University of Stavanger

Faculty of Science and Technology

MASTER'S THESIS

Study program/ Specialization: Offshore Technology / Marine & Subsea Technology	Spring semester, June, 2016 Open / ~~Restricted access~~
Writer: Ishie Jeremiah Ugochukwu	…… (Writer's signature)
Faculty supervisor: Professor Muk Chen Ong External supervisor(s): Dr. Kai Wang	
Thesis title: Structural Dynamic Analysis of Semi-submersible Floating Vertical Axis Wind Turbines	
Credits (ECTS): **30**	
Key words: Wind turbine, Simo-Riflex-DMS, Fatigue analysis, Coupled dynamic analysis, Finite Element Method, Time domain simulation, Aerodynamics, Hydrodynamics, Structural dynamics.	Pages: 132 + enclosure: 0 Stavanger, June 15 / 2016 Date/year

This page is intentionally left blank

Abstract

The risk, price inconsistency and environmental impact associated with oil and gas exploration and production have geared a focus on renewable energy. Wind power, the fastest growing source of renewable power generation in Europe, is a major competitor to oil and gas. The strong and stable wind at offshore locations and the increasing demand for energy have surged the application of wind turbines in deep water. Wind turbines are categorized into Horizontal Axis Wind Turbines (HAWTs) and Vertical Axis Wind Turbines (VAWTs) based on their respective orientation of axis of rotation. A floating wind turbine will experience large loads from wind, waves and rotating blades. Research has focused on the design, structural integrity, platform motion and installation of floating horizontal-axis wind turbines (FHAWTs) to better understand the performance of different concepts and to provide the basis for detailed structural design. However, the application of floating vertical axis wind turbines (FVAWTs) in deep offshore has potentials due to its economic advantage in installation and maintenance.

Research in the development of FVAWTs is still green. However, a variety of studies applied different simulation tools to investigate the response characteristics of FVAWTs to provide the conceptual design decriptions and detailed evaluation of technical feasibilities of the various concepts. This thesis adopted a 5MW Baseline FVAWT from Wang's PhD work. The FVAWT is a novel concept combining the 5MW DeepWind rotor and the DeepCwind semi-submersible from the Offshore code comparison collaboration Continuation (OC4) project. The response characteristics of the FVAWT was evaluated using a coupled non-linear aero-hydro-servo-elastic model (the Simo-Riflex-DMS code) which was developed by Wang for modeling FVAWTs. This coupled model incoorporates the models for the turbulent wind field, aerodynamics, hydrodynamics, structural dynamics and controller dynamics, and the simulation is performed in a fully coupled manner in time domain.

The FVAWT has been studied in a systematic manner, which includes a comprehensive investigation of the aerodynamics of the wind turbine to analyze the dynamic response of global motion for the floating system; considering normal operating condition to emergency shutdown event; as well as comparing the FVAWT with a FHAWT. However, the fatigue analysis for structural components such as blades, tower and mooring lines have not been performed. For FVAWTs, the continuously varying aerodynamic loads on the rotor lead to considerably higher

load level of the fatigue loads and number of load cycles. Therefore, it is significant to evaluate fatigue damage based on the time history of calculated response. The rainflow counting technique is used for short-term fatigue cycle counting. The Mlife tool from NREL is used to calculate the short-term fatigue damage equivalent loads for the FVAWT. Furthermore, this work is extended to model and evaluate the performance of a 5MW Optimised FVAWT in terms of power production, structural dynamic response, global motion and short-term fatigue damage on structural components. The 5MW Optimised FVAWT is a concept combining the optimised 5MW DeepWind rotor from the Technical University of Denmark (DTU) and the DeepCwind semi-submersible from the OC4 project. The two FVAWT concepts were evaluated under the same environmental condition.

The response characteristics of both 5 MW FVAWTs were studied under steady wind and turbulent wind conditions based on the statistical analysis and the spectral analysis of their responses to explore the effects of turbulence. The results identified that the effect of turbulence on the both FVAWTs resulted in an increased power generation, higher power variation, higher excitation for low frequency motions, greater fatigue damage but a reduction in the 2P effects. However, the effect of turbulence is negligible on the bending moment at the blade extremes but leads to higher loads on mooring lines and tower base especially at wind speeds above the rated wind speed. Furthermore, the results of the fatigue analysis showed that at wind speeds farther from the rated wind speed (14 m/s), the internal loads could have lower damaging effects than at wind speeds closer to the rated wind speed. Moreover, the dynamic response of the 5 MW Baseline FVAWT is compared with the 5 MW Optimised FVAWT in terms of power production, bending moment of structural components, global motion and short-term fatigue equivalent loads under turbulent wind condition. The results identified the 5 MW Optimised FVAWT to have lower Fore-Aft (FA) but higher lower Side-Side (SS) bending moment of structural components, lower motions amplitude, lower short-term fatigue equivalent loads and reduced 2P effects.

Acknowledgements

My deepest gratitude goes to my supervisor Professor Muk Chen Ong for giving me the opportunity to work on the topic I really wanted at UiS and his guiding role for this work. Professor Ong encouraged me to overcome many challenges and steered me to become an independent researcher. He is always ensuring all phase deadlines are met as planned throughout this work.

I would like to express my sincere indebtedness to my co-supervisor Dr. Kai Wang for his instruction, inspiration, and enlightenment throughout the thesis period. His manuals and procedures for the Simo-Riflex-DMS code were precise. He is always keeping contacts with me and discuss the progress of results with me through emails and skype calls.

Numerous people have contributed to my work through discussions. Special thanks to Prof. Ove Tobia Gudmestad for his encouragement and instructions on mooring line dynamics. I would like to thank Zhengshun Cheng from NTNU, my discussion with him triggered my quick understanding on how to set up the Simo-Riflex-DMS coupled simulation. I would like to thank Elizabeth Passano from Marintek for giving advice on the simulation set up when I was having challenges to run the code. I am also grateful to my friends and colleagues: Dr. Jasper Agbakwuru, Ifedinma Okeoma Njoku, Bjarte Odin Kvamme, Dr. Cornelius Agu, Utari Cendhy Liestyarini, Emeke Opute, Malakonda Reddy Lekkala, Muhammad Ahmad Tauqeer, Mika Pogosov, Lanjing Li, only to mention a few. They have been very helpful.

I also wish to acknowledge the opportunity given to me to study at the Department of Mechanical and Structural Engineering and Materials Science (IKM) of University of Stavanger (UiS), Stavanger, Norway. it was a dream come through.

Finally, I want to give special gratitude to my parent and my sister, Mrs Lilian Igba in Nigeria for their love have kept me going over the years. I could only achieve little without them.

Abbreviations

AC	Actuator Cylinder flow
BEM	Blade Element Momentum
BL	Beddoes-Leishman
CAPEX	Capital Expenditure
CFD	Computational Fluid Dynamics
CG/COG	Centre of Gravity
COB	Centre of Buoyancy
CP	Power Coefficient
DLC	Design Load Case
DLL	Dynamic Link Library
DMS	Double Multiple-Streamtube model
DNV	Det Norske Veritas
DS	Dynamic Stall
DTU	Technical University of Denmark
EU	European Union
EWEA	European Wind Energy Association
FA BM	Fore-Aft Bending Moment
FEM	Finite Element Method
FHAWT	Floating Horizontal Axis Wind Turbine
FVAWT	Floating Vertical Axis Wind Turbine
GDW	Generalized Dynamic Wake
HAWT	Horizontal Axis Wind Turbine
IEA	International Energy Agency
IEC	International Electrotechnical Commission
IFFT	Inverse Fast Fourier Transform
JONSWAP	Joint North Sea Wave Project

KW	Kilowatt
MIT	Massachusetts Institute of Technology
MSL	Mean Sea Level
MW	Megawatt
NACA	National Advisory Committee for Aeronautics
NREL	National Renewable Energy Laboratory
NTM	Normal Turbulence Model
NWP	Normal wind profile model
OC4	Offshore code comparison collaboration Continuation
PIV	Particle Image Velocimetry
PM	Pierson-Moskowitz spectrum
PSD	Power spectra Density
RANS	Reynolds-Averaged Navier-Stokes
SS BM	Side-Side Bending Moment
TLP	Tension Leg Platform
VAWT	Vertical Axis Wind Turbine
VTM	Vorticity Transport Model

Contents

Abstract ii
Acknowledgements iv
Abbreviations v
Content 1
List of Figures x
List of Tables xiv
1 Introduction 1
1.1. General Background 1
1.2. Wind Turbines 2
1.2.1. Wind turbine history 2
1.2.2. Vertical Axis Wind Turbines (VAWT) 5
1.2.3. Floating Vertical Axis Wind Turbines 9
1.3. State-of-Art in Modeling of FVAWT 12
1.4. Objectives and Thesis Scope 15
1.5. Thesis Outline 16
2 Theory 18
2.1. General 18
2.2. Wind 18
2.2.1. The power law 19
2.2.2. Turbulence 19
2.2.3. Turbsim 20
2.2.4. Wind power of an ideal rotor 21
2.2.5. Aerodynamic loads 24
2.2.6. Aerodynamic models 25
2.2.7. Dynamic stall 34
2.3. Waves 36
2.3.1. Regular waves 37
2.3.2. Irregular waves 40
3 The 5 MW Baseline Floating Vertical Axis Wind Turbine 44
3.1. The rotor 44
3.1.1. The platform 46
3.1.2. Generator 49

3.1.3. Mooring system 50
3.1.4. Safety and Emergency system 50
3.1.5. Control methodology 51
3.1.6. Potentials of the FVAWT concept 52
3.1.7. FVAWT concept challenges 52
4 The Optimised 5 MW Floating Vertical Axis Wind Turbine 54
4.1.1. The optimised DeepWind 5 MW rotor design 54
4.1.2. Methodology for Platform modification 61
5 Modelling of Floating Vertical Axis Wind Turbines 68
5.1. Dynamic Modelling of FVAWTs 68
5.1.1. Equation of motion 68
5.1.2. Non-linear FEM 69
5.1.3. Coupled Analysis 70
5.1.4. Coupled Modelling Tool for the Floating Vertical Axis Wind Turbine 71
5.1.5. Stochastic Modelling of the Environmental condition 72
5.2. Response to stochastic loads 73
5.3. Fatigue Analysis 74
5.3.1. The S-N Curves Approach 75
5.3.2. Cycle counting algorithms 76
5.4. Post-Processing Tools 76
6 Dynamic Response Analysis of Floating Vertical Axis Wind Turbine 78
6.1. General 78
6.2. Dynamic Response Analysis of the 5 MW baseline FVAWT 78
6.2.1. Validation of Response Results 78
6.2.2. Effect of Turbulence on FVAWT Performance 79
6.2.3. Effect of Turbulence on Structural Dynamic Response of the FVAWT 81
6.3. Dynamic response analysis of the 5 MW Optimized FVAWT 88
6.3.1. Model Validation 88
6.3.2. Effect of Turbulence on FVAWT Dynamic Response 90
6.3.3. Effect of Turbulence on Structural Dynamic Response of the FVAWT 99
6.4. Comparing the Dynamic response of the 5 MW Baseline and 5 MW Optimized FVAWT 106
6.4.1. Comparing Power Generation 106
6.4.2. Comparing Structural Dynamic Response 107
6.4.3. Comparing Global motion 113

6.5. Fatigue Analysis of Flexible Element 114
6.5.1. Fatigue Analysis of Flexible Element for the 5 MW Baseline FVAWT 115
6.5.2. Fatigue Analysis of Flexible Element for the 5 MW Optimized FVAWT 117
6.5.3. Comparing Fatigue Damage 119
7 Conclusion and recommendations for future work 122
7.1. Conclusions 122
7.2. Recommendations for Future Work 125
7.2.1. General comments 125
7.2.2. Specific recommendations 125
References 126
Appendix A 133
A.1- TurbSim Input file for the 5 MW Baseline FVAWT 133
A.2 - TurbSim Input file for the 5 MW Optimised FVAWT 136

List of Figures

Figure 1.1: 2015 share of new renewable power installations (MW). Total = 22,267.9 MW [1] ... 1

Figure 1.2: James Blyth's electricity – generation wind turbine, photographed in 1891 [7] 3

Figure 1.3: Fixed offshore wind turbine substructure concept [11] 4

Figure 1.4: Comparing fixed and floating wind turbine cost (Fixed in blue, floating in red) [12] .. 4

Figure 1.5: Floating offshore wind turbine substructure concept [38] 9

Figure 1.6: Axis of rotation of horizontal & vertical axis wind turbine [45] 10

Figure 1.7: Artist's impression of a floating VAWT farm[49] 11

Figure 1.8: Different FVAWT concept 12

Figure 2.1: Artistic side view of a semi-submersible VAWT showing the flow field grid size and hub height 20

Figure 2.2: Actuator disk model of a wind turbine; U, is air velocity; 1, 2, 3 and 4 indicate locations [83]. 22

Figure 2.3: Single Stream Tube visualization 26

Figure 2.4: Double Multiple Stream Tube visualization with U1 as the undisturbed wind speed. 27

Figure 2.5: Comparison of tangential forces of a VAWT, between MST and a Vortex code [99]. 28

Figure 2.6: The Actuator Cylinder flow model 29

Figure 2.7: Development of blade into a cascade configuration[116] 32

Figure 2.8: Mesh near the rotor. [83] 33

Figure 2.9: Ranges of validity for various wave theories. [133]. 39

Figure 3.1: The FVAWT concept 45

Figure 3.2: DeepCwind floating wind system design 47

Figure 3.3: Side view of platform walls and caps (abbreviations can be found in **Table 4.2**) 48

Figure 3.4: FVAWT model with hydrodynamic brake system.....51

Figure 4.1: The concept for the baseline VAWT rotor.....54

Figure 4.2: Schematic of standstill simulation with the rotor is subjected to self-weight.....56

Figure 4.3: Results from ANSYS analysis of various airfoil.....56

Figure 4.4: Results from analysis of sectioned blade.....57

Figure 4.5: Results from analysis of case-2 blade section.....58

Figure 4.6: Results from case-2 iterations.....58

Figure 4.7: Detailed description of the optimized rotor.....59

Figure 4.8: DeepWind modified troposkien rotor blade shape [143].....60

Figure 4.9: Load interpretation as used in SIMO.....62

Figure 5.1: Computation flow chart for the coupled model[71].....71

Figure 5.2: Bi-linear S-N-curve with an illustration of cyclic stress [154].....75

Figure 5.3: Post-processing flow chart.....77

Figure 6.1: Power generated under steady and turbulent wind conditions.....79

Figure 6.2: Transmitted torque under steady and turbulent wind conditions.....80

Figure 6.3: Blade FA and SS bending moment distribution.....81

Figure 6.4: Tower Base FA and SS bending moments.....83

Figure 6.5: Tower Base FA and SS bending moment's time series and PSD for DLC6.....83

Figure 6.6: Blade root (top) FA and SS bending moments.....85

Figure 6.7: Blade root (bottom) FA and SS bending moments.....85

Figure 6.8: Blade center FA and SS bending moments.....86

Figure 6.9: Mooring lines tension.....87

Figure 6.10: Mooring lines tension 2 time series and PSD for DLC6.....88

Figure 6.11: Comparing both FVAWT power generations.....89

Figure 6.12: Power generated under steady and turbulent wind conditions. 90

Figure 6.13: Time series and power spectrum of surge motion for DLC 3. 92

Figure 6.14: Time series and power spectrum of surge motion for DLC 6. 92

Figure 6.15: Surge motion for all DLC 92

Figure 6.16: Time series and power spectrum of sway motion for DLC 3. 93

Figure 6.17: Time series and power spectrum of sway motion for DLC 6. 93

Figure 6.18: Sway motion for all DLC 93

Figure 6.19: Time series and power spectrum of heave motion for DLC 3. 94

Figure 6.20: Time series and power spectrum of heave motion for DLC 6. 94

Figure 6.21: Heave motion for all DLC 94

Figure 6.22: Time series and power spectrum of roll motion for DLC 3. 95

Figure 6.23: Time series and power spectrum of roll motion for DLC 6. 95

Figure 6.24: Roll motion for all DLC 95

Figure 6.25: Time series and power spectrum of pitch motion for DLC 3. 96

Figure 6.26: Time series and power spectrum of pitch motion for DLC 6. 96

Figure 6.27: Pitch motion for all DLC 96

Figure 6.28: Time series and power spectrum of yaw motion for DLC 3. 98

Figure 6.29: Time series and power spectrum of yaw motion for DLC 6. 98

Figure 6.30: Yaw motion for all DLC 98

Figure 6.31: Blade FA and SS bending moment distribution for all DLC 100

Figure 6.32: Blade mean FA and SS bending moment distribution at all DLC 100

Figure 6.33: Tower base FA and SS bending moments 101

Figure 6.34: Tower Base FA and SS bending moment's time series and PSD for DLC6. 102

Figure 6.35: Blade root (top) FA and SS bending moments 103

Figure 6.36: Blade root (bottom) FA and SS bending moments 104

Figure 6.37: Blade center FA and SS bending moments 104

Figure 6.38: Mooring lines tension. 105

Figure 6.39: Mooring lines tension 2 time series and PSD for DLC6. 106

Figure 6.40: Comparing Power generation 107

Figure 6.41: Comparing distribution of bending moment along the blade 108

Figure 6.42: Tower base FA and SS bending moments 109

Figure 6.43: Tower Base FA and SS bending moment's time series and PSD for DLC6. 110

Figure 6.44: Blade root (bottom) FA and SS bending moments 111

Figure 6.45: Mooring lines tension. 112

Figure 6.46: Mooring lines tension 2 time series and PSD for DLC6. 113

Figure 6.47: Comparing time series and power spectrum of roll motion 113

Figure 6.48: Comparing time series and power spectrum of pitch motion 114

Figure 6.49: Fatigue STDEL of selected areas 117

Figure 6.50: Fatigue STDEL of selected areas 119

Figure 6.51: Fatigue STDEL of selected areas 120

List of Tables

Table 1.1: VAWTs and HAWTs comparison 7

Table 3.1: Technical and geometric properties of the 5 MW DeepWind turbine baseline design 46

Table 3.2: Platform abbreviatios in **Figure 3.3** 48

Table 3.3: Geometry, Structural and hydrodynamic properties of platform configuration 49

Table 3.4: Mooring System Properties 50

Table 4.1: Aerofoils properties with chord length of 5m and rotor height shown in **Figure 4.2**. 56

Table 4.2: Description of rotor sections 57

Table 4.3: The optimised blade properties (Case -2) 58

Table 4.4: The properties of the 5 MW optimised DeepWind rotor 60

Table 4.5: Tower cross-sectional properties 61

Table 4.6: Platform properties 65

Table 5.1: Combined wind and wave environment for normal operating condition 73

Table 6.1: Description of nodal points selected for blade bending moment evaluation 81

Table 6.2: Description of nodal points selected for blade bending moment evaluation 99

Table 6.3: Description of selected positions for fatigue analysis 115

Table 6.4: Description of legends as used in the plots 116

Table 6.5: Description of selected positions for fatigue analysis 118

Table 6.6: Description of legends as used in the plots 120

This page is intentionally left blank

1 Introduction

1.1. General Background

The interest on renewable energy has increased tremendously within the past decade. The risk and environmental impact associated with oil and gas exploration and production has triggered focus on the development of renewable energy resources. Furthermore, the political instability in oil producing countries and the oil price inconsistency have encouraged governments and organizations to explore alternative energy sources that would reduce the exposure of their countries' economies to oil price instability.

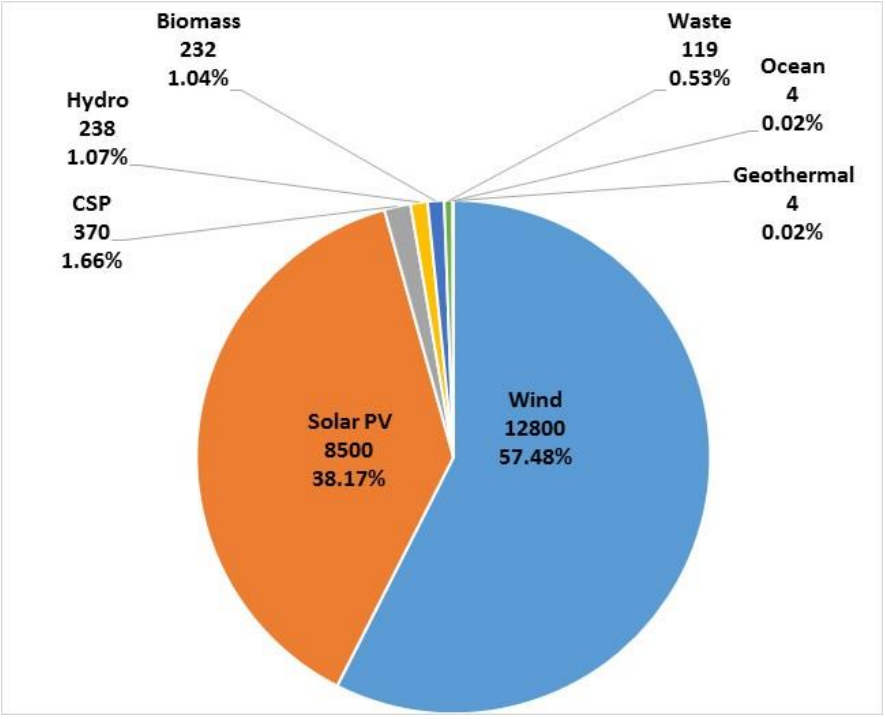

Figure 1.1: 2015 share of new renewable power installations (MW). Total = 22,267.9 MW [1]

Wind power is the fastest growing source of renewable power generation in Europe. According to the latest EWEA report, the year 2015 made it the eighth year in a row where renewable energy contributed over 55% of all additional power capacity and a landmark of 77% share of all new EU power installations in 2015 [1] . In 2015, Wind power contributed over 57% of total renewable energy (see **Figure 1.1**) and offshore wind power has been predicted to contribute 40 % share of the projected 300,000 MW wind capacity for the year 2030 in Europe [2] . Currently, wind power with a 15.6% share of the total EU power capacity represents the third largest source of power generation.

Wind energy has great potential for the future. However, wind power generation is limited by the high capital investment required for its commercialization. Wind turbine projects cost a fortune and thus, various methodologies has been applied to cost reduction. The cost of wind turbine projects are estimated using cost models such as the Operation and Maintenance (O &M) tool from the Energy Research Centre of The Netherlands [3, 4]. Although, various models exist for cost estimation, the risk reduction from wind energy is presently not accounted for by standard methods for calculating the cost of energy [2].

Therefore, wind power is more expensive per KW as compared with other means of power generation for example gas turbine. However, it proved to be the most sustainable energy source among other renewable energy sources such as current, wave, tidal, solar, etc. Wind power could have a competing share with the power generation from petroleum in the nearest future. Therefore, there has been many research in this area to further develop the wind power system in order to efficiently harness the available offshore wind resources.

1.2. Wind Turbines

1.2.1. Wind turbine history

Wind turbines are machines used to convert the kinetic wind energy into electrical power. The first generation of wind turbines, commonly called windmills were used to power machines directly such as grinders in Persia (present day Iran) [5], the Hero of Alexandria's windwheel [6] until 1887 when the first electricity generating wind turbine was built by James Blyth [7] (see **Figure 1.2**) .

The system components of wind turbines have changed since the 18th century. A simple wind turbine consist of the blade system - called the rotor, a shaft/tower, a generator, a foundation and electrical cables. The rotor is connected to the shaft at one end, the generator is connected to the other end of the shaft.

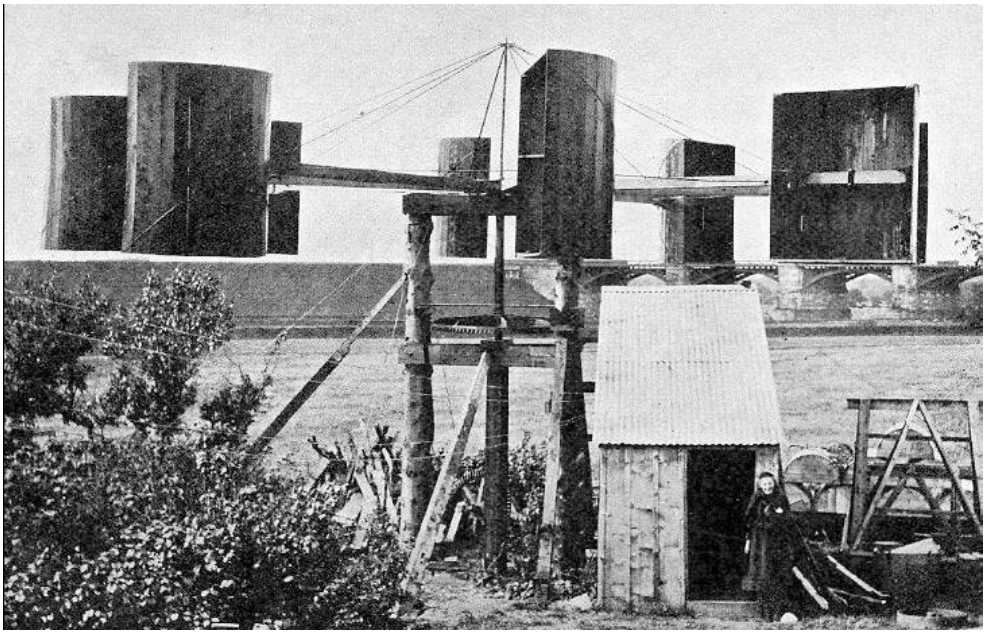

Figure 1.2: James Blyth's electricity – generation wind turbine, photographed in 1891 [7]

The rotor-shaft-generator system is supported by the foundation. The wind kinetics drives the rotor which subsequently transmit motion to the shaft through a system of gears. The rotational kinetic energy of the shaft is converted to electric power as the shaft turns the rotor of the generator within the generator's electromagnetic field. The electrical cables are used to transmit the produced electricity to the end user.

Wind turbines can be fixed on land and near shore or set to float offshore in deep waters. Offshore wind turbines have vast potentials due to the stable wind available offshore and offers advantages over land windfarm in terms of noise reduction and visual esthetics [8]. In shallow water, fixed substructures (**Figure 1.3**) are more attractive for offshore wind farm development due to their technological success in this region. The need to exploit wind resources far offshore in deep waters requires the use of floating support structures to be economically viable. Furthermore, as deeper water is approached, the use of floating substructure for wind turbine system becomes more economical due to their flexibility in changing the location of the system for major maintenance and ability to be deployed further offshore where there is generally more

consistent, or stable wind, including flexible installation process [9]. The cost of floating structures (see **Figure 1.4)** for deep waters application could as well compete with the fixed bottom substructures with insignificant cost increment per MW on a commercial scale [10]. Moreover, offshore maintenance cost and the risk associated with marine operations have limited the advantages of offshore windfarms over the land based windfarm.

Figure 1.3: Fixed offshore wind turbine substructure concept [11]

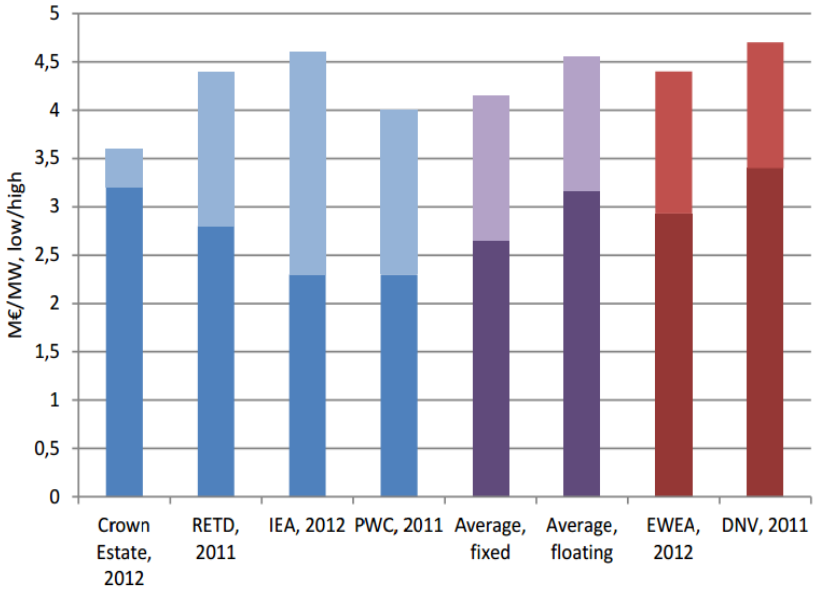

Figure 1.4: Comparing fixed and floating wind turbine cost (Fixed in blue, floating in red) [12]

Floating wind turbines respond differently to the varying environmental loads depending on the concept of the floating substructure. In the same vein, the Capital Expenditure (CAPEX) and the fatigue life of the wind turbine is significantly influenced by the type of support substructure. In the last decades, research to improve offshore wind turbine focused on the efficiency of electricity production, reduction in CAPEX, increased fatigue life etc. [13].

1.2.2. Vertical Axis Wind Turbines (VAWT)

Wind turbines are classified based on the dynamic motion of turbine support substructures (Fixed versus Floating wind turbine), the geographic position (Land wind based versus Offshore wind turbine) and the orientation of the axis of rotation of the rotor (Horizontal versus Vertical axis wind turbines). Furthermore, these various classifications can be combined. For example, a Vertical Axis Wind Turbine (classified based on the orientation of the axis of rotation of the rotor) with a floating substructure (based on the dynamic motion of turbine support substructure) is referred to as a Floating Vertical Axis Wind Turbines (FVAWT).

The rotor can be a Vertical Axis Wind Turbines (VAWT) or Horizontal Axis Wind Turbines (HAWT) as explained above. In this thesis, the focus will be on the Darrieus concept which was patented in 1926 [14]. In the 70s, VAWT was likely the best alternative for wind power exploitation in an attempt to address the resident energy crisis. However, VAWTs was not used any further in the development of the commercial wind turbines. This was the case between the 70s and the 90s.

The VAWT are categorized according to the rotor shape:

- Straight blades.
- Curved blades

The straight bladed VAWTs have all the blade elements at equidistance to the axis of rotation. Furthermore, at some fixed time, and neglecting the variation of wind velocity with the height, all the elements of one blade experience the same tip speed ratio. Therefore, it becomes possible in principle for the rotor to run at an optimum tip speed ratio for all the blade airfoils. This is not possible with curved blades, because the tip speed ratio changes along the blade. However, optimized tip speed ratio for straight bladed VAWTs will maximize their efficiency, measured in terms of power coefficient. The maximised efficiency of the straight bladed VAWT is higher than that of the curved blade. Moreover, the blades of straight bladed VAWTs require supporting connection arms, which would create a negative drag and reduce the power coefficient. In theory, all the blade elements would stall at the same time. Therefore, the peak for the straight bladed VAWTs are higher but less broad, compared with curved blades. The straight bladed VAWT has been used in combination with cambered airfoils and pitch passive control to increase the torque at the start in order to have self-starting ability [15].

The curved VAWT is known by its varying tip speed ratio along the blades, thus, each blade element stalls at different wind speeds at constant VAWT rotational speed. The application of the Troposkien shape in curved VAWT, remain one of its most significant advantage [16]. A Troposkien blade is a blade with shape of a perfectly flexible cable of uniform density and cross section, spinning around a vertical axis at constant rotational speed. One advantage of the Troposkien blade is the transfer of centrifugal loads induced stresses to tensional stresses in the blade direction and thus eliminate flatwise moment acting on the blade. This is a significant characteristic used in increasing the fatigue life of the VAWT since the aerodynamic loads acting on the blade are periodical.

In the 70s, smaller diameter VAWTs having diameters less than 35m was used with curved blades and many research institute dedicated resources to research in this area. The Sandia Laboratory in Albuquerque (New Mexico in United States), has been one of the most active research institute on VAWT.

Thus, data are available for the three Sandia VAWT:

- The 2m diameter [17], that was primarily built for a wind tunnel test [18] in the 70s.
- A 5m [19] was built as a proof-of-concept machine in 1974.
- A 34m 500 kW [20] was erected and used as a test bed case [21].

For the Sandia 2m diameter, NACA 0012 airfoils was used for the Troposkien shaped blade. The results of the experiments showed a significant influence of the Reynolds number on the power production and an optimum solidity at fixed Reynold number was between 0.2-0.25.

For the 5m diameter with a solidity of 0.22, a maximum power coefficient of 0.39 was reached. The value of the drag coefficient of the turbine was also estimated by spinning the turbine at no wind condition. The results showed that as the Reynolds number increases, the drag coefficient decreases.

The 34m 500kW turbine operated from 1987 to 1998. It was a milestone in VAWT development and it was the facility for several studies including an investigation on resonance response [22], new geometric configurations testing, application of tapered blades with 3 different chords and first laminar airfoils for wind turbines [23], application of a direct-drive and a variable speed generator to control the wind turbine [24]. Furthermore, a comparative investigation on two possible geometries was carried out by Sandia and FloWind Corp. on the 300kW wind turbine

[25]. The effects of increasing the rotor ratio (height to diameter ratio), from 1.31 to 2.78 was evaluated. It was summarised that it lead to a simultaneous increase of the swept area and the cost. However, FloWind succeeded in using pultruded blades, even though the pultrusion technology was unproven.

Table 1.1: VAWTs and HAWTs comparison

Parameter	VAWT	HAWT	Comments
Geometric simplicity	Simpler	More complex	VAWT blades are neither tapered nor is twisting present.
Yaw control system	No	Yes	VAWT is independent of wind direction, this implies huge cost savings.
Centre of gravity (CG)	Lower CG	Higher	Electrical or mechanical components could be placed at the bottom of the structure
Blade length	Longer	Shorter	A VAWT of the same swept area as the HAWT requires blades which are 2-3 times longer than a HAWT.
Self-starting	No	Yes	VAWTs are not self-starting and requires torque from a motor at start-up. Although, this problem has been solved using pitching straight blades and cambered airfoils for new concepts. [14]

The largest VAWT, EOLE, which was developed at the Hydro-Quebec and the National Research Centre of Canada started operations in 1988. The rotor was constructed by Versatile Vickers shipyard. The turbine had a height of 96m and a maximum diameter of 64m with a chord length of 2.4m. The NACA0018 airfoils were used. EOLE was a variable-speed – direct drive wind turbine and its 12m wide generator was rated 4MW at 14.5 Revolution Per Minute (RPM). It powered up to 2.7MW and at 11.35 RPM. Although EOLE had high availability (94%), it was shut down in 1993 after five years of operation due bottom bearing failure [26].

These series of VAWT development provided a possibility to evaluate potentials and problems associated with commercial development of VAWT. These are well documented by Paraschiviu [27]. **Table 1.1** compares VAWTs to HAWTs in terms of technological economies.

In spite of the advantages in **Table 1.1**, a major disadvantage of VAWTs are the periodic aerodynamic loads which includes fatigue damage on the tower and the bearings. Thus, the stiffness of the tower at the upper bearing is usually increased by pre-tensioned guy-wires [20]. However, these guy-wires creates additional problems: their natural frequency is within the range of the operational rotational speeds, thus a damper is required to avoid resonance; the tension in the guy-wires create a vertical load component on the rotor which must then be absorbed by the bottom bearing. Hence, alternative solutions such as a structural bearing could be applied to avoid this problem. This would be additional structural costs.

The above points ensures HAWTs supremacy in the 90s and also their commercialization for MW size wind turbines. The VAWTs have been applied to a only few areas within the last 20 year, where their technological advantages are of primary importance in urban wind energy [28] and hydropower turbines [15].

Economical and global energy change may drive new ambitions to the wind energy industry which could revitalize VAWT to compete side by side with HAWT in commercial wind turbine applications. The new targets for wind energy production has pushed beyond the limit of the rotor size, thus looking for new technologies and solutions. In the second edition of “The World Offshore Renewable Energy Report” [29], published by the British Department of Trade and Industry, VAWT has been said to be a possible solution for large wind turbines. The VAWT could be therefore represent the next generation rotor for offshore wind turbine.

Apart from the problem of the choice of rotor, offshore wind industry is faced with other logistic issues. One of the most challenging problems is the installation of wind turbines in deep waters. It is general that floating substructure are more economical and convenient than the monopiles for offshore sites deeper than 50m [30-32].

The first idea of a floating wind turbine was a SPAR concept proposed by Bill Heronemus from MIT in the early 70s [33]. The end of the energy crisis in the 70s ended several pioneering ideas in the field of wind energy, such as the ones of Heronemus and Ljungström. But nowadays, following the instability in the supply of fossil sources of energy, some of those ideas are now welcomed.

1.2.3. Floating Vertical Axis Wind Turbines

The dynamic response of a floating wind turbine differs significantly from that of a bottom supported substructure or a land base wind turbine. Therefore, it is pertinent to analyze numerous substructure in order to understand their respective dynamics and suitability for a particular sea state.

Hence, various concepts were developed and investigated for use as floating substructures to support the wind turbines. These concepts includes the spar[34] , the semi-submersible [35, 36] and the TLP concepts [37] are shown in **Figure 1.5**.

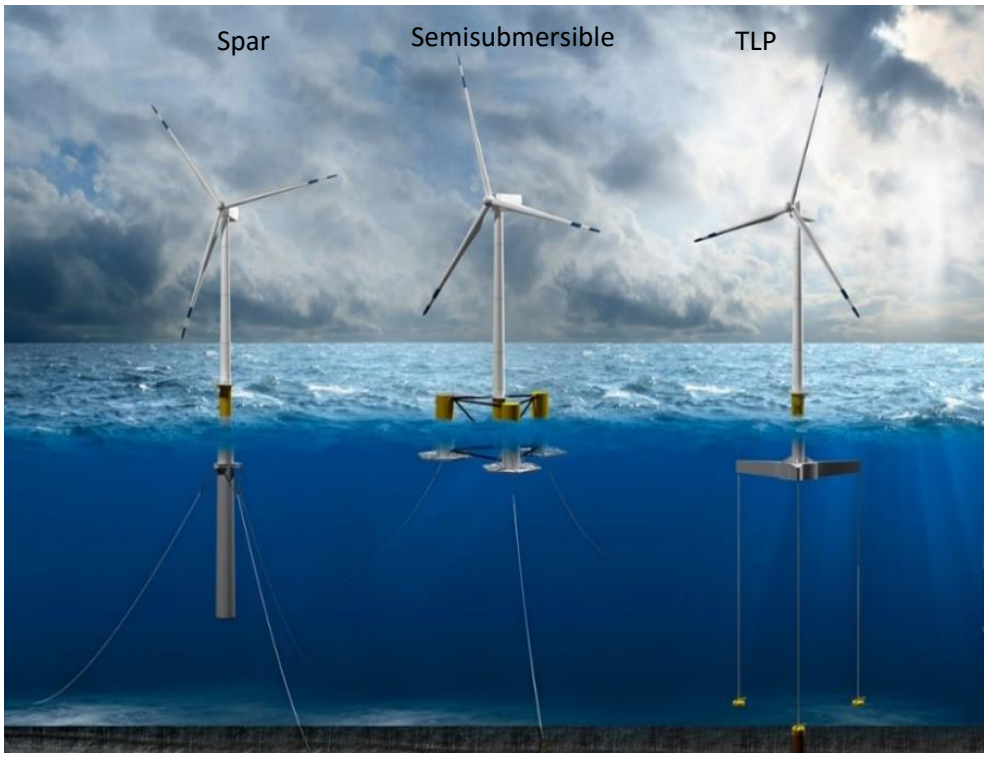

Figure 1.5: Floating offshore wind turbine substructure concept [38]

The Floating Horizontal Axis Wind Turbines (FHAWT) has been the research focus on deep wind power production due to their commercial success in onshore applications. Studies have focused on the design, structural integrity, dynamic response and installation methodologies of FHAWTs to better understand the performance of the various concepts and to provide the basis for detailed structural designs [35, 36, 39-42] . However, the conventional floating horizontal axis wind turbine may not continue to be the optimal design for floating wind turbine applications. Therefore, it is imparative to assess alternative concepts that may be more suitable.

Furthermore, it is important to understand the technical characteristics of Floating Vertical Axis Wind Turbines (FVAWTs) (see **Figure 1.7**) in order to harness their complete potentials.

FVAWT and FHAWT differs in their rotor axis of rotation; the blades of FVAWT rotates about the vertical while that of FHAWT rotates about the horizontal as shown in **Figure 1.6**. Also, it is possible to design either VAWT or HAWT rotor on similar concept of support substructure. For example, a VAWT or HAWT rotor can be supported by a semi-submersible substructure. Moreover, the FHAWT can confidently run on idle mode while FVAWT is considered not suitable for such condition [43]. Furthermore, most VAWTs rotor such as the 2-bladed Darius rotor, are fixed-pitch blades. This accounts for the large aerodynamic loads experienced in stormy wind. The large aerodynamic loads could cause catastrophic failure of the blades or/and the tower especially in the absence of blade pitch mechanism. Therefore, it is important to design FVAWT for such extreme weather conditions.

The effect of the azimuthal position of the blades on the dynamic response was studied in parked condition where the wind turbine is halted and it was found that the aerodynamic loads on the rotor experiences a continuously variation with the azimuthal blade position which is magnified under turbulent wind condition. The 2P effects on structural loads and mooring line tensions are prominent for the FVAWT concepts. Although, the larger global motion of the spar and the semi-submersible substructure was predicted to reduce the 2P effects [44].

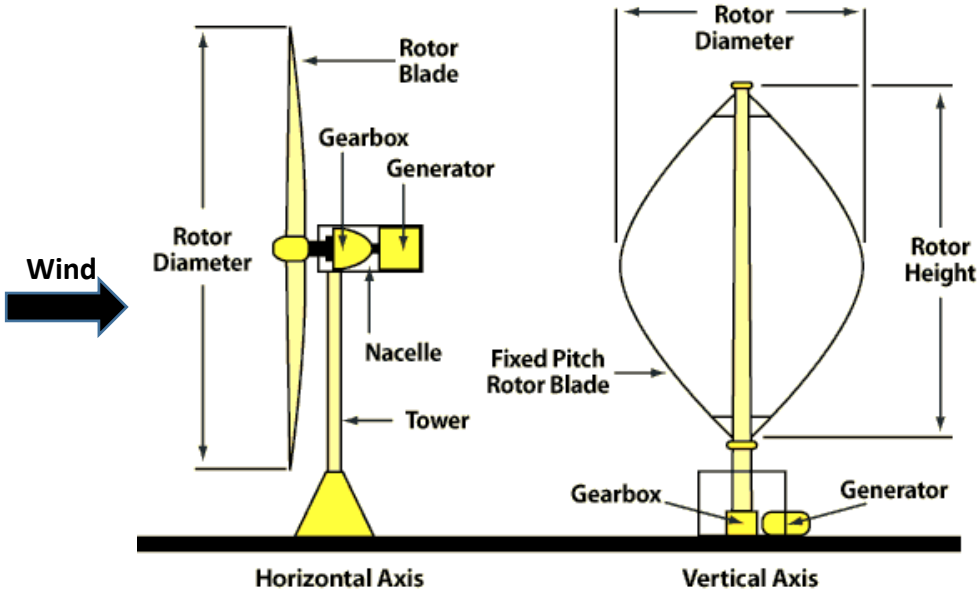

Figure 1.6: Axis of rotation of horizontal & vertical axis wind turbine [45]

The application of VAWT rotor technology in large wind turbines could reduce the cost-of-energy (COE) by over 20% [46]. Furthermore, due to higher maintainability of FVAWT, and its ability to capture wind energy regardless of wind direction without a yaw control mechanism, lower center of gravity, economies of installation amongst other as compared with Floating Horizontal Axis Wind Turbine [47] proved FVAWT could be a better concept in deep waters.These aforementioned advantages steered resurgence of interest in research on FVAWT in deep water [43, 48].

Figure 1.7: Artist's impression of a floating VAWT farm[49]

Floating Vertical Axis Wind Turbines have attracted interest in the offshore wind industry, and different concepts of Floating Vertical Axis Wind Turbines (FVAWT) have been evaluated, such as the DeepWind concept [50-52], the VertiWind concept [53] and the Aerogenerator X concept [52, 54] , for conceptual designs and technical feasibility (See **Figure 1.8**). Another novel concept combining the DeepWind 5 MW rotor[55] and the DeepCwind floater from the OC4 project,[56] was extensively investigated as well.

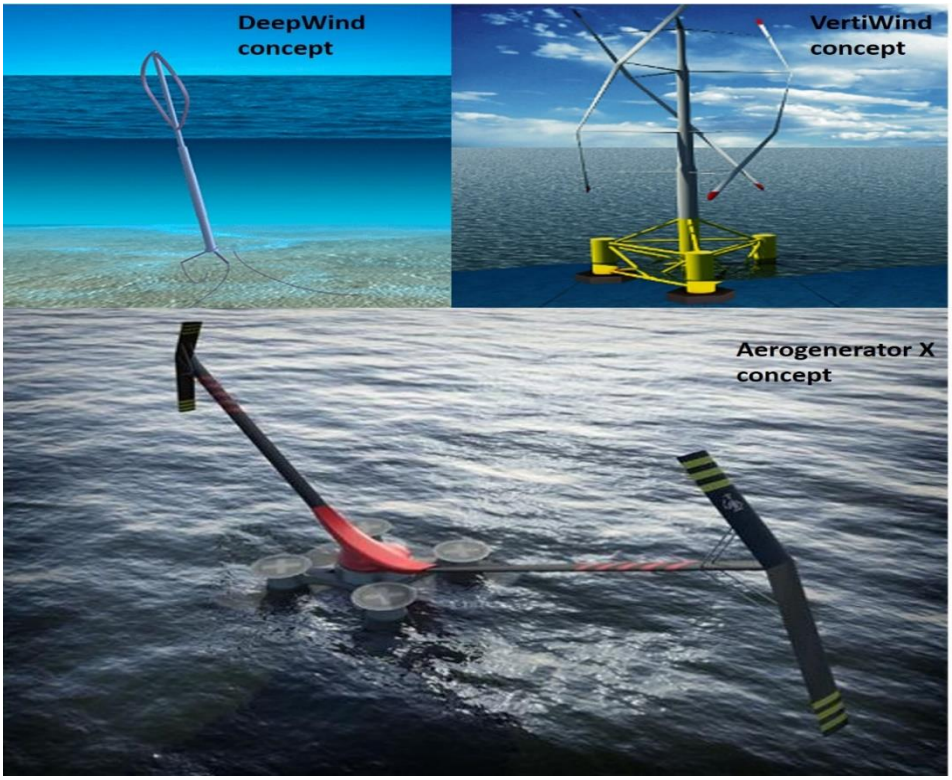

Figure 1.8: Different FVAWT concepts

1.3. State-of-Art in Modeling of FVAWT

Modeling of aerodynamic loads on FVAWTs rotors using numerical codes dated far back in the 1970s. There are two numerical methods: The vortex codes which is based on the Biot-Savart vorticity formula and The stream-tube codes based on the Blade Element Momentum (BEM) theory. The stream-tube codes, are based on the disk actuator concept which equates the total forces on the blade to the change in momentum of the air stream flow passing through the rotor. The results from the vortex codes are considered more accurate but requires high computational time with convergence issues at low rotational speed. Therefore, the stream-tube code is usually preferred in development of aero-elastic codes for simulating floating wind turbines because it has very fast computational time [57]. Strickland in 1975, improved the accuracy of the earliest stream-tube codes with the multiple streamtube model [58], by dividing the rotor into various streamtubes in order to investigate the variation of the flow in two perpendicular directions. Further, Paravischivoiu improved the model by adding an actuator disk in order to account for the induced velocities in both the upstream and downstream of the rotor blade[27]. In order to investigate the velocity field in three dimension in the stream flow instead of the two

perpendicular direction as proposed by Strickland, Madsen [59] replaced the plane actuator disk with an actuator cylinder.

One major difference between the modeling of floating wind turbine and landbase wind turbine is the present of hydordynamic loads in floating wind turbine. In modeling floating wind turbines, the dynamic coupling of between the motion of the wind turbine and that of the floating substructure must be considered. Therefore, three simulation codes are usually coupled to predict the dynamic response of the floating wind turbine in the time domain: An hydodynamic model to simulate the rigid body hydrodynamic loads on the support substructure, a finite element solver to model flexible elements for the mooring system and rotor system including serving as the link to an external controller, and an aerodynamic code to estimate the aerodynamic loads on the rotor system based on BEM or Generalized Dynamic Wake (GDW) theories. Thus, a stable combination of a non-linear finite element solver,a sophisticated hydrodynamic code, a well-tested aerodynamic code, and a control logic are usually coupled.

Several state-of-art coupled codes have been developed over the years, HAWC2 [60-62] was developed at Risø DTU. In HAWC2, an aero-elastic code - double disk multiple Streamtubes was linked to it using the Dynamic Link Library (DLL) in order upgrade its ability to simulating FVAWT in time domain for the DeepWind FVAWT. HAWC2 is a multi-body simulation tool which allow the separate modelling of individual component of the turbine. However, the hydrodynamic model employed is more accurate for slender substructure like spar (Morrison like structures), thus it is not suitable for analysing structures such as the semi-submersibles.

The coupled aero-hydro-servo-elastic code, SIMO-Riflex-Aerodyn was also developed [63] to fully integrate the complete features of Aerodyn [64] into SIMO-Riflex coupled module. However, this is used to model FHAWT and not suitable for FVAWT.

At Cranfield University in UK, Borg et al [65]developed a simplified coupled design code using MATLAB programming for preliminary design analysis of FVAWTs. This code is called FloVAWT. The code has been on continual development and verification by Collu et al [66]. Gormot-Berg dynamic stall model was applied in the aerodynamic model (Double Multiple Streamtubes). However, the code was criticized of lacking structural model, mooring line model and dynamic control model, hence, the rotor is assumed rigid with constant rotational speed and the relationship between force-displacement is then linearized.

A non-linear aero-hydro-servo-elastic, Simo-Riflex-DMS was developed for modeling FVAWTs with semi-submersible substructure. The Double Multiple Streamtube (DMS) code [67] is an aero-elastic code used to model the aerodynamic load on the wind turbine rotor. The Riflex code is the finite element solver while the SIMO code is used to model the floater hydrodynamics. Therefore, Simo-Riflex-DMS simulation code couples the wind velocity stream, aerodynamics, hydrodynamics, structural dynamics and controller module.

As discussed earlier, the dynamic response of FVAWTs significantly differs from onshore VAWT. FVAWT experiences larger pitch motion from environmental loading resulting tilting of the VAWT's tower. Therefore, the effect of tower tilting on the performance and aerodynamic loads must be evaluated. This similar effect has recently been discovered to be important in VAWTs operation on high buildings where skewed inflow is occasionally present. Furthermore, a single actuator disk multiple streamtube model has been used to investigate the performance of an H-Darriues designed high and the result of the analysis was compared with wind tunnel measurements conducted by Mertens et al. [68]. The results showed the skewed flow causes an effective increase of the energy extraction area and subsequently leads to an increased power output.

The DMS codes were not originally developed for FVAWT. Thus, the original DMS code did not account for secondary effects such as dynamic stall in FVAWT and tower tilting. For the above reason, the DMS model must be modified to account for the effect of tower tilting for the curved-blade Darriues VAWTs on floating substructures including a dynamic stall model. Wang et al. [69, 70] in 2013 , made an important modification to the DMS code to include the effect of tower tilting and the Gormont's model with the adaptation of the Strickland and the Gormont's model with the modification of Berg and the Beddoes-Leishman Dynamic Stall (BL DS) model were applied for the dynamic stall effect. The improved DMS model was further validated by a code-to-code comparisons with different dynamic stall models[69, 70] and experimental data from the small 17m Sandia wind turbine and the largescale 5 MW wind turbine used for the DeepWind project. Furthermore, the aerodynamic performance and aerodynamic loads at zero tower tilt angle simulated and compared with the experimental data. The results shows a better performance and a more accurate representation of the FVAWT aerodynamics. The modified DMS code is referred to as DMS in this work except otherwise stated.

In the Simo-Riflex-DMS has been used to analyze a novel model that combined the DeepWind 5 MW rotor [55] and the DeepCwind floater from the OC4 project, [56] in a fully coupled time – domain simulation [69]. The technical details of Simo-Riflex-DMS is given in the subsequent section.

This Simo-Riflex-DMS model as developed by Wang [71] is adopted for this thesis.

1.4. Objectives and Thesis Scope

The objective of this thesis is to perfrm dynamic analysis of a floating vertical axis wind turbine with two different rotor configuration. Comparison between these two wind turbines are carried out and discussed. In order to accomplish the objective, the following milestones enumerated have to be achieved:

- Understand the coupled model: Familiar with basic aerodynamic theory, hydrodynamics and structural dynamics and controller in the model.
- Create the coupled model in SIMO and Riflex.
- Set up the responses and run the coupled code: Global motion in SIMO; Tower base bending moment, blade bending moment and mooring line tension in Riflex.
- Postprocess the simulation results: statistical analysis and spectral analysis for structural dynamic responses.
- Estimate the fatique damage of flexible elements: Mlife [72] is used to calculate the short-term fatigue damage equivalent loads of the tower base Bending moment, Blade bending moment and mooring line tension for fatigue analysis.
- Compare the short-term fatigue damage equivalent loads of the FVAWT for steady wind conditions and turbulent wind conditions.
- Establish a coupled model of a new FVAWT model based on the optimized DeepWind Wind turbine from DTU publication [73].
- Compare the responses between the Baseline FVAWT and te Optimised FVAWT models.

A semi-submersible FVAWT concept [69] is adopted for this project. This concept has been studied in a systematic manner: A method for the analysis has been developed, global motion for the floating support structure was comprehensively analyzed - considering normal operating

condition and emergency shutdown event, a comparative analysis between the proposed model and a similar model with HAWT rotor has been carried out including a stochastic analysis of the model [43, 69, 74]. However, extensive investigation of the fatigue damage for flexible components such as the blades, the tower and the mooring lines have not been carried out. The continuously varying aerodynamic loads on the rotor lead to higher stress level and increased number of load cycles. Therefore, it is significant to evaluate fatigue damage based on the time history of calculated responses. The rainflow counting technique, as the most common method for fatigue damage estimation, is employed in this thesis. The detailed fatigue analysis is found in chapter 5.

The dynamic response of the proposed FVAWT is investigated by analyzing its global motion, by statistical analysis and spectral analysis of structural components, and by estimating short-term fatigue damage equivalent loads of the rotor system. Furthermore, the rotor for DTU proposed DeepWind concept was optimised by a group of researchers at DTU The tower to weigh 2/3 less than 1st baseline 5 MW design. This optimised model has lower bending moments and lower tension during operation [75]. A model based on the DTU optimised concept is built and the simulation results is compared with this project base model.

1.5. Thesis Outline

The outline of this thesis is developed to reflect the thesis objectives.

Chapter 1 entails the background, motivation and objectives of this work.

Chapter 2 presents the theory for estimating aerodynamic and hydrodynamic loads on vertical axis wind turbines.

Chapter 3 presents the details of the 5 MW DeepWind rotor from Risø DTU and the adapted semi-submersible substructure from OC4 project as used in
Wang's PhD thesis.

Chapter 4 presents the details of the 5 MW optimized DeepWind rotor from Risø DTU the adapted semi-submersible substructure from OC4 project as modelled in this thesis.

Chapter 5 gives overview of the modelling methodology as applied in this work. The coupled modeling technique based on the state-of-art simulation tool, Simo-Riflex-DMS to which incorporate an aerodynamic model, hydrodynamic model, structural model and control model is introduced. Furthermore, it describes vividly the approach adopted for the selection of environmental conditions and the post-processing tools used for the analysis of the simulation results.

Chapter 6 presents the structural dynamic response analysis of the FVAWTs based on the coupled nonlinear time domain simulation under turbulent and steady wind condition.

The analysis for the 5 MW Baseline FVAWT includes:

- Validation of response results.
- Analysis of response characteristics under steady and turbulent wind condition.
- Statistical and spectral analyses of the FVAWT responses.
- Structural analysis of flexible components of the FVAWT.

The analysis for the 5 MW Optimized FVAWT includes:

- Validation of response results.
- Analysis of response characteristics under steady and turbulent wind condition.
- Statistical and spectral analyses of the FVAWT responses.
- Analysis of global motion
- Structural analysis of flexible components of the FVAWT.

Furthermore, this chapter also includes a comparison between the dynamic responses of the 5MW baseline FVAWT and the 5MW optimized FVAWT models.

Chapter 7 is a summary of this work. It is mainly about the thesis conclusion and recommendations for future work.

2 Theory

2.1. General

To fully analyze the dynamic response of FVAWTs, the FVAWT parameters must be investigated under realistic environmental conditions which includes wind, waves and current. However, effect of current could only result in a slow platform drift and increased mooring line tension. Therefore, the environmental conditions considered in this thesis are combined waves and wind only.

2.2. Wind

The wind condition at a particular location is represented by the wind parameters, U_{10} and σ_U. The 10-minute mean wind speed U_{10} is a measure of the intensity of the wind at a reference height, H. The standard deviation σ_U is a measure of the variability of the wind speed about the mean. Wind conditions are either long term or short term. The long-term and short-term wind conditions are represented using wind speed statistics. Long-term wind condition is usually refered to as wind condition with exceedance probability of less than or equal to 0.1 while short-term conditions are 10 minutes mean (U_{10}) of the wind storm. The long-term distributions of U_{10} and standard deviation (σ_U) are based on statistical data for the same averaging period for the wind speed as the averaging period which is used for the determination of loads. It is also possible to determine the long term wind condition based on a reliable hindcast data [76]. Therefore, generic probability distributions like weibull or scatter diagiam are used to model the distribution of the long term wind parameters. The short term 10 minutes stationary wind climate is

represented by its power spectra density $S_{U(f)}$ of the wind speed process. $S_{U(f)}$ describes how the energy of the wind speed at a specific point in space is distributed between various frequencies.

Wind speed varies with time and height above the sea surface. The wind speed profile is a representation of the mean wind speed and its' variation with height above the sea surface. In the absence of complex stability and terrain conditions, idealized models are used for this representation. Three examples of such idealized models are detailed in DNV-RP-C205 [77]:

- The logarithmic wind profile model
- The power law wind profile model and
- The Frøya wind profile model.

Among these wind models, logarithmic and power law wind profile remain the most widely applied models. However, for unique conditions like land in the vicinity of ocean waters, the commonly used wind profile models may be insufficient to model such special cases, hence complex wind profiles which are developed by inversion are employed. The power law is applied in this thesis to model the wind profile, hence details of the logarithmic and the Frøya wind profile model will not be discussed further in this work.

2.2.1. The power law

The power law model of the wind profile shows the wind variation with the altitude. A power law model is represented as shown in equation 2.1.

$$U\left(z\right)=U_{(H)}\left(\frac{z}{H}\right)^{\alpha} \tag{2.1}$$

Where $U_{(H)}$ is the reference wind speed, H is the height at which the reference wind speed is specified and the power law exponent α depends on the terrain roughness.power law exponent. For this study, the value of H was set to 79.78 m (vertical centre of blades) above MSL and the value of was α set to 0.14 for the floating turbine according to IEC 61400-3 [78].

2.2.2. Turbulence

The wind turbulence is a function of the standard deviation σ_U and it descibes the conventional variation of the wind speed about the mean wind speed U_{10} in a 10-minute period. The wind turbulence can be estimated using the turbelence intensity parameter I. The turblence intensity

is the ratio of σ_U to U_{10}. The U_{10} is usually measured every 10 minutes at a reference height location,H (H is typically 10m reference height) or calculated using the probability distribution with consideration of the return period, thus the mean wind speed at any height z above the sea level can be estimated using equation 2.1.

The standard deviation σ_U as described in equation 2.2.

$$\sigma_U = \left(\frac{U(H)}{\ln(\frac{H}{Z_0})} \right) + 1.28 \bullet 144 \bullet I \tag{2.2}$$

where Z_0 is the surface roughness and I is taken as 0.14 in for medium turbelence [79, 80] .

2.2.3. Turbsim

The turbulent wind field is generated using an application, Turbsim. The wind field is described by its height and width, known as the grid height b and the grid width a respectively. To generate a wind field using Turbsim, it is important select an appropriate wind profile and turbulence model that applies to the case under consideration [81]. **Figure 2.1** illustrates how VAWTs are positioned in the flow wind field. The reference wind speed is specified at the wind turbine hub height as indicated with red dotted line in **Figure 2.1.** Turbsim uses a statistical model to produce the time series of wind fields. Details of the input files can be found in is in **Appendix A.**

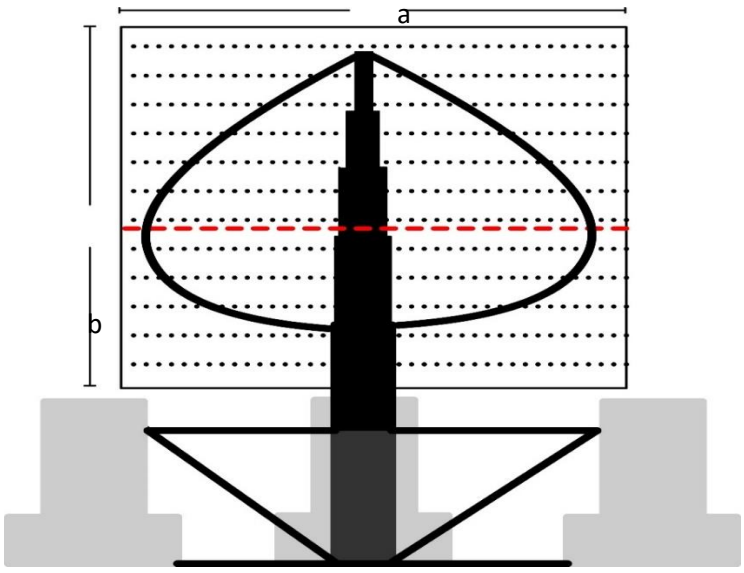

Figure 2.1: Artistic side view of a semi-submersible VAWT showing the flow field grid size and hub height.

2.2.4. Wind power of an ideal rotor

The non-dimensional power also known as the power coefficient CP, is used as an indication of VAWTs efficiency. This parameter is expressed as the ratio of the produced power to the available power in the swept area. The power coefficient is defined in (2.18).

In 1926, Betz [82] proposed a simple model applied in determining the power from an ideal wind turbine rotor including the wind loads on the ideal rotor and the effect of the rotor rotation on the local wind field. The Betz model is based on a linear momentum theory. The assumed control volume is bordered by the surface of a stream tube and two cross-sections of the stream tube with flow across the ends of the stream tube as shown in **Figure 2.2**. A uniform "actuator disk" is used to describe rotor which creates a discontinuity of flow pressure in the stream tube. Note that this analysis is not limited to any particular type of wind turbine. Betz's assumptions are as follows:

- Flow is homogenous, incompressible, steady
- Wake vorticity is neglected
- Frictional drag is neglected
- Uniform thrust over the rotor area
- The number of blades are infinite
- The static pressure far upstream and far downstream of the rotor is equal to the undisturbed ambient static pressure.

The net force on the control volume could be calculated by applying the law of conservation of linear momentum to the control volume. The net force is equal and opposite to the thrust T, according to Newton's third law, which is the force of the wind on the turbine rotor. Applying the law of conservation of linear momentum in one-dimension, for incompressible – steady state flow, the thrust is equal and opposite of the change in air stream momentum as indicated in equation 2.3:

$$T = U_1(\rho AU)_1 - U_4(\rho AU)_4 \tag{2.3}$$

where ρ is the air density, A is the cross sectional area, U is the air velocity and the subscripts indicate values at numbered cross sections in **Figure 2.2**.

For time invariant flow;

$$\dot{m} = (\rho AU)_1 = (\rho AU)_4 \tag{2.4}$$

where $\dot{m}$ is the stream mass flow rate.

Hence, equation 2.3 becomes;

$$T = \dot{m}(U_1 - U_4) \tag{2.5}$$

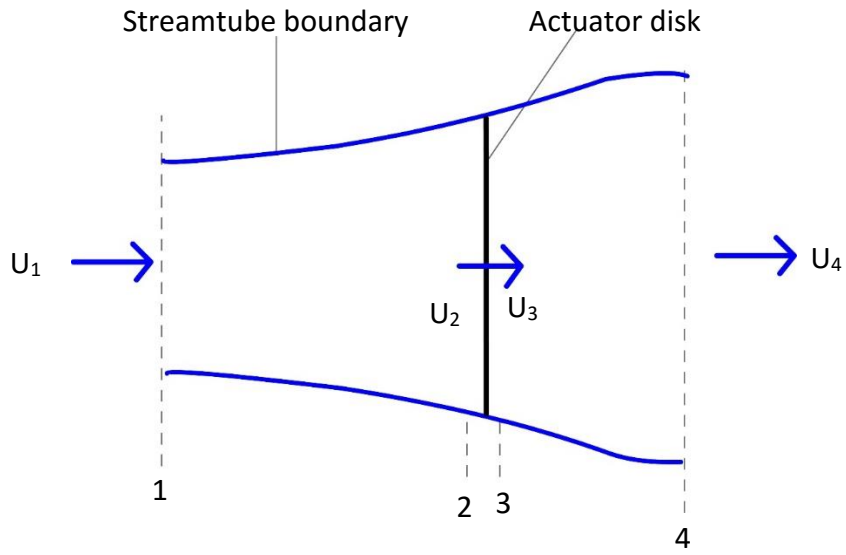

Figure 2.2: Actuator disk model of a wind turbine; U, is air velocity; 1, 2, 3 and 4 indicate locations [83].

The actuator disk model in **Figure 2.2** is like a diffuser, hence U_4 is less than the free stream velocity, U_1. This creates a positive thrust; and the net workdone on the turbine rotor is zero. Therefore, a simplified Bernoulli equation is applied on the two control volumes on either side of the actuator disk. In the upstream of the disk, the stream tube equation is;

$$P_1 + \frac{1}{2}\rho U_1^2 = P_2 + \frac{1}{2}\rho U_2^2 \tag{2.6}$$

In the downstream of the disk, the stream tube equation is;

$$P_3 + \frac{1}{2}\rho U_3^2 = P_4 + \frac{1}{2}\rho U_4^2 \tag{2.7}$$

The last Betz assumptions implies P_1=P_4 and that the velocities U_2 and U_3 at the two streamtubes interface remains the same. Thus, the thrust on the rotor can be represented as the net sum of the forces on each side of the actuator disk as in equation 2.8:

$$T = A_2(P_2 - P_3) \tag{2.8}$$

Combining (2.6) and (2.7) and substituting the value P_2-P_3 of into (2.8):

$$T = \frac{1}{2}\rho A_2 (U_1^2 - U_4^2) \tag{2.9}$$

Hence, the rotor disk power can be described by (2.10);

$$P = \frac{1}{2}\rho A_2 U_2 (U_1^2 - U_4^2) \tag{2.10}$$

Equating the thrust values from (2.3) and (2.9) to obtain (2.11) and since the mass flow rate is constant, the mass flow rate is A_2U_2 as well,

$$U_2 = \frac{U_1 + U_4}{2} \tag{2.11}$$

In (2.11), the wind velocity at the rotor plane is the same as the average of the upstream and downstream wind speeds. If the axial induction factor *a* is expressed as the fractional decrease in wind velocity between the free stream and that at the rotor plane, then;

$$a = \frac{U_1 - U_2}{U_1} \tag{2.12}$$

$$U_2 = U_1(1-a) \tag{2.13}$$

$$U_4 = U_1(1-2a) \tag{2.14}$$

From (2.12), (2.13) and (2.14), the axial thrust on the disk is:

$$T = \frac{1}{2}\rho A U_1^2 \left[4a(1-a)\right] \tag{2.15}$$

Similarly, (2.10) becomes;

$$P = \frac{1}{2}\rho A U_2 U_1^2 \left[4a(1-a)\right] = \frac{1}{2}\rho A U_1^3 \left[4a(1-a)^2\right] \tag{2.16}$$

The thrust on a wind turbine can be characterized by a non-dimensional thrust coefficient as:

$$C_T = \frac{T}{\frac{1}{2}\rho A U_1^{\,2}} = \frac{\text{Thrust force}}{\text{Dynamic force}} \tag{2.17}$$

In the same vein, the power coefficient is described in equation 2.18;

$$C_p = \frac{P}{\frac{1}{2}\rho A U_1^3} = \frac{\text{Power}}{\text{Dynamic power}} \tag{2.18}$$

From (12), the thrust coefficient and the power coefficient for an ideal wind turbine are 4a (1 − a) and $4a(1-a)^2$ respectively.

2.2.5. Aerodynamic loads

In the VAWT, the airfoils are rotating about the vertical. The relative flow velocity passing over the airfoils is the vector sum of the wind speed and the tangential speed induced by the VAWT rotation [57]. The angle of attack changes periodically during one revolution and its magnitude is dependent on the tip speed ratio. Furthermore, the angle of attack decrease at increasing tip speed ratios. The efficiency of the VAWT drops significantly at low tip speed ratios, hence, the blade airfoils stall. This effect occurs in VAWT during the following conditions:

- At very high wind speed, the rotor stalls.
- At very low rotational speed, the VAWT losses self-starting ability.

In order to solve the problems discussed above, the tip speed ratios must be sufficiently high such that the angle of attack resides within a certain limit value to prevent stall during one revolution and the blade elements operate at high efficiency, thus transmitting high torque to the rotor.

However, the value tip speed ratio cannot be infinity. In the same vein, at very high tip speed ratios, the airfoils has low efficiency because the angle of attack is very small. Consequently, at both very low and high tip speed ratios the wind turbine will operate at low efficiency. This implies that the wind turbine must operate within a range of favourable tip speed ratios to maximize the efficiency.

The periodicity of the angle of attack creates periodic loads on the either blades whose frequency is dependent on the frequency at which the rotor rotates. Therefore, loads and moment transmitted to the tower becomes periodical. The periodicity of transmitted loads and moments is dependent on the number of blade of the rotor, the periodic amplitude decreases as the number of rotor blade increases. Thus a two bladed VAWT has the maximum periodic amplitude. The rotor blades are flexible structural elements. Therefore, periodic loading on the blade will have significant impact on their fatigue life.

2.2.6. Aerodynamic models

The periodicity of the aerodynamic loads as discussed in the previous section introduces complexity in VAWTs aerodynamics. The aerodynamic loads on a Darrieus-type vertical axis wind turbine is significant influenced by the interaction between each of the turbine blades and either their own wakes and the wakes downwind of the second blade in the case of a two bladed rotor. The wakes vorticity and their interaction with the blade elements is one of the most complex problem in the numerical analysis of VAWTs aerodynamics [84].

Several numerical, theoretical and computational aerodynamic models have been developed and used to estimate the aerodynamic loads on VAWTs. These models are Blade Element/Momentum models (BEM) [67, 85-87], Actuator Cylinder flow model [88], vortex models [89-91], cascade models [92], panel models [93-95] and CFD simulation [83].

Blade Element/Momentum or stream-tube models are based on the conservation-of-momentum principle in a quasi-steady flow by equating the forces on the rotor blades to the change in the streamwise momentum through the turbine. Several stream-tube models have been develop over the years, however, they can be collectively categorized into three [71]:

- Single Streamtube model by Templin [85], assuming that the entire rotor represented by an actuator disk is enclosed in one streamtube;
- Multiple-Streamtube model by Strickland [86], in which the volume swept by the rotor is divided into a series of adjacent streamtubes
- Double Multiple-Streamtube model (DMS model) by Paraschivoiu [87], which assumes that the vertical axis wind turbine can be represented by a pair of actuator disks in tandem at each level of the rotor, as shown in **Figure 2.4.**

I. Single Streamtube model

Unlike HAWT, the projection of a VAWT rotor blades is similar to a cylinder that is parallel to the stream tube, this implies that the blades cut cross the normal actuator disc twice at both upstream and downstream the flow, as seen in **Figure 2.3**. Therefore, in place of a single line, the rotor could be represented as a zone in which the induction has to be determined.

In 1974, Templin proposed to use this method for VAWT aerodynamics. The induction factor a in the zone could be estimated by applying of the principle of flow continuity as shown in (2.21)

[96]. The induction factor is dependent on the magnitude of the rotor solidity s, the tip speed ratio λ and the azimuthal angle Θ. These non-dimensional parameters, a, s and λ are used to configure and scale wind turbines, irrespective of their actual dimensions. Equation (2.19) describes the rotor solidity which denotes that proportion of occupied area in the swept area. The tip speed ratio in (2.20) as explained in the previous sections describes how fast the VAWT rotates with respect to the flow speed.

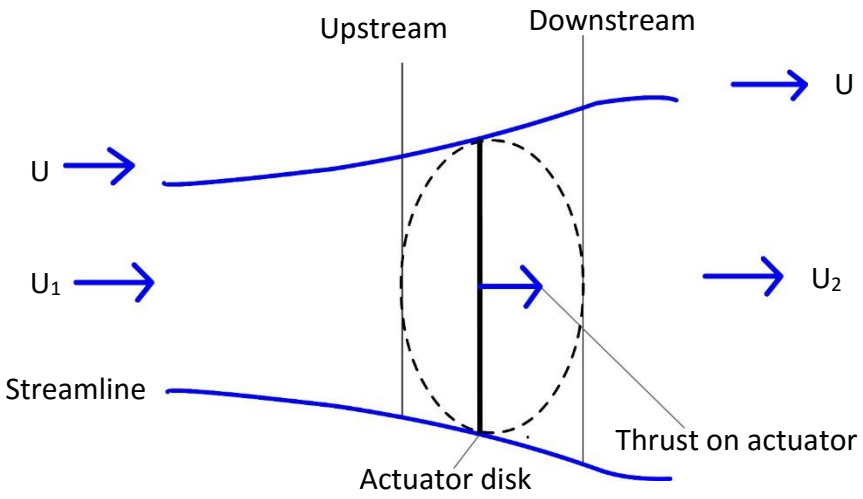

Figure 2.3: Single Stream Tube visualization

$$s = \frac{Nc}{2R} \tag{2.19}$$

$$\lambda = \frac{R\omega}{U} \tag{2.20}$$

$$a = \frac{s}{\pi}\lambda \sin\theta \tag{2.21}$$

The Single Streamtube model is simple but does not account for the interaction between blade and wakes. Furthermore, at downstream the disk, the flow is assumed reduced and undisturbed. These assumption and simplification results in inaccuracy in the aerodynamic load calculations.

II. Multiple Streamtube model

Multiple stream tubes are usually applied in BEM. The multiple streamtubes model is an extension of the Single Streamtube model, multiple streantubes are added to divide the zone into upstream and downstream tubes. This was followed by discretization of the swept area into independent multiple slices. See details of model in [58].

III. Double Multiple-Streamtube (DMS) models

The combination of the rotational speed ω, solidity σ and the amount of used stream tube pieces m. possible to compute the power produced at every actuator disk if the location of the blade is known. The relative velocity W is dependent on the azimuthal angle Θ as described the geometric relation in (2.22). The W and angle of attack α depend on the induction factor a. The induction factor has the same definition as in (2.12). The angle of attack is described in (2.23). The tangential force coefficient C_t is the sum of the projected lift C_L and drag C_D coefficients with the angle of attack α on the reference frame (2.24). The sum of all products of tangential force coefficient Ct and square of the non-dimensional relative velocity is the torque coefficient C_T as shown in (2.25). In 1988, Paraschivoiu [97] defined the non-dimensional power as the product of the torque coefficient C_T and the tip speed ratio λ, see (2.26).

$$\frac{W}{U} = \sqrt{((1-a)\sin\theta)^2 + \left((1-a)\cos\theta + \lambda\right)^2} \tag{2.22}$$

$$\alpha = \arctan\left(\frac{(1-a)\sin\theta}{(1-a)\cos\theta + \lambda}\right) \tag{2.23}$$

$$C_t = C_L \sin\alpha - C_D \cos\alpha \tag{2.24}$$

$$C_T = s\sum_{i=1}^{2m} \frac{\left(\frac{W_i}{U}\right)^2 C_{t,i}}{2m} \tag{2.25}$$

$$C_P = C_T\lambda \tag{2.26}$$

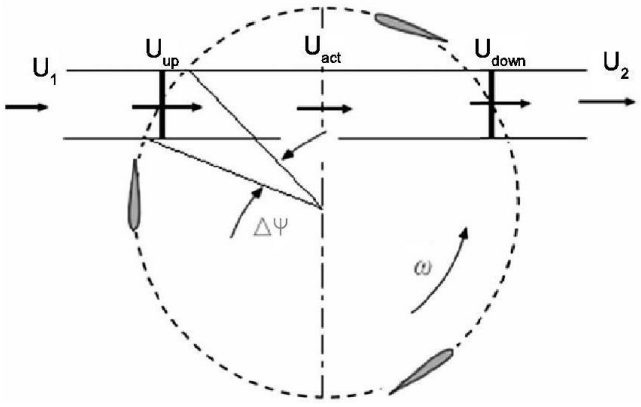

Figure 2.4: Double Multiple Stream Tube visualization with U_1 as the undisturbed wind speed.

The DMS model is described in **Figure 2.4** and has been discussed extensively by Paraschivoiu [27]. The downstream wind speed is assumed to have a lower free stream speed as compared with the upstream, as there was a reduction of energy at upstream. Furthermore, it was assumed the flow is undisturbed, irrespective of its position, which neglects the effect of the earlier shed wake. Moreover, it was also assumed that the induction factor is only parallel to the flow, however, as the VAWT rotates, it creates a lateral induction factor which is perpendicular to the flow. These assumptions account for the low accuracy of DMS.

In 2009, Ferreira [98] suggested a method to incorporate the lateral induction factor into the original DMS model by modelling the induction zone as a circulation or a small vortex in order to improve the DMS model. The results of the improved version of DMS model approaches the curve achieved with a vortex model as indicated in **Figure 2.5**. Although, the offset between the improved version of DMS and the vortex model is visible but the results from the original DMS model has been significantly improvement.

Although the DMS is a simple BEM tool with fast response, it has been criticised to over predict the power for high solidity VAWTs and experience the problem of convergence at higher tip speed ratio. However, in comparison among the streamtube models, the DMS model incorporates the variation of the induced velocity with respect to the azimuth angle for each streamtube, hence, the DMS model is more accurate. Only high fidelity models proved the inaccuracy of the DMS model [98].

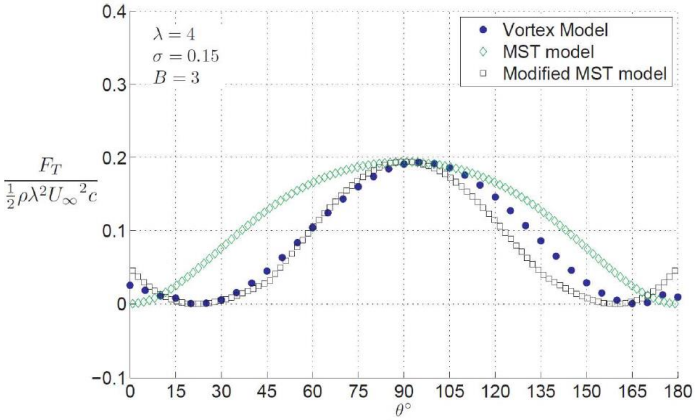

Figure 2.5: Comparison of tangential forces of a VAWT, between MST and a Vortex code [99].

IV. The Actuator Cylinder flow (AC) model

Madsen [88] extended the conventional Actuator Disk concept for HAWTs to an actuator surface coinciding with the swept area of the actual turbine to developed the Actuator Cylinder flow (AC)

model [100]. The Actuator Cylinder model (AC) uses a cylinder instead of a disc, which is more equivalent to the swept surface, especially with a straight bladed VAWT. The projection of the forces along the surface in tangential and normal direction is shown in **Figure 2.6b**. The AC is developed to project the forces in z-directions onto the cylinder surface, hence becomes a 2D solver.

The AC model estimates the aerodynamic loads on VAWTs based on their surface geometry. The real energy conversion of the 5 MW DeepWind VAWT rotor was simulated with the AC flow model [101] and implemented in the HAWC2 aeroelastic code as presented by Madsen et al. [102].

Madsen[102] applied the Euler and the flow continuity equation to determine the velocities in x and y direction as in (2.27) and (2.28) respectively. The power coefficient in (2.29) [101] can be estimated if the normal and tangential forces are determined and azimuth angle Θ is known. The Actuator Cylinder model has fast responses but more complex as compared with the DMS model. However, the AC model has been criticized of lacking blade-wake interactions as well.

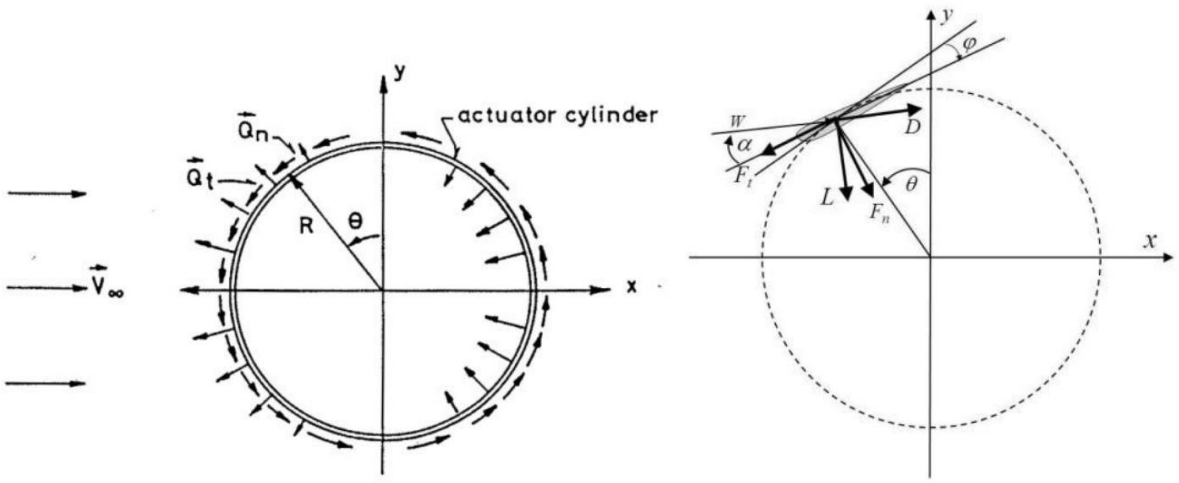

(a) The Actuator Cylinder flow model representation of a VAWT with volume forces normal and tangential to the circle [101].

(b): The blade forces projected on a direction perpendicular and tangential to the circular blade path.

Figure 2.6: The Actuator Cylinder flow model

$$U_x = -\frac{1}{2\pi}\int_0^{2\pi} Q_n(\theta)\frac{-(x+\sin\theta)\sin\theta+(y-\cos\theta)\cos\theta}{(x+\sin\theta)^2+(y-\cos\theta)^2}d\theta - Q_n(\cos^{-1}y)^* + Q_n(\cos^{-1}y)^{**} \quad (2.27)$$

$$U_y = -\frac{1}{2\pi}\int_0^{2\pi} Q_n(\theta)\frac{-(x+\sin\theta)\cos\theta-(y-\cos\theta)\sin\theta}{(x+\sin\theta)^2+(y-\cos\theta)^2}d\theta \tag{2.28}$$

$$C_P = \frac{\frac{1}{2\pi}\int_0^{2\pi} B(F_t(\theta))\cos\theta + F_n(\theta)\sin\theta\omega d\theta}{\rho U_1^3} \tag{2.29}$$

V. Vortex Models

In the vortex models, the velocity field about the rotor is estimated by assuming a potential flow through the influence of vorticity in the wake of the blades. The blades are divided into several blade elements with individual blade element representing a vortex filament known as the lifting line. The airfoil coefficient datasets and determined relative flow velocity are used to estimate the strengths of the bound vortices. For simplicity, the fluid velocity at any point in the flow field is assumed to be the undisturbed wind velocity and the velocity induced by all vortex filaments in the flow field. The vortex model applies the above assumptions in order to estimate the velocity field.

In 1975, Larsen [103] introduced a vortex model for a single blade element of a VAWT, this was extended by Fanucci and Walter [104] to a two dimensional models applicable to VAWTs, Holme [105] and Wilson [106] to a two dimensional models applicable to VAWTs. However, these models did not incorporate the rotor stall effect and only applied to lightly loaded wind turbine with small angles of attack.

Strickland et al. [91] in 1979 introduce a three dimensional vortex model and consequently improved the same [107] by accounting for the rotor dynamic effects like pitching circulation , dynamic stall and added mass. The improved model correlated better with the calculated values and results from experiment for the instantaneous blade forces and the overall power coefficients. Moreover, the improved 3D vortex model has been improved as well by Cardona [108], Vandenberghe and Dick [109].

Ponta and Jacovkis [110] divided the analysis into two separate regions: macro and micro models to combine the free-vortex model with a FEA of the flow within of the rotor. Although the effect rotor stall was neglected but could solve some problems associated with the previous vortex models and showed a better correlation with experimental results.

Brown's Vorticity Transport Model (VTM) [111] was developed in year 2000, in order to provide an accurate depiction of the wake dynamics that is generated by the turbine rotor. The VTM has been applied to evaluate the aerodynamic performance and dynamics of the generated wake of three VAWT concept both in steady and unsteady wind conditions [112]. The VTM used a structured Cartesian mesh within the fluid domain surrounding the turbine rotor to discretise the time-dependent Navier–Stokes equations in three-dimensional finite-volume form. It assumed that an incompressible wake is generated such that the Navier–Stokes equations can be cast into the vorticity–velocity form inrder to calculate the vorticity distribution in the flow surrounding the rotor. Scheurich et al. [89] validated the VTM by comparing the VTM's predicted blade aerodynamic loading of a straight-bladed vertical-axis wind turbine with the experimental measurements made by Strickland et al [107]. Consequently, the power curve from an experimental measurements of a commercial vertical-axis wind turbine with helically twisted blades made by Penna [113] used to compared the VTM predictions by Scheurich and Brown [114]. The comparison ensured confidence in the capability of the VTM model with respect to VAWTS aerodynamics as the VTM predictions correlated satisfactorily with experimental measurements.

VI. The cascades models

The cascade models was originally developed for turbo-machineries [115], however, it was proposed first in 1987 by Hirsh and Mandel [92] to adapt the principles in the cascade model for the analysis of VAWTs aerodynamics. The VAWT blades assumed to be positioned in a plane surface, also known as the cascade. The distance between adjacent blades is equal to the ratio of the turbine distance along the circumference to the number of blades, as described in **Figure 2.7.**

The Cascade model used a particular semi-empirical relation to express the relationship between the induced velocities to the wake velocity and further apply the Bernoulli's equation to associate the wake velocity with the free stream velocity. The cascade model showed more accurate prediction of the instantaneous blade forces although it requires more computational time as compared with the streamtube models. Moreover, its prediction is independent on the values of turbines solidity, and convergences at both high solidities and high tip speed ratios. The model was improved by Mandal and Burton to the dynamic stall effects and flow curvature with blade

pitching. The improved cascade model compared well with the improved three dimension vortex model by Strickland et al. [107] in terms of calculated values of the wake velocities.

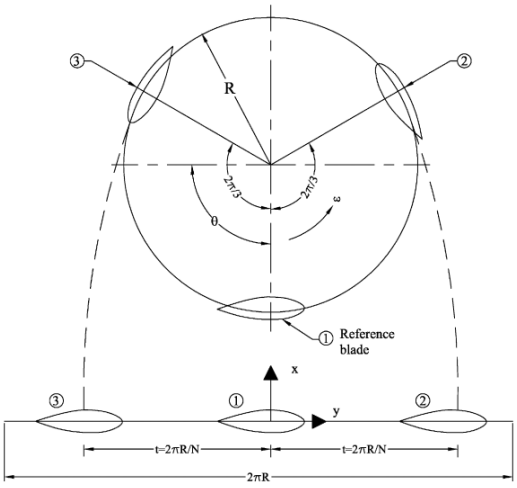

Figure 2.7: Development of blade into a cascade configuration[116]

VII. The panel model

The panel models is a widely applied model in naval hydrodynamics [117] and aircraft aerodynamics [118] and Erickson [119] in 1990, introduced this model. Modeling with this methodology starts with a discretization of a 3D surface into a number of panels. An arbitrary geometry for the hydrodynamic problems is obtained by placing source or doublet with a known strength on each panel and in terms of the velocity potential for a no penetration Dirchelet boundary condition on the body with the Kutta condition being enforced at the trailing edge, the Laplace equation is solved.

Simão Ferreira in his PhD thesis [98] developed a potential flow panel model.. This model a 2D distribution of source and doublet panels over the blade's surface is used to represent the individual blade. The Kutta condition is invoked at the trailing edge, the near-wake is modelled as doublets, while the mid and far wake modelled as vortex points. This model and the VTM model have been used by Simão Ferreira and Scheurich [95] to estimate the aerodynamic loads of a high aspect ratio H-rotor VAWT in order to show that the instantaneous blade aerodynamic loading and the power conversion of a VAWT are decoupled. Zanon et al. [90] applied a semi-inverse iterative algorithm for simulating the unsteady 2D flow past a VAWT to improve the 2D panel model to a double–wake vortex panel model coupled with the integral boundary layer equations on the aerofoil surface. This becomes a landmark as first thorough validation of a double-wake model with PIV data concerning a pitching aerofoil and a VAWT in dynamic stall.

Furthermore, the Stereo-PIV experimental results and SIMOke-trail studies by Dixon et al. [90, 94] has been used to validated a 3D unsteady panel model.

VIII. Numerical simulations

CFD (Computational Fluid Dynamics) models of the aerodynamics of vertical axis wind turbines has taken a new dimension with the availability of high-performance computers. Beri et al [83] and Hansen and Sørensen [120] have simulated the two-dimensional aerodynamics of an aerofoil for a VAWT in a planar and cyclic motion by solving the Reynolds-Averaged Navier-Stokes (RANS) equations.

Beri et al [83] applied a moving mesh technique (see **Figure 2.8**) to investigate the two-dimensional unsteady flow around a NACA0018 airfoil modified VAWT model and utilized fluent solving Reynolds average Navier-strokes equation.

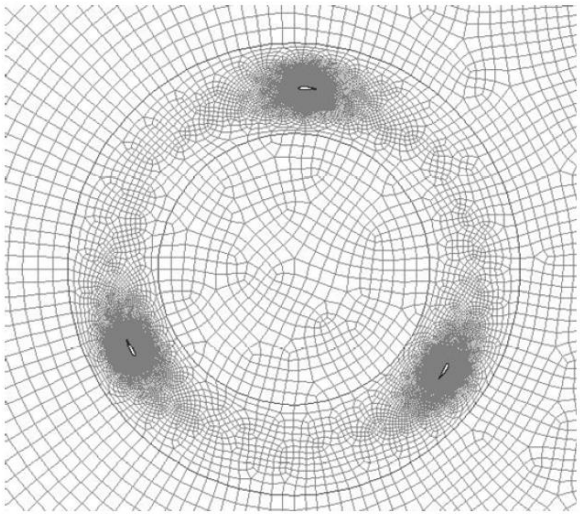

Figure 2.8: Mesh near the rotor. [83]

The results of the 2D RANS CFD simulation with the airfoil modified showed a better performance at low tip speed ratios for the modelled turbine as compared with that obtained from the DMS model. In contrast to the 2D RANS, Horiuchi et al [121] performed an detached-eddy simulations of a similar aerofoil configuration. consequently, a 2D CFD simulation of dynamic stall on a VAWT was carried out to verify and validate it with the Particle Image Velocimetry (PIV) measurements by Simão Ferreira et al. [122].

2.2.7. Dynamic stall

Secondary effects like the blade geometry and airfoil type, the rotating tower and the presence of struts and spoilers, are particularly significant at high tip-speed ratios and the influence of secondary effects on the aerodynamics of the Darrieus rotor and must be included in aerodynamic modelling of VAWTS to improve models accuracies. Dynamic stall is one of the most significant effects and occurs at low tip-speed ratios, when the amplitude of the oscillation of the angle of attack becomes large causing flow separation from the blade surface. This is because variation of the angle of attack with the azimuthal position during operation as well as the presence of a lower wind speed in the downwind zone from the wake of the upwind part of the rotor.

Dynamic stall is a complex and unsteady situation which has relationship with the time response of the viscous boundary layer. It causes the stall to occur at a higher angle of attack than for the static stall case, and is characterized by shedding vortices over the upper lifting surface. Firstly, the rotor experience a quick increase in lift and ends with full flow separation and then losses of lift in a catastrophic manner as the vortex disturbance is are carried across the trailing edge of the airfoil [123]. This creates cyclic pressure loading and hysteresis loops in the force coefficients that is not represented the steady airfoil data.

In predicting the dynamic stall of VAWTs, different empirical models with the fundamentals spanning from the numerical correction of the dynamic stall delay were developed including the Gormont's model [124] which was originally developed for helicopters or a model from the MIT by Paraschivoiu [125]. Strickland et al. [91], Paraschivoiu [125] and Berg [126] adapted the Gormont's model for analysis of VAWTs dynamic stall.

Furthermore, Wang in his PhD thesis [71], predicted the unsteady aerodynamics of VAWTs at a low tip speed ratio using Gormont's model with the adaptation of Strickland et al. [110] and with adaptation of Berg [151].

In his work, Wang proposed to compute the modified dynamic coefficients using linear interpolation between the dynamic coefficient predicted by Gormont's model and the static coefficient to avoid the drawbacks in Gormont's model. This model is denoted as ''Berg DS'' his analysis. However, some of the assumptions in the Gormont's Dynamic Stall model were

preserved. Thus, the two-dimensional force coefficient data as a function of $c\ \dot{\propto}/(2W)$ and other parameters (α_e, γ, K_1) was related by applying a modified angle of attack α_M as in Equation (2.30)

$$\alpha_M = \alpha_e - \gamma K_1 \left(\left| \frac{c\dot{\alpha}_e}{2W} \right| \right)^{\frac{1}{2}} S_{\dot{\alpha}} \tag{2.30}$$

where W represents the relative inflow velocity, α_e is the effective blade angle of attack, γ and K_1 are empirical constants, $\dot{\propto}_e$ is the instantaneous rate of change of α_e and $S_{\dot{\propto}}$ is the sign of $\dot{\propto}$.

Furthermore, Wang also adopted the Beddoes-Leishman dynamic stall (BL DS) [127] which has the ability of simulating the dynamic stall effect on helicopters, and the adaptation of this model has been validated for wind turbines by Gupta and Leishman [128]. The model consists of unsteady attached flow, unsteady separated flow and dynamic vortex lift. The summary of the load relations are in (2.31)-(2.35). Further details about is analysis is in [71].

The total normal force coefficient C_N^{Plot} under attached flow condition is given by

$$C_N^{Pot} = C_N^C + C_N^I \tag{2.31}$$

where C_N^C is the circulatory normal force coefficient and C_N^I is the impulsive normal force coefficient.

The unsteady chordwise force coefficient, C_C which is identical to the tangential force coefficient in this case, is obtained using the effective angle of attack α_e

$$C_C = C_N^C \alpha_e \tag{2.32}$$

Wang also modified certain parameters in the BL DS model for vertical axis wind turbine applications as stipulated in the AeroDyn Theory Manual of NREL [73]. Thus the model is capable of producing aerodynamic force coefficients over the entire range of possible angles of attack.

The chordwise force coefficient C_C is as presented in (2.33).

$$C_C = C_{N\alpha}\left(\alpha_e - \alpha_0\right)\alpha_e \sqrt{f_C^{''}} + C_N^v \alpha_e \left(1 - \tau_v\right) \tag{2.33}$$

where the $C_{N\propto}$ is the normal force coefficient curve slope, $f_C^{''}$ is the dynamic separation point function taking into account the temporal effects for chordwise force coefficient, C_N^v is the

normal force coefficient from the vortex lift contribution and τ_v is a non-dimensional parameter to track the position of the vortex across the airfoil.

Hence, the lift coefficient C_L and drag coefficient C_D are calculated from C_N and C_C by force resolution as presented in (2.34) and (2.35) respectively.

$$C_L = C_N \cos\alpha + C_c \sin\alpha \tag{2.34}$$

$$C_D = C_N \sin\alpha - C_c \cos\alpha + C_{d0} \tag{2.35}$$

where C_{d0} is the minimum drag coefficient corresponding to the zero angle of attack.

In this thesis, all assumptions and simplifications made by Wang [71] is adopted for the calculation of aerodynamic loads on the VAWT.

2.3. Waves

Waves are generated by wind actions. When the speed of the wind blowing over a large sea area for a long time increases, bigger waves are generated. However, wave growth does not only depend on the wind speed and time duration of the wind action but also on wave to wave interaction. Hence, smaller waves grow into higher waves by their interaction with wind and themselves by energy exchange [129].Wave loads creates similar load action effect as wind load but in addition generates cyclic loading on substructure as well as on the top part of the mooring lines. Wave loads have their greatest influence as shallow water is approached due to the wave shoaling phenomenon [130].

As waves approach shallow water, wave-energy transport velocity, changes. Under stationary conditions, the constant energy flux is kept constant by compensaring a decrease in transport speed by an increase in energy density. During shoaling, non-breaking waves will increase in wave height as the wave packet enters shallower water, hence a reduction in wavelength while the frequency remains constant is required to maintain the energy density. [131]. This is particularly obvious for tsunamis waves as they increase uncontrollable in height when approaching a coastline, with catastrophic results.

The wave condition in a sea state is categorized into *wind seas* and *swell*. Wind seas are generated by local wind, while swell have no relationship to the local wind. Swells are generated from wind blown over distant area and therefore are superposed into incoming sea wave. Swell can consist of several swell components at a given location [77]. The wind sea will follow the wind

direction, while the swell omni-directional. However, during analysis, both wind Sea and swell could be assumed to have the same direction of propagation in order to be conservative with an exception of weather vaning vessels. Therefore, analysis of vessels which are sensitive to different propagation directions should focus on identifying unfavourable short term sea states accounting for this fact.

The sea state is stochastic in nature and modelling of the sea state surface elevation is a complex task. Hence, several approximations and methodology are employed over the years to depict the sea state conditions. In an attempt to describe the sea state, the regular wave concept was introduced.

In general, waves are described as;

- Regular
- Irregular

2.3.1. Regular waves

Regular waves propagates with permanent forms with a propagation velocity also known as the phase velocity or wave celerity. They are described by distinct wave length, wave period and wave height. The wave length L and wave period T are the distance between successive crests and the time interval between successive crests passing a particular point respectively.

The propagation velocity of the wave form or wave celerity c is related to the wave length and wave period as represented in (2.36).

$$c = \frac{L}{T} \tag{2.36}$$

The wave frequency describes the number of cycles completed in a second. It is expressed as the inverse of the wave period in (2.37):

$$f = \frac{1}{T} \tag{2.37}$$

The wave angular frequency and the wave number are important parameter used to describe regular waves. The angular frequency Ω and the wave number k are related to the wave period and wave length as described in (2.38) and (2.39) respectively.

$$\Omega = \frac{2\pi}{T} \tag{2.38}$$

$$k = \frac{2\pi}{T} \tag{2.39}$$

The surface elevation z= η(x, y, t) is the distance between the still water level and the wave surface. The distance from the still water level to the crest is called the wave crest height A_C while the distance from the still water level to the trough is known as the wave trough depth A_T.
The wave height H which is the vertical distance from trough to crest is related to A_C and A_T by (2.40).

$$H = A_c + A_T \tag{2.40}$$

Regular waves can be categorised into:

- Linear
- Non-linear

Linear regular waves are symmetric about the still water level. This means A_C=A_T. However, non-linear regular waves are asymmetric, $A_C \neq A_T$ and the wave celerity depends on the dispersion relation which is a functional relationship between T, L and H.

The average wave energy density E is the summation of the average kinetic and potential wave energy per unit horizontal area. Thus, the energy flux P is defined as the average rate of transfer of energy per unit width across a plane normal to the propagation direction of the wave [132]. Hence, the speed of wave energy transfer known as the group velocity is related to P and E by (2.41).

$$C_g = \frac{P}{E} \tag{2.41}$$

Several wave theories such as the linear or airy wave theory, Stokes wave theory, Cnoidal wave theory, Solitary wave theory, Stream function wave theory have been developed for constant water depth d. The objective of a wave theory is to determine the relationship between T, L and the water particle motion throughout the flow. The relationship between wave period T, wave length L and wave height H for a given water depth d is called the dispersion relation.

The range of applicability of these wave theories in a specific problem are defined by three wave parameters determine which wave theory to apply. These are the wave height *H*, the wave period L and the water depth *d*. These three wave parameters are combined to form three non-

dimensional dependent parameters used in determining ranges of applicability of the various wave theories.

These non-dimensional parameters are as described in (2.42) to (2.44).

Wave steepness parameter: $$S=2\pi\frac{H}{gT^2}=\frac{H}{L_0} \quad (2.42)$$

Shallow water parameter: $$\mu=2\pi\frac{d}{gT^2}=\frac{d}{L_0} \quad (2.43)$$

Ursell number: $$U_R=\frac{HL^2}{d^3} \quad (2.44)$$

where L_0 is the linear deep water wave length corresponding for a wave period *T*. The range of validity of the various wave theories are represented in **Figure 2.9**. In **Figure 2.9,** the horizontal axis is a measure of shallowness while the vertical axis is a measure of steepness.

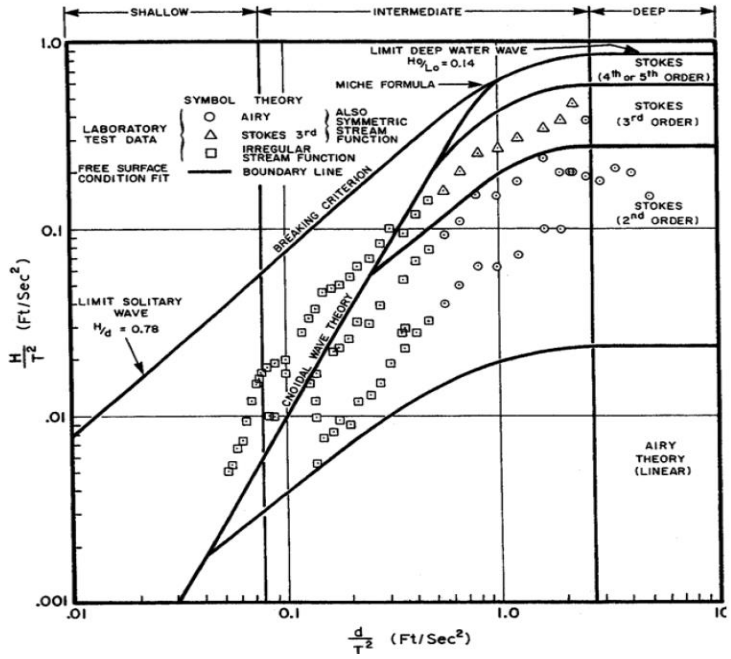

Figure 2.9: Ranges of validity for various wave theories. [133].

These different wave theories will not be discussed further for the purpose of this work. Find details of the respective regular wave theories in [77, 133]

2.3.2. Irregular waves

The free surface elevation z=η (x, y, t) in irregular or random waves is a stochastic in nature. Unlike regular waves, the local wavelength of irregular waves can be defined as the distance between two consecutive zero up-crossings. Furthermore, the global maximum between a positive up-crossing through the mean elevation, and the following down-crossing through the same level is used to describe the wave crest in irregular waves. A similar description is applicable to the wave trough.

In order to represent a real sea state, irregular random waves can be modelled as a summation of sinusoidal wave components. The simplest random wave model is the linear long crested wave model given by

$$\eta_{1\,(t)} = \sum_{k-1}^{N} A_k \cos\left(\omega_k t + \varepsilon_k\right) \tag{2.45}$$

where ε_k are randomised phases uniformly distributed between 0 and 2π mutually independent of each other with the amplitudes A_k which is a random variable taken to be Rayleigh distributed with mean square value given by

$$E\left[A_k^2\right] = 2S\left(\omega_k\right)\triangle\omega_k \tag{2.46}$$

Where S (ω) is the wave spectrum.

The irregular wave's kinematics can be predicted by Grue's method, Wheeler's method, Second-order kinematics model [77].

A sea state can be short-term or long-term sea condition. A long term sea state is characterised by return period or probability of exceeding a reference environmental parameter. However, in short- term sea states, the sea surface is assumed stationary for a duration of 20 minutes to 3-6 hours. A stationary sea state is described by a set of environmental variables such as the significant wave height Hs and the wave peak period Tp. The significant wave height Hs is defined as the average height of the highest 33.33 % waves measured within the time period, it is sometime represented by $H_{1/3}$. The inverse of the frequency at which a wave energy spectrum

has its maximum value is called the peak period Tp. The zero-up-crossing period T_z is the average time interval between two successive up-crossings of the mean sea level.

I. Wave spectrum

Wave spectrum are used to define the energy of a sea state within a short term condition. A short term sea state is generally characterized by the significant wave height, H_S, and the spectral peak period, T_P. However, in some cases, the wave direction, Θ, and wave peakedness, ɣ, are significant parameters which must be used to realise the random sea state. The sea state of any arbitrary combination of H_S, T_P will typically be of a combined sea surface which would represent the superposition of a locally wind generated sea and swell system [129].

Different spectra has been develop over the years to describe the short term realisation of the sea surface. These include the Pierson and Moskowitz (PM) spectrum, JONSWAP spectrum, Torsethaugen Spectral Model (TSM), etc.

Pierson and Moskowitz in 1964 [134] developed the PM spectrum. In the PM spectrum, it was assumed that if the wind blew steadily for a long time over a large area, the waves would come into equilibrium with the wind. This is the simplest concept of a fully developed sea. The PM model is represented mathematically as shown in equation (2.47):

$$S\left(f;h_s,t_p\right)=0.3125.h_s^{\,2}t_p\left[\frac{f}{f_p}\right]^{-5}\exp\left\{-1.25\left[\frac{f}{f_p}\right]^{-4}\right\} \tag{2.47}$$

The PM was extended by a group of researchers to include fetch limited seas, describing developing sea states. This forms the JONSWAP spectrum [135] is used to describe pure wind sea conditions. It is described in equation (2.28). However, both spectra describe wind sea conditions that often occur for the most severe sea states.

$$\mathrm{S}\left(f;h_s,t_p\right)=\mathrm{SPM}\left(\omega\right)\left(1-0.287In\gamma\right).\gamma^{\exp\left\{-0.5\left[\frac{f-f_p}{f_{p\sigma}}\right]^2\right\}} \tag{2.48}$$

where S_{PM} (ω) = Pierson-Moskowitz spectrum, σ =0.07 for $f_P < f$, and σ =0.09 for $f_P \geq f$. Therefore, the spectral peakedness parameter, γ, is calculated according to equation (2.49):

$$\gamma=\exp\left\{5.75-1.15\frac{t_p}{\sqrt{h_s}}\right\} \tag{2.49}$$

The Torsethaugen Spectral Model (TSM) [136], is a superposition of two JONSWAP spectra; representing a combination of a wind sea and a swell system and thus divides the hs – tp plane into a wind sea dominated region and a swell dominated region. The boundary, t_{pb}, between these regions is given by equation (2.50).

$$t_{pb} = 6.6\, h_s^{0.333} \tag{2.50}$$

In general, a local wind sea will have a spectral peak period lower than, t_{pb} ,while a swell or decaying wind sea will have a spectral peak period larger than, t_{pb},. The range at which a particular spectrum could be valid must be considered on a case by case basis when the analysis under consideration is known. As a rule of thumb, if the response of a given sea state is located within a +/- 2 limit around the boundary given by equation (2.50), the JONSWAP spectral model yields acceptable results because the JONSWAP spectrum yields larger response than the Torsethaugen spectrum within this range. The Torsethaugen model is a single peaked spectrum within this limit and double peaked outside the limit. Therefore, the Torsethaugen model (or equivalent models) should be used outside this range.

The JONSWAP spectrum is used to model irregular waves in this work.

This page is intentionally left blank

3 The 5 MW Baseline Floating Vertical Axis Wind Turbine

The novel FVAWT concept selected for this work is as shown in **Figure 3.1** and fully described in [69]. The design consists of a semi-submersible substructure [132] with a curved Darrieus VAWT [57] with the generator positioned at the tower base. The global motion of the semi-submersible substructure is limited by anchoring the platform to the sea bottom by means of conventional catenary mooring system. Furthermore, the sea water dampens the platform dynamics.

In this thesis, already proven tools and methodologies used by Wang [71] is adopted. This is the idea behind most of the modelling tool employed. This novel FVAWT concept has been used by Wang [74] for the design of a 5 MW VAWT.

3.1. The rotor

The curved Darrieus rotor has been chosen for the FVAWT concept analysed in this work among the various design rotor concept proposed for VAWTs in the past years because of the following reasons:

- The simplicity of the concept design.
- Darrieus rotor gives better up-scaling potential and it matches with the other components described in the next paragraph.
- The possibility of using blades with Troposkien shape, which can reduce the bending moment on the blades due to the centrifugal force.
- The power coefficient of Darrieus rotor approximately 0.4, which is close to the values reached with HAWTs [27] .
- The Darrieus rotor has a long research and development in history and thus can enhance parametric study and code to code verification.

Darrieus rotors usually consist of blades which twice or thrice that of a HAWT of the same rated power [27] as explained earlier. However, a longer connection arms can be introduced in

combination with a straight blades Darrieus rotor to reduce the length of the blade. Furthermore, the curved blades have been chosen for this work with the possibility of considering a modified Troposkien blade shape for the optimised 5 MW FVAWT concept.

The simplicity of the blade design ensures its suitability for the application of Pultrusion technology for the manufacturing process and in principle, the blades can be pultruded with a constant geometry along the length without tapering. The Pultrusion process [137] of GRP is a promising manufacturing method for producing large blade profiles. An advantage of the application of the Pultrusion process is that the material strength of pultruded GRP is much better than for hand laid-up GRP for horizontal-axis wind turbines with a significant reduction in the costs of manufacture. In fact, Migliore in 2000 [138] estimated up to 74%, reduction in the manufacturing costs in the production of blades for VAWTs compared with blades for HAWTs.
The tower is connected to the main column of the platform. Multiple bearings are used to ensure the tower do not rotate relative to the platform.

The airfoil is a symmetric NACA airfoil of 18% chord length thickness. The symmetric NACA profile is selected according to the earlier statement made in the previous chapter.
Therefore, the rotor properties are described in **Table 3.1**

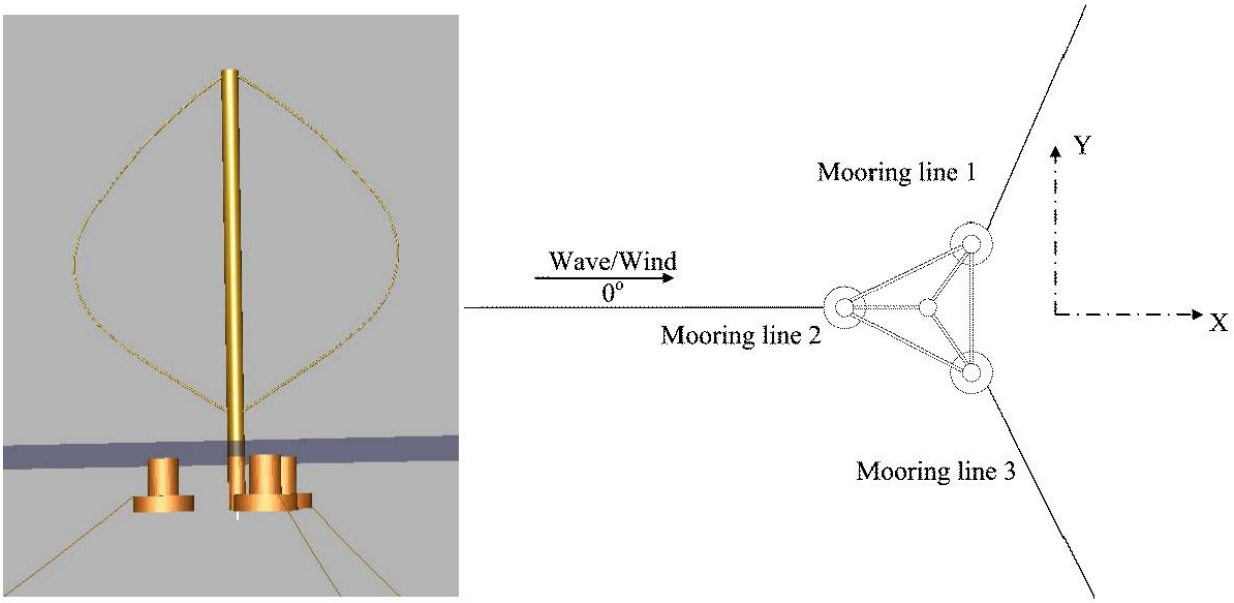

(a) Floating vertical axis wind turbine **(b)** Mooring line arrangement [71]

Figure 3.1: The FVAWT concept

Table 3.1: Technical and geometric properties of the 5 MW DeepWind turbine baseline design

Geometric and undistributed properties of the blade			
S/N	Properties	Unit	Magnitude
1	Rotor radius	M	63.74
2	Rotor height	M	129.56
3	Blade chord	M	7.45
4	Airfoil type		NACA0018
5	Solidity		0.1653
6	Length of one blade	m	188.86
7	Rotor mass	Kg	305044
8	Distance of hub height above MSL	m	79.78
Operational and Performance data			
9	Rated Power	MW	5
10	Rated rotation speed	rpm	5.26
11	Number of blades	-	2
12	Rated wind speed	m/s	14
13	Cut in wind speed	m/s	4
14	Cut out wind speed	m/s	25

3.1.1. The platform

A semi-submersible is selected for this work amidst several platform concept due to its desired characteristics over other platform concepts. The stability of the semi-submersible platform is achieved by its water plane stiffness in combination with the water ballast in the offset columns or pontoons.

As compared with a spar buoy, which obtains stability by having a deep draught ballasted substructure, a semi-submersible has a significant lower draught, and thus a more flexible concept with respect to changing environmental conditions, installation and transport. Furthermore, a spar wet tow either requires deep harbours and deeper seaways to be towed from the yard to the installation site, or a more sophisticated transportation and installation

method than what exists today. The lower draught of a semi-submersible ensures its suitability for intermediate water depths, and for shallow water assembly yards.

In this thesis, the semi-submersible depicted in **Figure 3.2** originally developed and used to support the NREL 5 MW HVAWT in the DeepCwind phase II of the OC4 Project [56] is selected to support the DeepWind 5 MW Baseline VAWT. DeepCwind is a U.S. - based project aimed at generating field-test data for use in validating floating offshore wind turbine modeling tools.

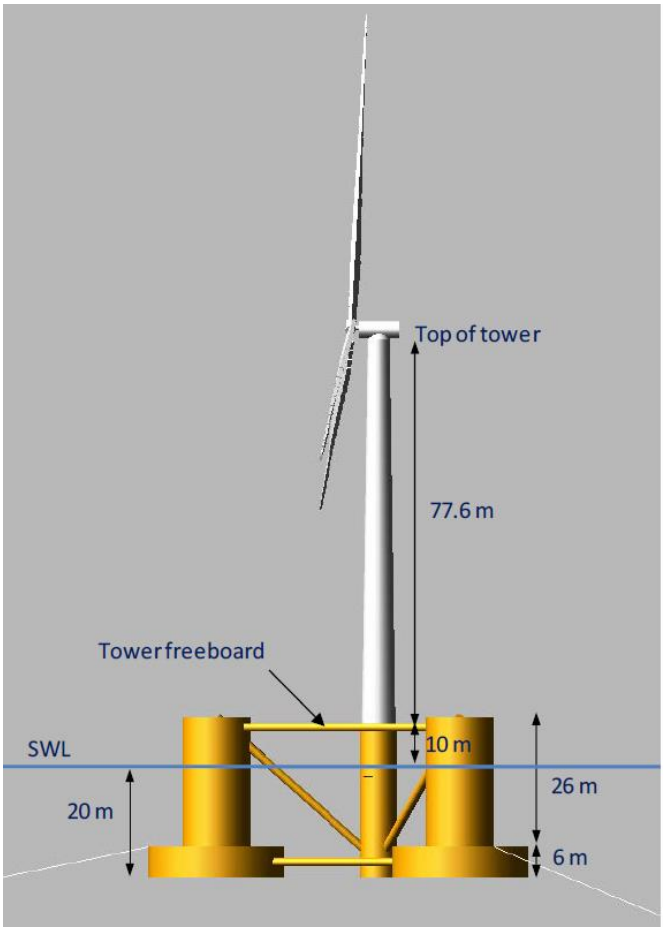

Figure 3.2: DeepCwind floating wind system design

The platform is a semi-submersible floater with four column and three pontoons. The columns consist of a main column CM located at the center and three offset columns. The offset columns are connected to the central column by 15 braces. Each offset column consist of an upper column UC and a base column BC also called the pontoon as shown in **Figure 3.3.**

As compared with the FHAWT in the OC4 project, this thesis adopted the 5 MW Darrieus rotor instead of the NREL 5 MW reference HAWT turbine. The 5 MW Darrieus rotor is heavier than the NREL 5 MW HAWT. Hence, Wang in his PhD thesis [71] slightly modified the ballast water of the

original semi-submersible in order to fit it to the specification of the VAWT discussed in the previous section. This modified platform is adopted in this work.

The specification of the modified semi-submersible as represented in **Table 3.3**.

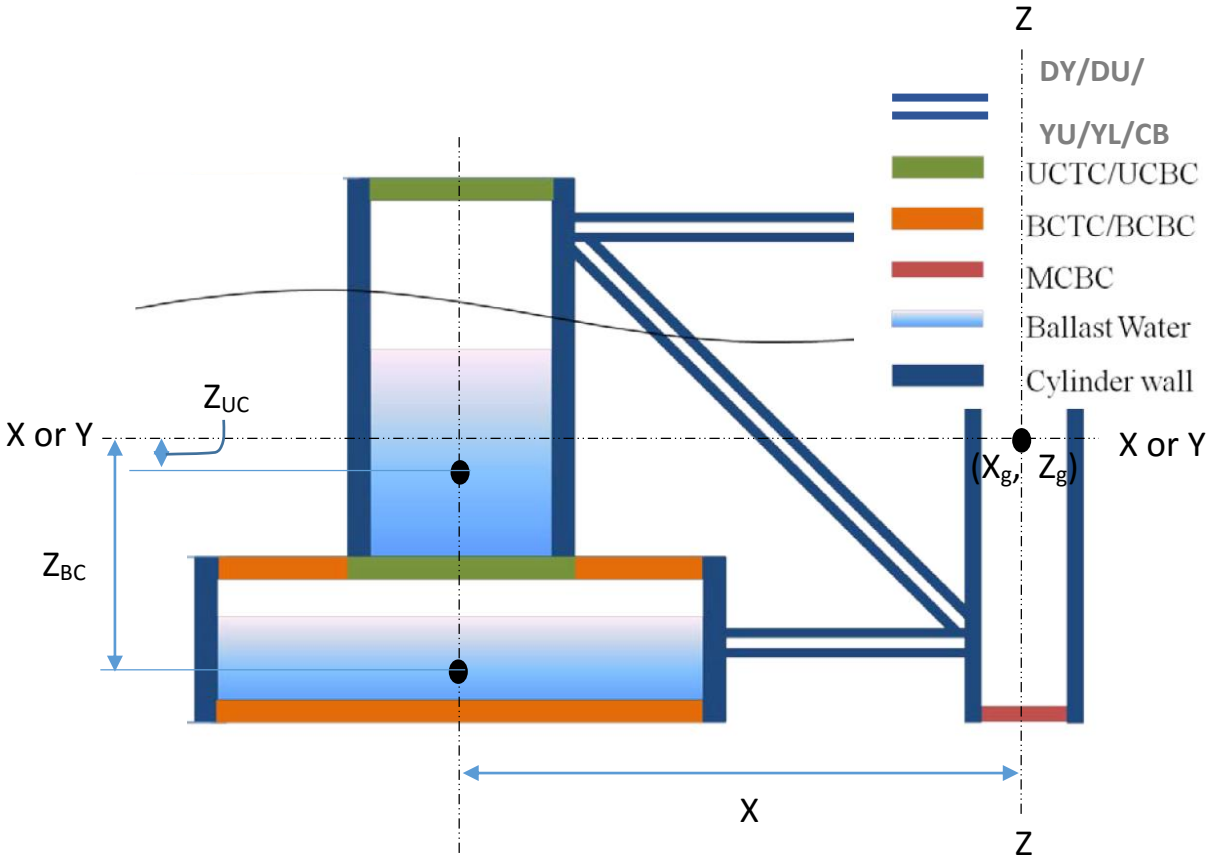

Figure 3.3: Side view of platform walls and caps (abbreviations can be found in **Table 4.2**)[56]

Table 3.2: Platform abbreviatios in **Figure 3.3**

S/N	Abbreviations	No of component	Description
1	DU	3	Set of braces connecting the offset columns in a triangular (or delta) pattern at the top
2	DL	3	Set of braces connecting the offset columns in a triangular (or delta) pattern at the top
3	YU	3	Braces connecting the offset columns with the main column in form of a y-connection at the top
4	YL	3	Braces connecting the offset columns with the main column in form of a y-connection at the bottom

5	CB	3	Set of three cross braces connecting the bottom of the main column to the top of the offset columns
6	UCTC	3	UC top cover
7	UCBC	3	UC bottom cover
8	BCTC	3	BC top cover
9	BCBC	3	BC bottom cover
10	MCBC	1	MC bottom cover

Table 3.3: Geometry, Structural and hydrodynamic properties of platform configuration

S/N	Floater Properties	Unit	Magnitude
1	Depth of platform base below SWL (total draft)	m	20
2	Spacing between offset columns	m	50
3	Platform mass, including ballast and generator	t	13353.7
4	CM location of total concept below SWL	m	8.66
5	Buoyancy in undisplaced position	t	14267.41
6	CB location below SWL	m	13.15
7	Hydrostatic restoring stiffness in heave C33	N/m	3.836E+06
8	Hydrostatic restoring stiffness in roll C44	N.m/rad	-3.77E+08
9	Hydrostatic restoring stiffness in pitch C55	N.m/rad	-3.77E+08
10	Moment of inertia in roll	t.m2	9159733
11	Moment of inertia in pitch	t.m2	9159733
12	Moment of inertia in yaw	t.m2	12087187

3.1.2. Generator

The generator is mounted on the bottom of the VAWT unlike the case for horizontal axis wind turbine. The generator operate at variable speeds to control the turbine operations. The rotor torque is transmitted through the shaft to the generator. Furthermore, a direct drive is assumed to be positioned inside the central column of the platform, hence the gearbox is not considered in the model and the mass of the generator is summed into the total mass of the platform.

3.1.3. Mooring system

The rotor torque is transmitted through the shaft to the generator. Therefore, the semi-submersible is moored with three catenary lines spread symmetrically about the platform *Z*-axis to secure the platform to the seabed. The mooring layout plan view is as shown in Figure 3.1(b) .

The fairleads (body-fixed locations where the mooring lines attach to the platform) are positioned at the top of the base columns at a depth of 14.0 m below the SWL and at a radius of 40.87 m from the platform centerline. The anchors are positioned at a water depth of 200 m. One of the lines is aligned along the negative *X*-axis (in the *XZ*-plane). The two remaining lines are evenly spaced around the platform, in a manner that the fairleads and anchor points are 120º apart when viewed from the plan as shown in **Figure 3.1(b)**. These properties described the undisplaced platform position. Drag and added mass of the mooring lines due to both hydrodynamic loading and seabed interaction are also considered with the structural damping of the mooring line is set to 2% stiffness proportional damping [56]. **Table 3.4** describes the mooring properties.

Table 3.4: Mooring System Properties

S/N	Mooring line properties	Units	Magnitude
1	Depth to Anchors Below SWL	m	200
2	Depth to Fairleads Below SWL	m	14
3	Radius to Anchors from Platform Centerline	m	837.6
4	Angle Between Adjacent Lines	Degree	120
6	Unstretched Mooring Line Length	m	835.5
7	Mooring Line Diameter	m	0.0766
8	Equivalent Mooring Line Mass Density	Kg/m	113.35
9	Equivalent Mooring Line Mass in water	Kg/m	108.63

3.1.4. Safety and Emergency system

The VAWTs are weaker than HAWTs in avoiding over-speeding conditions. Indeed the most common HAWTs are nowadays pitch controlled and can use aerodynamic brakes in addition to a mechanical brake system. FVAWTs with semi-submersible substructure requires a big mechanical

brake system at the bottom of the VAWT, sometimes consisting of two brakes, one on each shaft (low and high speed).

However, Wang in his work [74], carried out numerical simulations based on the coupled non-linear time domain code for a floating vertical axis wind turbine with hydrodynamic brake (See **Figure 3.4(b)**). Furthermore, the effect of using the hydrodynamic brake -FVAWT system was evaluated by comparing the results obtained for the FVAWT with hydrodynamic brake with the results obtained for the original FVAWT under normal operating conditions. The results showed the combination of a mechanical brake with a larger hydrodynamic brake could successfully shutdown the process. The application of a hydrodynamic brake is expected to be efficient for rotor shutdown and for reducing the platform motion and structural loads.

For a floating VAWT, the application of hydrodynamic brakes are expected to be efficient for shutdown, reduction of the platform motion and structural loads including over-speeding protection.

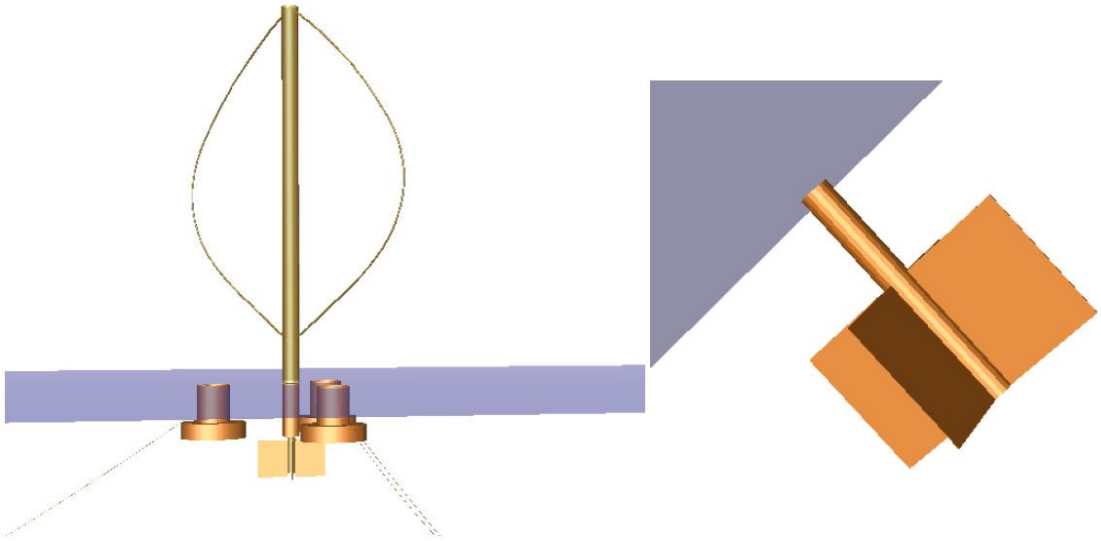

(a) Floating vertical axis wind turbine (b) Hydrodynamic brake[74]

Figure 3.4: FVAWT model with hydrodynamic brake system

3.1.5. Control methodology

The VAWT does not require a pitch nor a yaw control system as compared with a HAWT. The power control is obtained by rpm control of the rotor speed [139]. Hence, this solution is simple and favourable for model up-scaling purposes.

3.1.6. Potentials of the FVAWT concept

The most obvious advantage of the concept is simplicity. The whole construction is simply a rotor supported by the semi-submersible. The blade is as well of a simple concept. Furthermore, large blade sections can be pultruded in GRP in a small to medium scale production facilities. In principle, a small scale production facility can be integrated on a ship, and the blades can be produced offshore in lengths of kilometres. Moreover, the blade could as well be manufactured at shore to prevent the limitations connected with land transportation of blades. Consequently, the FVAWT requires no yawing control system to position the rotor towards the wind direction and no pitching of blades is necessary to regulate power. The Darrieus rotor is also stall-controlled at high wind speeds, or the power can be downregulated by reducing the rotor speed. Additionally, over-speeding protection could be achieved efficiently by applying hydrodynamic brakes.

3.1.7. FVAWT concept challenges

The generator advantage with a large mass located at the bottom of the rotor is advantage. However, it introduce complexity in maintenance and complication in exchange of the component. Furthermore, lifting the generator through the central column which is a small parts must be technically evaluated.

The cost of manufacturing a blade of such geometry is also a challenge. However, the pultrusion of GRP in full blade length sections that are bent into the blade shape and glued together seems most be the promising method of manufacture.

Unlike HAWT, VAWT relies on the substructure system to absorb the rotor torque. This may be through the use of torque arms connected to the anchoring system or through drag elements in the water. The torque of the Darrieus rotor varies with the azimuthal angle and this varying torque will also have to be absorbed through the anchoring system [57].

This page is intentionally left blank

4 The Optimised 5 MW Floating Vertical Axis Wind Turbine

The Optimised 5 MW FVAWT differs from the baseline 5 MW FVAWT concept as highlighted below:

- Optimised rotor weight and blade geometry and cross-section
- Tower weight and geometry
- Modified semi-submersible total weight and inertia

The control, mooring, and generator as described in section 3 is adopted for the Optimised 5 MW FVAWT. The subsequent sections provide detail information of the optimised components of the baseline FVAWT.

4.1. The optimised DeepWind 5 MW rotor design

The curved Darrieus rotor shown in **Figure 4.1** was selected for the 5 MW FVAWT baseline design. The FVAWT rotor has a total blade weight of 154 tons per blade with chord of 7.45 m, details of the baseline design is found in [55] .

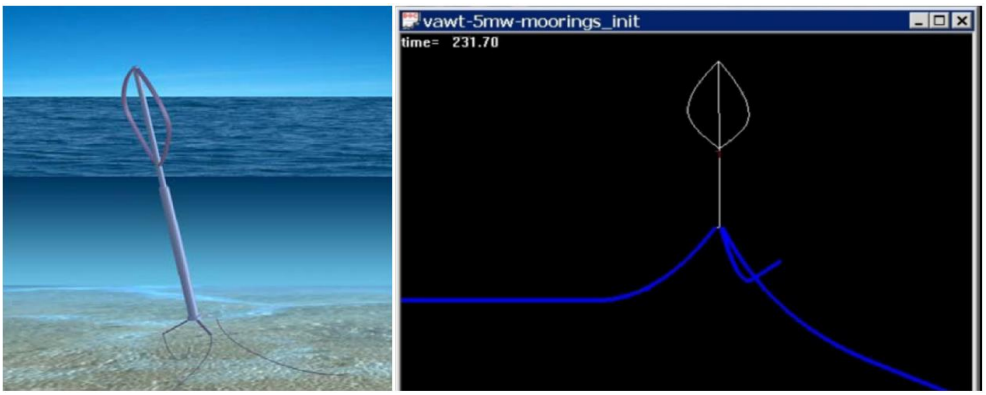

(a) Vertical-Axis Darrieus concept for deep sea. Rotor height is 130m and the rotating floater 107m long. **(b)** A 5 MW DeepWind turbine concept with mooring lines modelled in HAWC2 [50].

Figure 4.1: The concept for the baseline VAWT rotor

However, the large weight of the baseline design has significant negative impacts on the systems design, cost of manufacture and cost of maintenance. Hence, there was need to explore an alternative blade designs with piecewise constant blade chord and/or thicker profiles. The technical and geometric properties of the 5 MW DeepWind baseline VAWT design is as summarized in **Table 3.1.**

4.1.1. Summary of the Research at DTU for the Optimised Rotor

I. Blade Optimisation

A group of researchers at DTU considered alternative concepts to mitigate the enumerated disadvantages associated with the 5 MW baseline FVAWT rotor. The desired structural properties to be obtained in the optimised design cum the material cost reduction were the two basic design drivers that influenced the selection of the aerofoil profile and blade section piece dimensions. However, the reduction in the rotor weight could lead to reduced sectional load capacity. Thus, the optimization process was aimed to explore possibilities of reducing the weight of the 1st 5 MW baseline design by using the sectioned blade arc to ensure the minimum blade stain is less than 5000 μm/m throughout the blade length [140].

In the first iteration process, three NACA aerofoil profile - NACA0018, NACA0021 and NACA0025 (see **Table 4.1**) of uniform blade cross-section was investigated using a finite element code - ANSYS to select the aerofoil profile with minimum strain and moment distribution along the profile [75]. At this stage, a rotor height and cord length of 143m and 5m respectively was used to analyse the three aerofoil profile individually, see **Figure 4.2**.

The three aerofoil was modelled with an aero-hydrodynamic-elastic code- HAWC2 [61] and then investigated for strength. The results showed the NACA0025 has higher stiffness and lower strain (see **Figure 4.3**). Moreover, NACA0025 has the highest weight (see **Table 4.1**) among the three aerofoils, thus, it was imperative to carry out a second iteration to investigate the possibilities of combining the desirable properties of NACA0025 with the other airfoils of lower weight into the baseline model. Therefore, a second iteration was carried out to reduce the blade weight by zoning the blade length into three sections. From the ANSYS calculations, the blade base and the tip experienced the highest strain and thus, NACA0025 was adopted for the section at the base of the base (section 1) due to its high stiffness property.

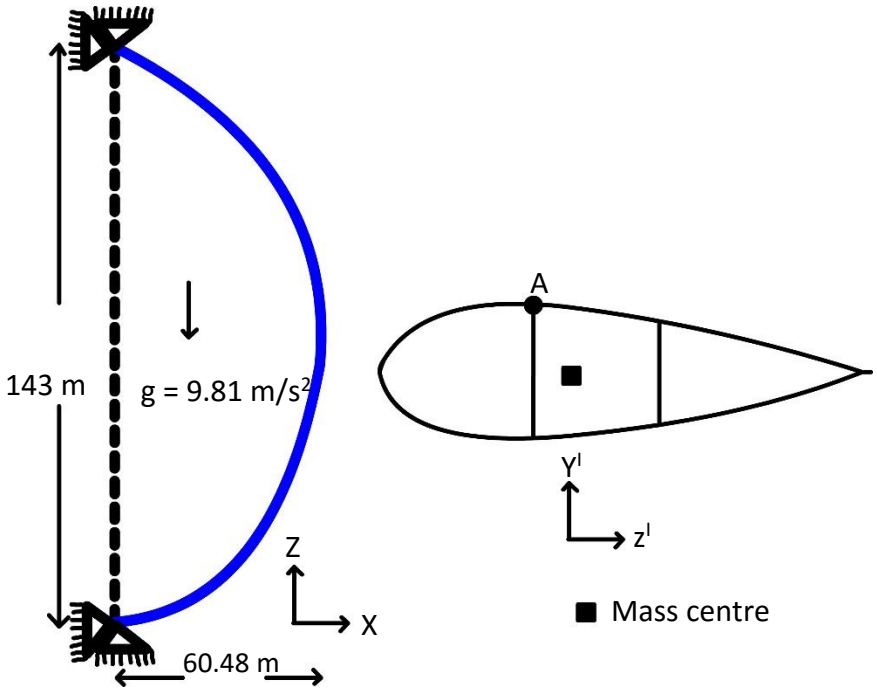

Figure 4.2: Schematic of standstill simulation with the rotor is subjected to self-weight.

Table 4.1: Aerofoils properties with chord length of 5m and rotor height shown in **Figure 4.2**.

S/N	Properties	Unit	NACA0018	NACA0021	NACA0025
1	Sectional area	m^2	0.1217	0.1262	0.1323
2	Specific mass	Kg/m	219.2	227.2	238.1
3	Area moment of inertia about z^I axis	m^4	0.0117	0.0163	0.0237
4	Area moment of inertia about Y^I axis	m^4	0.2504	0.2607	0.2748

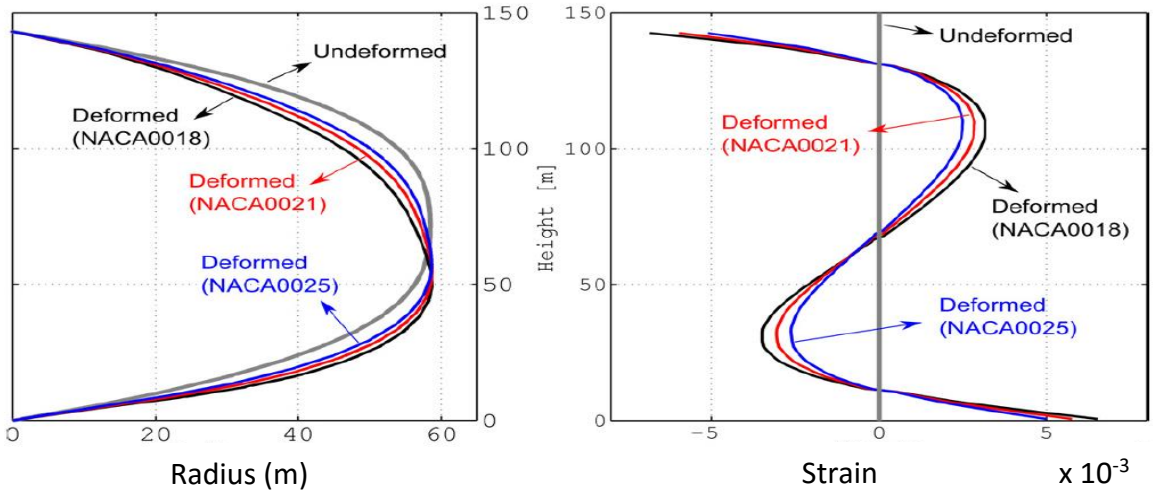

(a)ANSYS calculations of the deformation of the rotor. **(b)** Corresponding strain distributions for the rotor at point A (see **Figure 5.2**).

Figure 4.3: Results from ANSYS analysis of various airfoil

Consequently, the high rigidity of the fasteners at the blade tip were expected to minimize the strain at the tip such that any of the aerofoil profile could be used at the top zone (section 3). The sectioned blade is as described in **Figure 4.3**. The blade was sectioned into three parts with the arrangement as shown in **Table 4.2** to form two blade cases.

Table 4.2: Description of rotor sections.

S/N	Cases	Section 1	Section 2	Section 3	Total weight
1	Case -1	NACA0025	NACA0021	NACA0018	45670
2	Case -2	NACA0025	NACA0018	NACA0021	45844

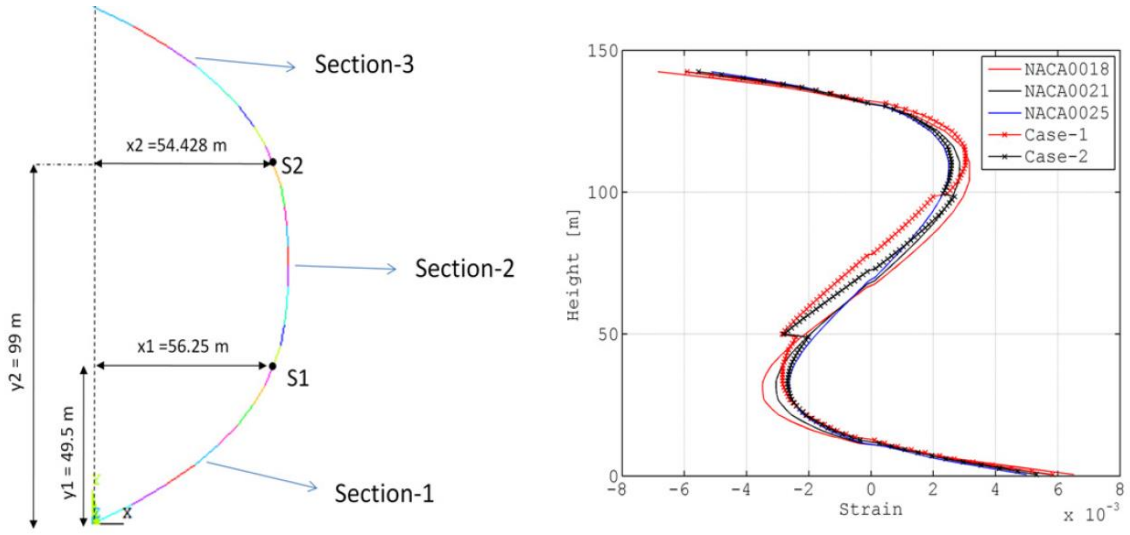

(a) The sectioned rotor and **(b)** the ANSYS calculations of the strain distributions throughout the rotor for point A (**Figure 4.2**) [75] .

Figure 4.4: Results from analysis of sectioned blade

From **Figure 4.4 (b)** the case-2 blade section arrangement showed a smaller strain as compared with the other blade profiles. Therefore, the case-2 blade section arrangement was investigated further using HAWC2. The results from HAWC2 are as shown in **Figure 4.5** and **4.6**.

The results of the 2nd iteration resulted in a new rotor design. The properties of the new rotor is as shown in **Table 4.3**.

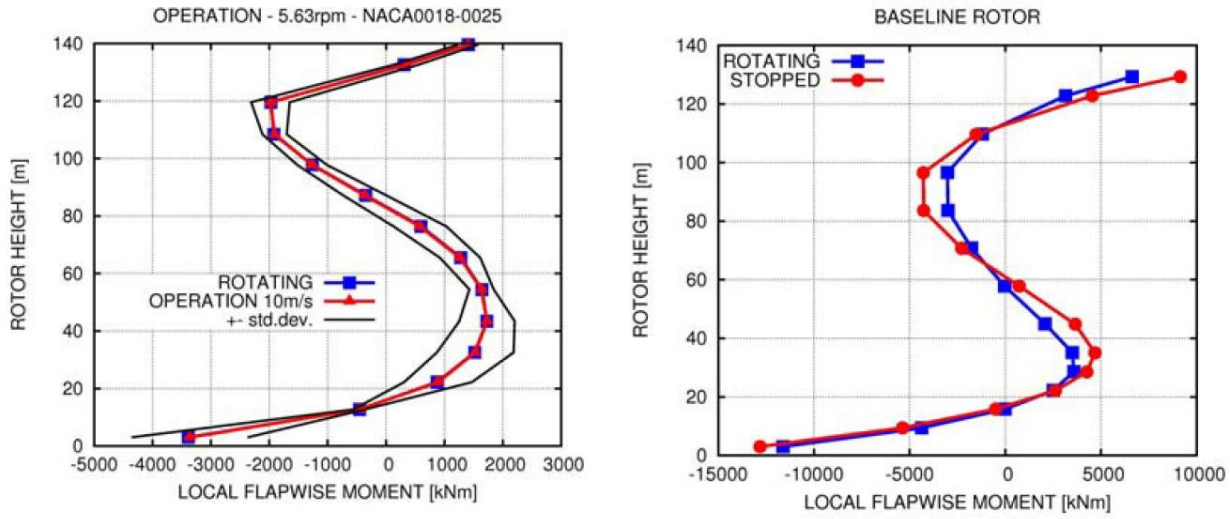

(a) influence of operation on the flapwise moment from 2nd iteration and **(b)** on the 1st baseline 5 MW design [75]

Figure 4.5: Results from analysis of case-2 blade section

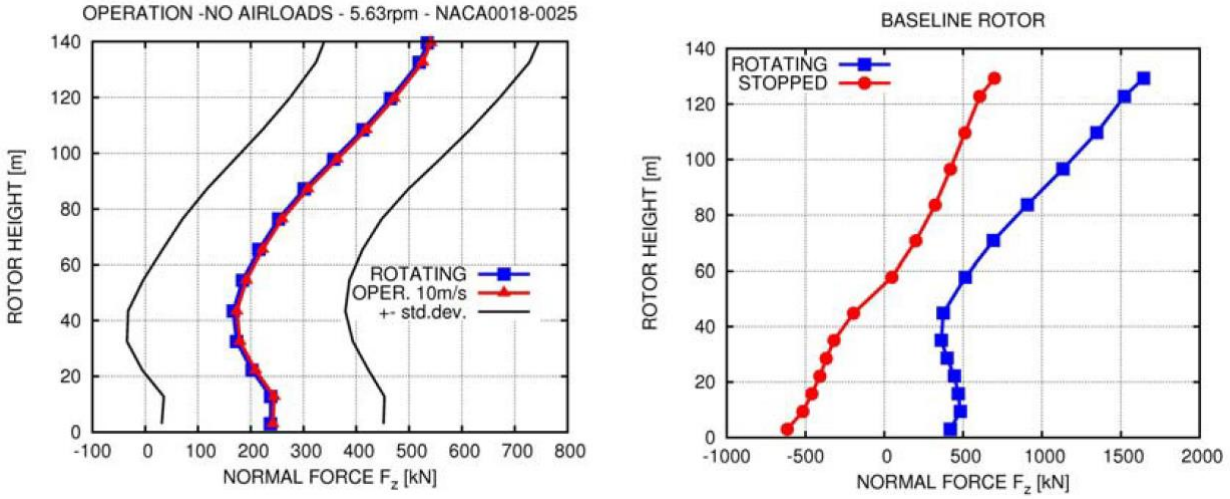

(a) Influence of the operation on the normal force. Left: 2nd iteration results. **(b)** 1st baseline 5 MW Design [75].

Figure 4.6: Results from case-2 iterations

Table 4.3: The optimised blade properties (Case -2)

S/N	Properties	Unit	Value	% change from the baseline design
1	Rated power	KW	6200	+ 24.0
2	Rated rpm	RPM	5.63	+7.00
3	Solidity		0.15	-32.90
4	Rotor radius	m	60.49	-5.10
5	Rotor height	m	143	+10.40
6	Swept area	m^2	12318	+14.70
7	Chord	m	5	-32.90

Moreover, there was increased pressure drags in the case -2 base design and hence HAWC2 simulation and a wind turnel validation test was conducted at low reynold number (10^6) in order to further optimise the concept [141]. This resulted in the development of several other aerofoil profile with DU12W262 having a greater performance in terms of power coeffiecient up to 0.48 when results were extrapolated to a Reynold number of 10^7 (for easier comparison with the NACA0018 of the 5 MW baseline design). The DU12W262 profile is an assymetric aerofoil profile with 26.2% thickness and high stiffness.

However, the symetric NACA0025 and NACA0018 profiles were selected to be used as the base profiles due to the following advantages as summerized below [142]:

- The blade structural properties are similar to the suggestions for the thick profile
- The profile thickness can easily be changed for parametric studies.
- Data availability for comparative studies and model validatation.

Therefore, it was proposed to use the NACA0025 at section 1 & 3 (see **Figure 4.7)** and the NACA0018 at section 2. Also, section 2 has morethan 80% of the total blade length (see **Figure 4.8)**.

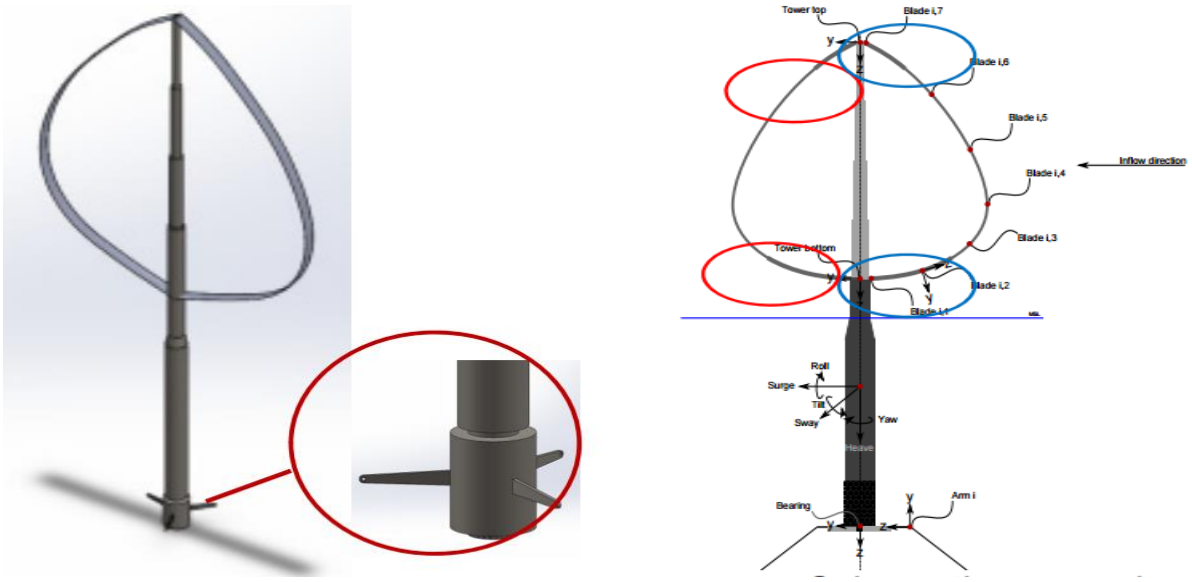

(a) 3D drawing of 5 MW concept. Detail of generator and torque absorption system shown
(b) Schematic overview of the 5 MW optimised DeepWind, with blade sections connections (section 1 and 3 are represented with blue circles).

Figure 4.7: Detailed description of the optimized rotor

However, for simplicity, time-constraint and easy model comparison with the 5 MW VAWT Baseline model, the symmetric NACA0018 is used for all blade section in this thesis. The optimised rotor properties as used in this thesis are summarised in **Table 4.4**. The details of the blade cross-sectional properties used to modelled in Riflex can be found in [73].

Table 4.4: The properties of the 5 MW optimised DeepWind rotor

Geometric properties				
S/N	Parameter	Symbol	Unit	Value
1	Rotor radius	R	m	60.48
2	Rotor height	H	m	143
3	Chord	C	m	5
4	Solidity = Nc/R	σ		0.1653
5	Rotor weight (2 blades)	W	Tons	96.06
6	Airfoil type NACA0018			
Technical properties				
7	Rated power	P	MW	5
8	Rated rotational speed	Ω	RPM	5.73
9	Rated wind speed	V	m/s	14
10	Cut in wind speed	Vi	m/s	4
11	Cut out wind speed	Vo	m/s	25

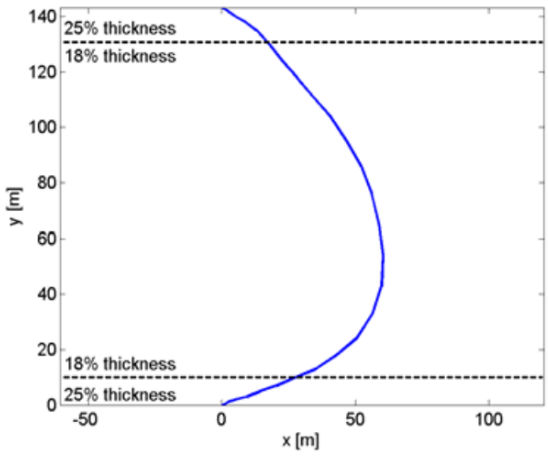

Figure 4.8: DeepWind modified troposkien rotor blade shape [143].

II. Tower Optimisation

The rotor tower weight was as well reduced in order to reduce the overall rotor weight. It could have been much easier to reduce the weight of the tower by reducing the crossection linearly from the base to the top. However, to consider the varation of aerodynamic load with altitute and positions of larger bending moments, the tower is sectioned into four parts as shown in **Figure 4.7** in such that the section with largest bending moment (the base) has the largest cross-section and the details of the tower properties are summarized in **Table 4.5**. The optimised (sectionized) tower weighs apprioximately 75 tons, lesser than the baseline tower [73]. The tower is a construction steel material with desity of 7805 kg/m^3.

The details of the 5 MW optimised DeepWind rotor in **Table 4.4** is combined with the DeepCwind semi-submersible from the OC4 project [56] to model the Optimized 5 MW FVAWT. The semi-submersible is again slightly modified as discussed in the next section to maintain the same draft as the original floater.

Table 4.5: Tower cross-sectional properties

Section	Radius (m)	Thickness (mm)	EI_y / EI_z (Nm2)	EA (N)	GJ (Nm2/rad)
1	4.62	15.00	4.6860e+11	9.2469e+10	3.6149e+11
2	5.32	17.00	2.9294e+11	6.9350e+10	2.2598e+11
3	5.84	18.00	2.0907e+11	5.9667e+10	1.6128e+11
4	6.40	21.90	1.2080e+11	4.5719e+10	9.3188e+10

4.1.2. Methodology for Platform modification

The 5 MW optimised DeepWind rotor has about 41% weight reduction from the 5 MW VAWT Baseline design rotor weight. Furthermore, if the Optimized rotor is modelled directly, the draft of the platform will increase. This will result in increased tension in mooring lines because the length of the mooring and position of fairleads are unchanged. Therefore, the semi-submersible from the DeepCwind phase II of the OC4 Project[56] must be slightly modified to maintain the same draft as the original platform. This is achieved by increasing the mass of ballast water.

The following assumption, approximation and notation are applied to successfully modify of the platform;

- The ballast water is sea water with density ρ = 1.025t/m^3
- From the platform detailed specifications [56], 25% and 75% of ballast mass are placed in the Upper UC and Base BC offset column respectively. No ballast in centre column CM.
- At the platform un-displaced position, the ballast mass geometry can be assumed as solid cylinder with mass M (t).
- The FVAWT is assumed symmetrically loaded and thus the method of the buoyancy compensating force [144] is applied in SIMO.
- The distance from the centre of mass of ballast water to the CM equals the distance from the centre of mass of UC or BC to CM.

The platform without the VAWT is assumed neutrally buoyant which in reality, it is the weight of the floating body including the VAWT that is neutrally buoyant. SIMO assumed the effects of gravity and buoyancy in the equations of motion is taken into account through the restoring matrix. However, in Riflex, it is assumed the finite element method includes both gravity and buoyancy as nodal forces. Hence, a buoyancy and a gravity compensating force, acting at the centre of buoyancy COB and centre of gravity COG as in **Figure 4.9**, must be respectively specified in SIMO to annul this inconsistency. This method of modelling coupled SIMO-Riflex system is known as the Method of Buoyancy Compensation Force.

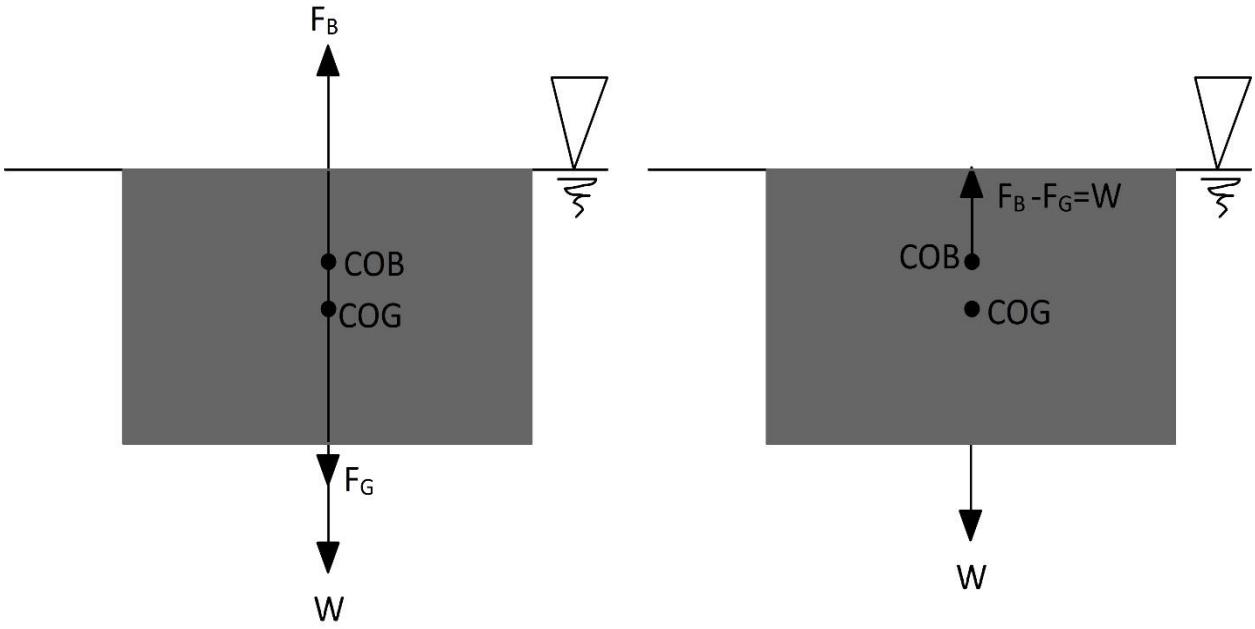

(a) Forces acting on the neutrally buoyant model. (b) SIMO interpretation.

Figure 4.9: Load interpretation as used in SIMO

Figure 4.9 is a description of the physical model of a symmetrically loaded FVAWT. This ensures the additional force W acting on the body due to weight of the flexible elements is cancelled out by the submerged force F_B-F_G. This will give a correct static configuration and reduce instability with running the analysis.

The following methodology is used to modify the platform in order to support the Optimised 5 MW FVAWT. Furthermore, this approach also works well for other scenario, where a platform weight need to be slightly modified to maintained the same platform draft as the original in order to adopt the platform for a wind turbine of different weight. However, some of the equations only need to be applied appropriately to reflect the uniqueness of case under consideration.

1. Calculate the submerged mass from the original platform submerged volume (submerged volume can be calculated or taken from platform information) as shown in (4.1).
2. To maintain the same draft, submerged mass of both the original platform and the modified platform must be equal as shown in (4.2).
3. Calculate the mass of modified platform M_P by subtracting the total mass of flexible elements M_F as in (4.3).
4. Calculate the mass of ballast water for both the modified M_B and original platform M_{BO} by subtracting the total platform metal mass M_M from M_P as in (4.4). The mass of ballast water for the original platform M_{BO} may be given from platform specifications. However, (4.4) can be used also to calculate $M_{BO.}$
5. Find the respective distance X, Z_{UC} and Z_{BC} from the ballast centre of gravity at UC and BC to platform centre of gravity (X_g and Z_g) for both modified and original platform, see **Figure 3.3**.
6. Calculate the mass of ballast water per $\mathrm{M_{B_{UC}}}$ and $\mathrm{M_{B_{BC}}}$, see (4.5).
7. Calculate the mass moment of inertia $\mathrm{I_{O/M_{XX\ or\ YY}}}$ and $\mathrm{I_{O/M_{ZZ}}}$ due to the mass of ballast water about the three axis of rotation taking the third assumption into consideration, see (4.6) and (4.8). This must be done for both the original and modified platform.
8. Subtract the inertias $\mathrm{I_{O_{XX\ or\ YY}}}$ and $\mathrm{I_{O_{ZZ}}}$ calculated in step 7 from the respective total platform inertias $\mathrm{I_{TO_{XX\ or\ YY}}}$ and $\mathrm{I_{TO_{ZZ}}}$ and then add the inertias due to mass of ballast of the modified platform $\mathrm{I_{M_{XX\ or\ YY}}}$ and $\mathrm{I_{M_{ZZ}}}$ calculated in step 7 to the respective to obtain the total inertias of the modified platform $\mathrm{I_{TM_{XX\ or\ YY}}}$ and $\mathrm{I_{TM_{ZZ}}}$ about the three axis of rotation as described in (4.9) and (4.10).

The submerge mass Δ is expressed as;

$$\Delta = \rho\nabla \tag{4.1}$$

Where ∇ is the submerged volume of platform + turbine un-displaced position.

$$\Delta_{\text{Modified}} = \Delta_{\text{Original}} \tag{4.2}$$

$$M_P = \Delta_{\text{Modified}} - M_F \tag{4.3}$$

$$M_B = M_P - M_M \tag{4.4}$$

From the second assumption, the ballast mass per UC is expressed as:

$$\begin{aligned} M_{B_{UC}} &= \frac{25}{100}\frac{M_B}{n_{UC}} \\ M_{B_{BC}} &= \frac{75}{100}\frac{M_B}{n_{BC}} \end{aligned} \tag{4.5}$$

Where n_{UC} and n_{BC} are number of UC and BC in the platform.

The mass moment of inertia of the ballast mass about the Z-Z axis is given based on the parallel axis theorem as:

$$I_{O/M_{ZZ}} = \sum_{i=1}^{n_{UC}}\left(\left(\frac{R_{UC_i}^2 M_{B_{UC\,i}}}{2}\right) + X_i^2 M_{B_{UC\,i}}\right) + \sum_{i=1}^{n_{BC}}\left(\left(\frac{R_{BC_i}^2 M_{B_{BC\,i}}}{2}\right) + X_i^2 M_{B_{BC\,i}}\right) \tag{4.6}$$

Where R_{UC} and R_{BC} are the radius of the upper and base offset column respectively minus the wall thickness.

Applying the Perpendicular Axis Theorem, the moment of inertia of a rigid object about the Z-Z axis perpendicular to the X-Y plane axis is given by:

$$I_{ZZ} = I_{XX} + I_{YY} \text{ For symmetric object, } I_{ZZ} = 2I_{XX} \tag{4.7}$$

Applying (4.7), the mass moment of inertia for the X-X axis of rotation is:

$$I_{O/M_{XX}} = \sum_{i=1}^{n_{UC}}\left(\left(\frac{R_{UC_i}^2 M_{B_{UC\,i}}}{4}\right) + \frac{L_{UC_i}^2 M_{B_{UC\,i}}}{12} + Z_{UC_i}^2 M_{B_{UC\,i}}\right) + \sum_{i=1}^{n_{BC}}\left(\left(\frac{R_{BC_i}^2 M_{B_{BC\,i}}}{4}\right) + \frac{L_{BC_i}^2 M_{B_{BC\,i}}}{12} + Z_{BC_i}^2 M_{B_{BC\,i}}\right) \tag{4.8}$$

The platform is symmetric, hence $I_{O/M_{XX}} = I_{O/M_{YY}}$.Therefore, the mass moment of inertia for the modified platform is given by (4.9) and 4.10) below:

For X-X or Y-Y axis;

$$I_{TM_{XX}} = I_{TM_{YY}} = I_{TO_{XX\text{ or }YY}} - I_{O_{XX\text{ or }YY}} + I_{M_{XX\text{ or }YY}} \tag{4.9}$$

Similarly, for Z-Z axis;

$$I_{TM_{ZZ}} = I_{TO_{ZZ}} - I_{O_{ZZ}} + I_{M_{ZZ}} \tag{4.10}$$

However, the calculated moment of inertias are with respect to the centre of gravity or local coordinate. To apply this into the symmetrical structural mass, they must be transformed to the global coordinate system as described in (4.11) :For more detail, see the SIMO manual [145].

$$\begin{aligned} RIXX &= I_{TM_{XX}} + M_B(Y_g^2 + Z_g^2) \\ RIYY &= I_{TM_{YY}} + M_B(X_g^2 + Z_g^2) \\ RIZZ &= I_{TM_{ZZ}} + M_B(X_g^2 + Y_g^2) \end{aligned} \tag{4.11}$$

The change in platform weight as a result of the change in ballast mass must be accounted for in the calculations for the hydrostatic stiffness data. Hence, the part of the restoring terms C(4,4), C(5,5) in the hydrodynamic stiffness data is calculated according to (4.12) to obtain the modified $C(4,4)^{New}$ and $C(5,5)^{New}$ [146].

$$\begin{aligned} C(4,4)^{New} &= C(4,4) - M_O g Z_{g_O} + M_P g Z_g \\ C(5,5)^{New} &= C(5,5) - M_O g Z_{g_O} + M_P g Z_g \end{aligned} \tag{4.12}$$

Where M_O and Z_{gO} are the total mass and centre of mass along the Z-axis of the original platform, g is the acceleration due to gravity.

The buoyancy force and COB remains the same as the original platform, hence its contribution to the restoring term is zero.

The summary of the structural, geometric and hydrodynamic properties of the platform in its un-displaced position are described in **Table 4.6**.

Table 4.6: Platform properties

Properties	Units	Magnitude
Platform total draft (below MSL)	m	20.00
Spacing between offset column	m	50.00
Total mass of ballast water	t	9671.97
Total platform mass, including ballast and generator	t	13614.11
Location of CM of FVAWT (platform + turbine) below MSL	m	-10.72
Submerged mass of FVAWT	t	14267.41
Location of COB of FVAWT	m	13.15

Hydrostatic stiffness in heave C33	N/m	3.836×10^6
Hydrostatic stiffness in roll C44	N.m/rad	-3.776×10^8
Hydrostatic stiffness in pitch C55	N.m/rad	-3.776×10^8
Moment of inertia in roll (RIXX)	$t.m^2$	9327626.10
Moment of inertia in pitch (RIYY)	$t.m^2$	9327626.10
Moment of inertia in yaw (RIZZ)	$t.m^2$	12319270.23

.

This page is intentionally left blank

5 Modelling of Floating Vertical Axis Wind Turbines

The interaction between aerodynamic and hydrodynamic loads including the interaction with the controller results in non-linear loading and accounts for large FVAWT dynamics. Therefore, dynamic structural analysis is necessary for structural design in all limit states of floating wind turbines. In this chapter, the dynamic response analysis methodology including the post-processing tools are presented.

5.1. Dynamic Modelling of FVAWTs

FVAWTs in normal operating condition will experience both cyclic and non-cyclic loading resulting from waves, wind and rotor motion. Cyclic loads causes fatigue damage in structural elements. Furthermore, secondary effects from wind such tower tilting are considered significant in this work. Therefore, a static approach is considered insufficient in the modelling of these dynamic effects, hence a dynamic analysis is adopted.

5.1.1. Equation of motion

For a submerged rigid body with 6 degrees of freedom, the linearized equation of motion and external actions can be expressed in the frequency domain as in (3.2) [147] . External forces such as wave forces, current forces, mooring forces or other external forces are represented by F (ω) forces in (5.1).

$$(M+ A(\omega)\ddot{x}(\omega) + B(\omega)\dot{x}(\omega) + Cx(\omega) = F(\omega) \quad (5.1)$$

In time domain, the solution of (5.1) must be performed by iteration at each time step for non-linear systems. Therefore, the Cummins equation can be applied to transform (5.1) to a non-linear time domain model as depicted in (5.2), which introduces an impulse-response (memory) function into the equation of motion[147]. The (5.2) known as the Duhamel's integral which

accounts for frequency dependent added mass and linear radiation damping in the time domain [148].

$$(M+ A^{\infty}) \ddot{x}(t) + \int_0^t \kappa(t-\tau)\dot{x}(\tau)\,d\tau + Cx(t) = F(t) \tag{5.2}$$

5.1.2. Non-linear FEM

Finite Element Analysis (FEM) is a numerical integration method which approximates the solution of the differential equations of motion by dividing the structural component into smaller elements with a reduced number of displacement patterns.

In non-linear FEM, secondary effects like the effects of large displacements, non-linear material behaviour or changing boundary conditions are accounted for in the solution. These effects introduce a memory effect, and traditional structural mechanics principles like superposition of loads and responses are considered insufficient. Furthermore, non-linearity could also be introduce by non-linear formulations of loads.

In FVAWT modelling, the relevant non-linearity are related to geometric structural non-linearity, i.e. the effects of large displacements, and quadratic load formulations in the thrust and drag forces. The Riflex program addresses the geometric non-linearity.

For a non-linear system of infinite elements in dynamic equilibrium, the non-linear equation of motion as in (5.3) can be expressed by global matrices that contain the mass, damping and stiffness properties of the finite elements [149]. External forces are weight, buoyancy, forced displacements from attached bodies, viscous drag and wave acceleration forces, including wind forces from DMS.

$$(M^S + M^H)\ddot{r}(t) + C^S\dot{r}(t) + K^S(r(t)) = R^{EXT}(r(t),\ddot{r}(t)) \tag{5.3}$$

Where R^{EXT} consist forced displacements, velocities and accelerations from the rigid floating substructure motion in the coupled solution.

Geometric non-linearity are significant for FVAWTs because of large deflection of the blades and in mooring lines. The Riflex code (FEM solver) applies the Newmark-β method implicit integration to find the dynamic equilibrium at each time step [149]. The parameters in this method control the accuracy, numerical stability and numerical damping of the integration method, and allows unlimited displacements, but assumes small strains [42].

5.1.3. Coupled Analysis

Floating Wind turbines consist of two dependent components; the floating substructure and the wind turbine. The dynamic response analysis of the individual component (substructure or turbine) can be performed with software and analysis tools that are conventional within the respective offshore and wind industries. This is usually the case for bottom fixed offshore wind turbines. However, in FVAWTs, coupling effects from among the substructure, moorings and flexible turbine dynamics is significant and thus, a coupled analysis must be performed.

In bottom fixed offshore wind turbines, the floating substructure is modelled with a hydrodynamic software and analysed by rigid body dynamics. The turbine is modelled as flexibles, slender FEM. The Finite Element solver is hence separate, and separate analysis of the floating substructure and the turbine will not include coupling effects between them. However, to take the coupling effects into consideration, the two solvers must exchange information at each time step of the analysis.

In FVAWTs, the considered coupling effects are usually [150];

- Aerodynamic damping from the rotor on floater motion
- Floating substructure motions influence the wind force
- Mean position of the floating substructure influences wind force and mooring force
- Mooring line dynamics (inertia and damping) influences floating substructure motion

The rigid body and the flexible elements are connected at common super nodes in coupled analysis. Although the dynamic equilibriums for the flexible element system and the rigid body are resolved separately in time domain, but at the same time, information about external forces and displacements are exchanged between the two solvers at each time step [149]. Therefore, equilibrium is attained for both FEM equation and rigid body motion by iteration at each time step.

In (5.2), the force vector F (t) which also includes the non-linear restoring, inertia and damping from the mooring lines, wave forces, wind forces and inertia and damping forces from the turbine in a coupled model is represented in (5.4).

$$F(t) = F^{wave}(t) + F^{wind}(t) + F^{turbine}(t) + F^{mooring}(t) \quad (5.4)$$

5.1.4. Coupled Modelling Tool for the Floating Vertical Axis Wind Turbine

A fully coupled simulation tool Simo-Riflex-DMS as used in Wang PhD thesis [71] is adopted for the time domain simulation of the FVAWT dynamics. The Simo-Riflex-DMS code consist of separate models for the wind inflow, aerodynamics, hydrodynamics, structural dynamics and controller dynamics integrated together to form a coupled whole. The SIMO code estimates the rigid body hydrodynamic forces and moments on the floater; the Riflex is a finite element solver used to model flexible element such as the blades, tower, shaft and mooring system, it also provides the link to the DMS code and external controller; the DMS code calculates the aerodynamic loads on the blades using an external aerodynamic module. Java script was to write the generator torque characteristics. SIMO implementation computes the hydrodynamic loads at the actually displaced position of the floater, DMS calculates the aerodynamic loads on the blades and Riflex carries out full equilibrium iteration at each time step [71, 151]. Simo-Riflex-DMS is a sophisticated aero-hydro-servo-elastic simulation tool which coupled a comprehensive hydrodynamic model, a stable non-linear finite element solver, a well-known aerodynamic code and a user-defined controller model. This coupled code has been presented and verified [69].The computation flow chart illustrating how the adopted Simo-Riflex-DMS simulation tool works on this coupled model in relation to other simulation codes used as input it, is as shown in **Figure 5.1**.

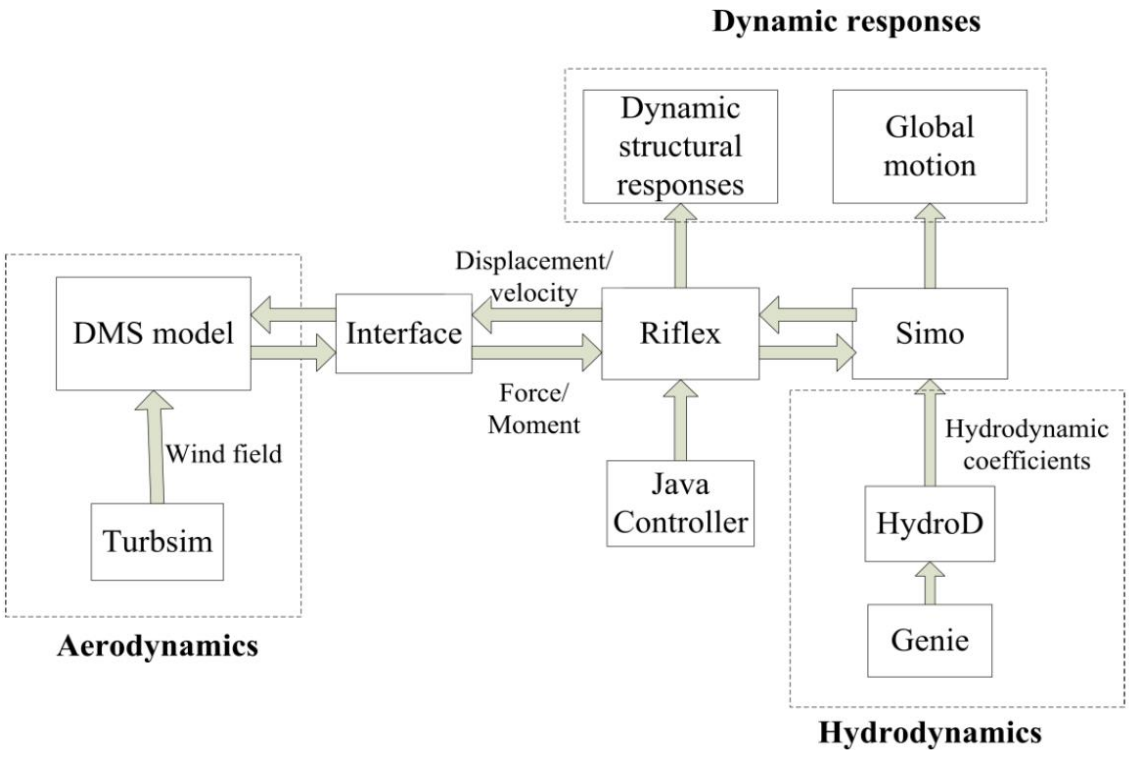

Figure 5.1: Computation flow chart for the coupled model[71]

5.1.5. Stochastic Modelling of the Environmental condition

It is of importance to select realistic environmental conditions for proper evaluation of offshore wind turbines. Therefore, a combined wind and wave environmental conditions is considered for the FVAWT modelling. Furthermore, other special conditions such as current, tidal conditions and ice could be significant at some offshore location like in the artic region. However, such conditions are considered out-of- scope for this thesis. Additionally, the stochastic nature of loading and response for the FVAWT is assumed due to the inherent randomness of wind and wave conditions.

Although, the wind speed varies with longitudinally, laterally and vertically, the longitudinal component is considered dominant and hence it forms the basis for the wind direction at which the mean wind speed is described for periods 10 minutes or 1 hour. Furthermore, the mean lateral and vertical wind speed are assumed to be zero in the thesis. The instantaneous wind speed at certain direction and a particular point in space is the combination of the mean wind speed and the fluctuating or turbulent component. The fluctuating wind component is represented by turbulent intensity as described in (2.2). In this thesis, the normal turbulence model (NTM) according to the IEC standard is used. The NREL's TurbSim code [81] is used to generate a 3D turbulent wind fields based on the Kaimal turbulence model for IEC Class C. Furthermore, the variation of the mean wind speed with altitude called the wind shear due to viscous boundary layer effects generates a wind profile. This wind profile is modelled by the power law described in (2.1), it estimates the mean wind speed at any height above the mean sea level for the normal wind profile model (NWP) proposed in IEC standard.

A real sea state can be represented by non-linear stochastic wave models. The wave time series are produced using inverse fast Fourier transformation (IFFT) with the assumption that the surface elevation of an offshore site is a Gaussian process. Therefore, for the assumed narrow-banded short term sea state, the wave energy can be represented by a wave spectrum, while the wave phase is uniformly distributed within the interval [0 2π]. In this thesis, the JONSWAP (Joint North Sea Wave Project) spectrum [135] in (2.48) is applied for generating the long-crested irregular waves.

To depict a realistic offshore environmental condition, a combination of wind-wave environmental state is considered. Hence, the relationship between the wind and waves can be

expressed by a joint distribution of the 1-hour mean wind speed at 10 m above sea water level, the significant wave height (*Hs*) and the spectral peak period (*Tp*). Johannessen et al. [152] proposed a joint probability density distribution with respect to the wind and wave measurements from 1973-1999. The joint distribution represented in (5.5) is a product of the marginal wind distribution f_{U10} (w), the conditional distribution of Hs given U10, and the conditional distribution of Tp given Hs and U10.

$$f_{U_{10}H_S T_P}(u,h,t) = f_{U_{10}}(w) f_{H_S/U_{10}}(h/S) f_{T_P/H_S U_{10}}(f/h,u) \tag{5.5}$$

A contour surface can be generated using (3.5), it ensures the various weather parameters with a certain return period can be jointly modelled. The conditional average values of Hs and Tp for a given U_{10} corresponding to wind speeds U_w (Cut-in to cut-out rotor wind speed) at hub height is calculated by applying the joint distribution function. Therefore, a set of load cases for the normal operating condition as in **Table 5.1** has been selected for simulating the FVAWT response with respect to the estimated correlated wave and wind conditions at the Statfjord site in the North Sea. The wind and wave direction is in alignment. These Design Load Cases (DLC) are used for both the Baseline 5 MW FVAWT and the Optimised 5 MW FVAWT dynamic analysis.

Table 5.1: Combined wind and wave environment for normal operating condition

DLC	Uw (m/s)	HS (m)	TP (s)	TurSim Model
1	5	2.10	9.74	NTM
2	10	2.88	9.98	NTM
3	14	3.62	10.29	NTM
4	18	4.44	10.66	NTM
5	22	5.32	11.06	NTM
6	25	6.02	11.38	NTM

5.2. Response to stochastic loads

In short term sea states, wind and wave conditions can be assumed stationary, hence response can be described as a linear superposition of individual frequency components. The variance

spectrum is a convenient approach of defining the frequency component of a process X which is expressed by the Fourier transform in (5.6) of the correlation function [147].

$$S_X(\omega) = \frac{1}{2\pi} \int_{-\infty}^{\infty} C_X(\tau) e^{-i\omega t} \, d\tau \tag{5.6}$$

The linear correlation between the response spectrum S_F (ω) and a process (wind speed or wave surface elevation) spectrum S_X (ω) can be expressed for the wind- or wave load through a complex transfer function (H_{XF}), as shown in (5.7).

$$S_F(\omega) = \left|H_{XF}(\omega)\right|^2 S_X(\omega) \tag{5.7}$$

where, S_F (ω) represents the one-degree response spectrum.

5.3. Fatigue Analysis

Fracture in structural elements due to Fatigue damage are created by cyclic stress variations. Cyclic stress variation can cause fatigue damage even though the stress level is below the yield stress of the material it microscopic imperfections are created which leads to high local stress concentration and gradual crack growth. From fracture mechanics perspective, imperfections and microscopic cracks growth are dominant weak points like in welds and bolted points. The cracks grow, reducing the effective area of the cross-section required to resist the loadings, hence fracture occurs when the remaining cross section area does not have enough capacity, and the global system or the point fractures.

A fatigue process are categorized as high cycle or low cycle fatigue. High cycle fatigue are fatigue process with more than 10^4 load fluctuations during the lifetime, but has a lower stress level, whereas low cycle fatigue has a lower number of cycles, but has high stresses level which can cause deformation into the plastic range [153]. In this work, elastic material behaviour is considered, hence any stress level above the yield stress is defined as structural failure. Furthermore, the number of cycles during the life of a floating wind turbine is high, hence only high cycle fatigue is considered.

The long term load distributions and a material response model is the basis for fatigue damage and life time estimation. The Paris' law or an S-N curve approach can be employed for the

material response model. The S-N curve approached explained in the subsequent section is applied in this work.

5.3.1. The S-N Curves Approach

In S-N curves approach, it is assumed that cracks growth due to high cycle fatigue in structures is purely due to the stress variation and that the mean of the varying stress is insignificant. The method is based on laboratory tests, where specimens are subjected to stress ranges of varying amplitude (S) until it reaches failure. The number of cycles until failure (N) assumed a linear relationship (with slope m) with the logarithm of the stress amplitude (S) as in (5.8) according to Wöhler approach [154].

$$N = KS^{-m} \tag{5.8}$$

The expression in (5.8) is generally referred to as an S-N curve. S-N curves for offshore welded steel structures can be found in [154]. For corrosion protected structural parts in air, a higher number of stress cycles with small amplitudes can be permitted, and the S to log(N) can be described with a bi-linear curve, as depicted in **Figure 5.2**.

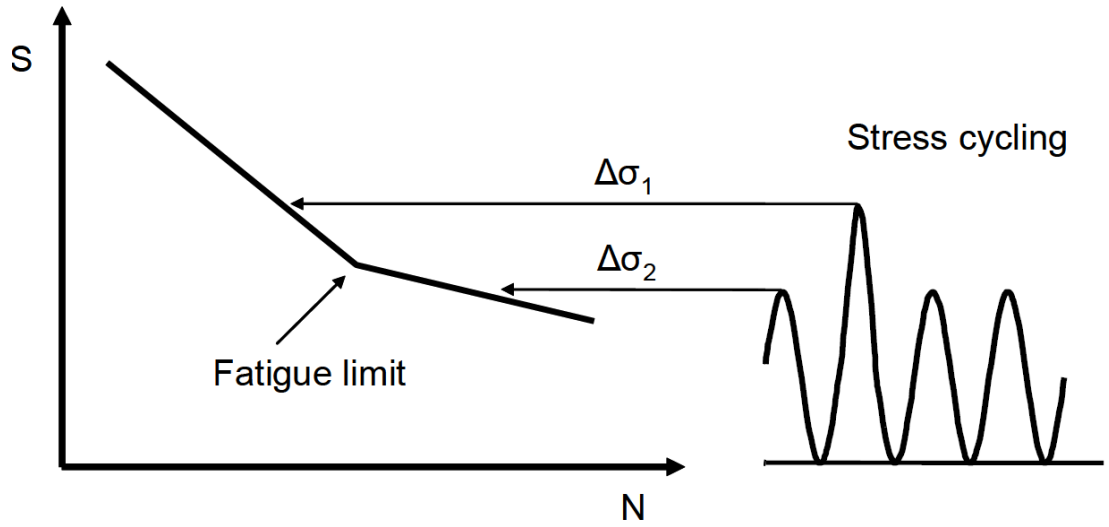

Figure 5.2: Bi-linear S-N-curve with an illustration of cyclic stress [154].

There are different ways of numerating stress concentrations in a full fatigue analysis. Local analyses are to determine hot spot stress directly or Stress Concentration Factors (SCF) can be applied to the nominal stress. The SCFs is most suitable for simple joints, and can involve various SCFs for different stress components. Fredheim [155] in 2012, carried out studies for local hot spot stress analysis for a semi-submersible wind turbine. However, in this work, the system components are not considered as welded, hence no evaluation of hot-spot stress is carried out.

The Miner- Palmgren hypothesis in (5.9) assumed the individual stress fluctuation contribution is an accumulated partial damage. Therefore, the Miner- Palmgren hypothesis can be applied to determining the fatigue damage for a long term stress range distribution.

The accumulated damage is found by adding the contributions from each stress level.

$$D = \sum_{j}^{N_{bins}} \frac{n_j}{N_j} \tag{5.9}$$

where n_j is the number of stress cycles in the time history and N_j is the number of cycles to failure according to the S-N curve. D = 1 indicates a failure.

5.3.2. Cycle counting algorithms

The nominal stress histories of structural elements can be obtained from results of frequency domain analysis, or time domain FE analyses from the FEM solver.

In order to estimate fatigue damage from stress histories by applying S-N curves, number of stress cycles must be known and stress levels must be performed. Various methodology for stress cycle counting can be employed: Range counting, peak-valley counting or level crossing method and the Rainflow counting method. The Rainflow counting method is proved to give the best estimate for fatigue analyses for wide banded stress histories [156].

Frequency domain methods for fatigue estimation assumed the stress amplitudes are related to the load spectrum. The frequency domain methods are fast, but do not provide less accurate when compared with Rainflow counting technique unless a frequency domain solution for the stress is available [148]. Therefore, the Rainflow counting algorithm will be used in this thesis.

5.4. Post-Processing Tools

The results of the time simulation demand several post-processing analysis in order to evaluate relationships or correlations between parameters of interest. The correlation between parameters of interest are performed through statistically and spectral analysis while fatigue damage and life-time estimation is carried out using the fatigue analysis method discussed in the previous section. The post-processing flow chart for the simulation results are as represented in **Figure 3.3.** The MATLAB programme is used to perform the statistical analysis as well as serving as a master application for the NREL MLife Toolbox and Wafo Toolbox.

NREL MLife is a MatLab-based tool used to analyse results from wind turbine tests and dynamic simulations. The response results from Riflex is used as input to the NREL Mlife Toolbox [72] through MATLAB in order to estimate short-term fatigue damage on turbine structural element. The algorithm are based on the fatigue life estimation discussed in section 5.3.

In this thesis, the Wafo Toolbox [157] is used for the spectral analysis of results of structural responses from Riflex and global motion from SIMO. The time series of structural response and global motion from Riflex and SIMO are respectively loaded into MATLAB in order to perform spectral analysis using Wafo.

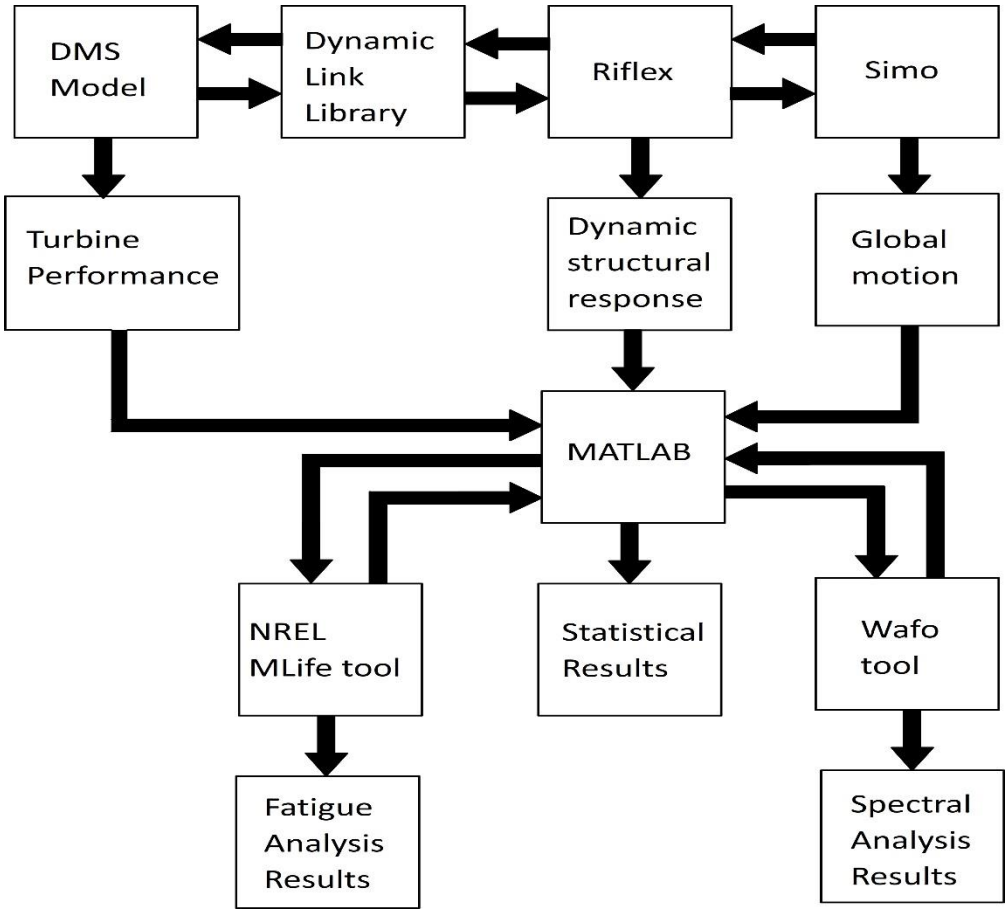

Figure 5.3: Post-processing flow chart

6 Dynamic Response Analysis of Floating Vertical Axis Wind Turbine

6.1. General

The fully coupled time domain simulation tool is used to study the dynamic response of both the Baseline 5 MW FVAWT and the Optimised 5 MW FVAWT under various environmental conditions. The fully coupled nonlinear time domain simulation tool, Simo-Riflex-DMS developed by Wang [69] and described in section 4.1.4 was adopted in this thesis. The dynamic response of the FVAWTs include global motions of the platform, structural responses of the rotors, and mooring lines dynamics. The analysis for the FVAWT is focused on the effect of turbulence on the respective FVAWT dynamic responses under normal operating conditions. Furthermore, the dynamic responses of the Baseline 5 MW FVAWT is compared with that of the Optimised 5 MW FVAWT.

6.2. Dynamic Response Analysis of the 5 MW baseline FVAWT

6.2.1. Validation of Response Results

The Baseline 5 MW FVAWT was modelled exactly as it was described by Wang [71]. The analysis of the FVAWT's global motion has been carried out by Wang and will not be repeated in this thesis, hence focus will shift to ensuring the correctness of the model in this thesis by comparing the turbine performance in terms of power generated to that presented by Wang in his PhD thesis.

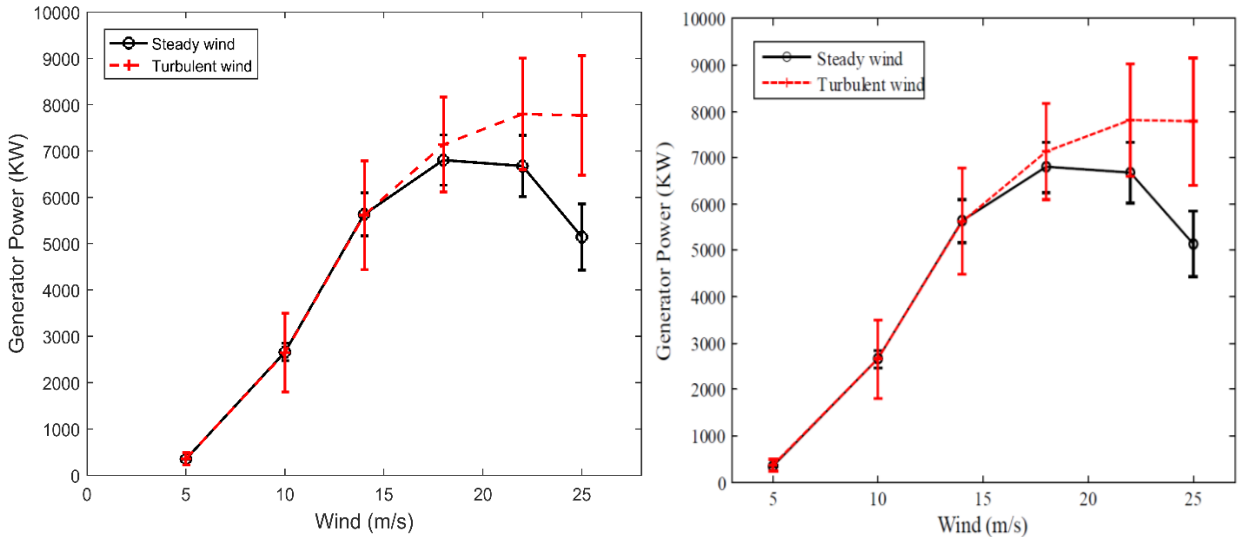

(a)Results of this thesis simulations. **(b)** From PhD presentation by Wang [71].

Figure 6.1: Power generated under steady and turbulent wind conditions.

The power curve in **Figure 6.1** (a) from this work showed the same performance as that presented by Wang in **Figure 6.1** (b) both for steady and turbulent wind condition. Hence, the model proved to be correctly modelled and further analysis can be performed as discussed in the subsequent sections.

6.2.2. Effect of Turbulence on FVAWT Performance

I. Effect of Turbulence on Transmitted Torque

Under wave and wind conditions, the aerodynamic loads changes continuously as the azimuthal blade position changes. This creates varying loads and excitation of loads on the rotor. However, the variation in aerodynamic load can be amplified, introducing extra excitation under turbulent wind. Therefore, it is pertinent to study the dynamic behaviour of the FVAWT under steady wind and turbulent wind conditions. The design load conditions are combined state of irregular waves in alignment with wind as summarized in **Table 5.1**. Furthermore, the same control model is used for both steady and turbulent wind conditions.

At a particular mean wind speed, corresponding time series of wave elevations is generated for steady wind and the turbulent wind conditions. Furthermore, the wind turbulence is stochastic in nature, hence a number of random realisations called, 'Seeds' were generated to conservatively consider the inherent randomness in the turbulent wind components. Therefore,

time domain simulations of a total of 5 seeds were carried out for each of the 6 different environmental conditions.

The effect of turbulence on the torque transmitted by the rotor to the generator is presented in **Figure 6.2**. The plot of the transmitted torque at each wind speed is based on the mean value of simulated power for each 3600 s simulation after removing start-up transient for five different seeds. The error bars are used to indicate the standard deviation from the mean values in this thesis. The plot showed that above the rated wind speed of 14 m/s, the difference between the transmitted torque under steady and turbulent wind condition widens as the wind speed increases with the transmitted torque under turbulent condition having the largest value at wind speeds above the rated speed. The mean torque transmitted at the rated wind speed exceeds the rated torque of 9.078MN because the BL dynamic stall model is included in this model. This further showed the significant of the dynamic stall model in the design of the DeepWind rotor.

Additionally, as the wind speed increases above the rated speed 14 m/s, the deviation from the mean transmitted torque under turbulent wind conditions increases higher than that of the steady wind conditions. Hence, at the cut-out wind speed, the turbine experienced the highest deviation from the mean transmitted torque under turbulent wind condition. This is also accompanied by maximum turbulence effect on the mean transmitted torque as the observed difference between the mean value under turbulence and steady wind condition is largest at this wind speed.

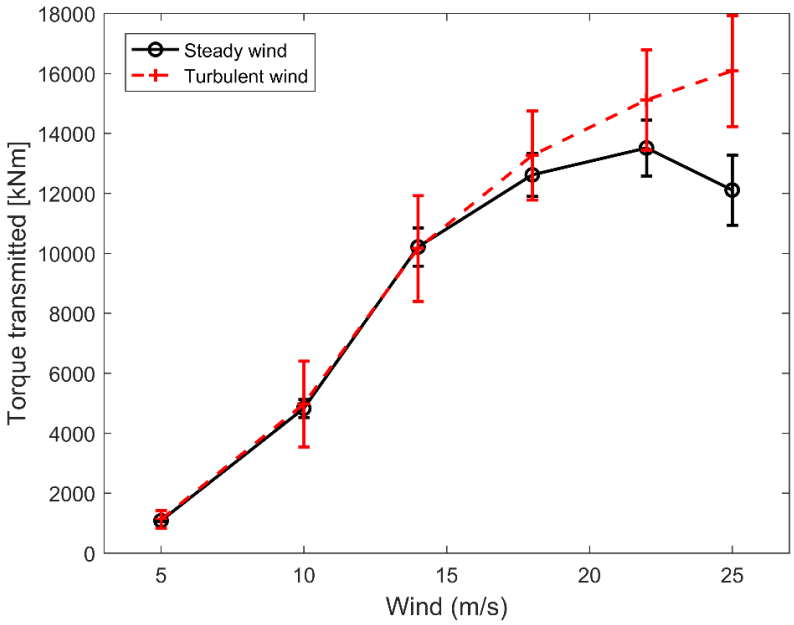

Figure 6.2: Transmitted torque under steady and turbulent wind conditions.

6.2.3. Effect of Turbulence on Structural Dynamic Response of the FVAWT

I. Effect of turbulence on the Turbine Blade Bending Moment

In evaluating the distribution of bending moments along the blade, 20 points shown in **Table 6.1** were selected, spanning from the bottom to the top root nodes of the blade. The plot of the distribution of bending moments along the blade is as shown in **Figure 6.3.**

Table 6.1: Description of nodal points selected for blade bending moment evaluation

Nodal points	Coordinates (Y,Z)	Length segment (m)	Description
1	(0.10,15.074)	0	Blade root (bottom)
2	(12.35, 23.28)	11.61	Along blade
3	(22.14, 29.87)	23.43	Along blade
4	(31.13, 36.28)	34.80	Along blade
5	(39.59, 42.90)	54.94	Along blade
6	(46.70, 49.11)	55.75	Along blade
7	(52.87, 55.52)	64.97	Along blade
8	(57.84, 62.10)	73.39	Along blade
9	(62.00, 70.52)	81.55	Along blade
10	(63.61, 80.79)	93.90	Along blade
11	(62.80, 87.35)	99.50	Blade center
12	(59.18, 96.09)	108.58	Along blade
13	(54.35, 102.47)	117.22	Along blade
14	(48.44, 109.19)	125.86	Along blade
15	(41.06, 115.90)	135.34	Along blade
16	(33.01, 122.44)	145.53	Along blade
17	(24.02, 128.81)	156.45	Along blade
18	(14.49, 135.34)	167.79	Along blade
19	(4.70, 141.38)	179.73	Along blade
20	(0.00, 144.56)	188.17	Blade root (top)

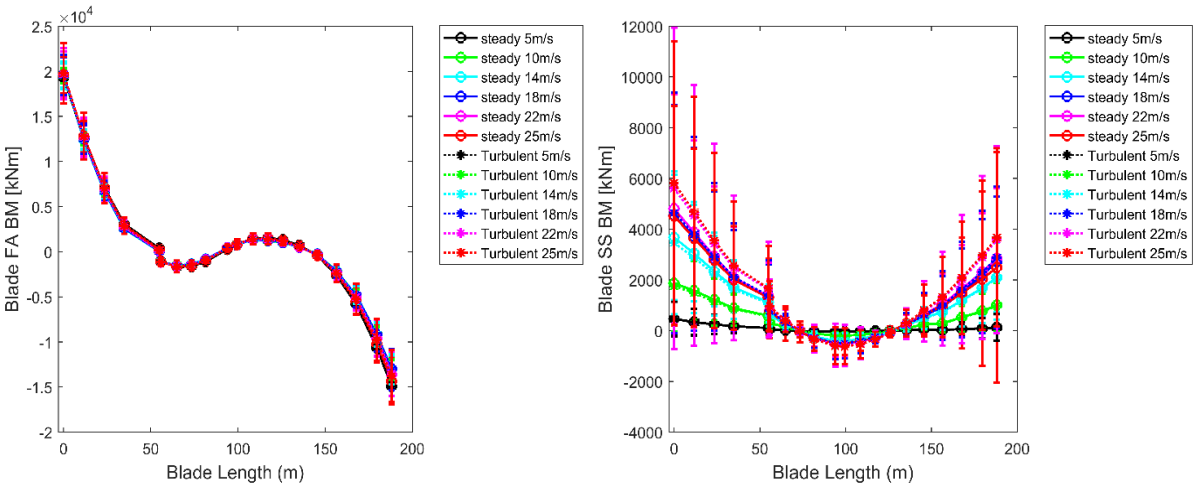

Figure 6.3: Blade FA and SS bending moment distribution

Figure 6.3 showed the turbulent effects is minimal for the FA bending moment as compared with the SS bending moment. Furthermore, the variation in terms of standard deviation from the mean bending moment for both FA and SS bending moment is negligible at locations closer to the center of the blade but increases as both extremes of the blade are approached. Moreover, both plots showed the blade experienced higher bending at its extremes, including a slight increase at the center for the FA bending moment. However, SS bending moment under both turbulent and steady wind condition approached zero at the center unlike the FA bending moment.

The mean SS bending moment distribution at each wind speed under turbulent wind condition appears to be close to the values under steady wind. However, the plot showed the critical points are at the blade extremes. This is further investigated in the next section.

II. Effect of turbulence on Selected Critical Points on the Wind Turbine

The distribution of bending moments along the blade presented in **Figure 6.3** showed that the bending moments are more significant at the blade roots or extremes and at the centre. Therefore, these points of higher bending moments were selected for further analysis as described in the subsequent sections. Furthermore, the tower base is a point of high bending moments, hence, the tower base is as well selected for analysis.

i. Tower Base

The bending moment at the tower base is investigated and a plot of the bending moments against the mean wind speeds are shown in **Figure 6.4**. **Figure 6.4** showed that at the tower base, the mean FA bending moment increases while the mean SS bending moment decreases as the wind speed increases. The plot also revealed that as the wind speed increases, the effect of turbulence on the mean FA and the mean SS bending moments at the tower base remained relatively low but became significant at wind speeds above 18m/s with a larger bending moment under turbulent wind condition. Furthermore, the effect of turbulence on the mean values increases as wind speed increases. The effect of turbulence had its largest effects at 25m/s wind speed.

The excitation created by turbulence in terms of load variation analyzed as standard deviation from the mean values of the respective bending moments is depicted in **Figure 6.4**. The plot

showed the effect of turbulence on load variability is negligible up to 22m/s wind speed for both the FA and the SS bending moments. Furthermore, the effect of turbulence only resulted in an increased load variation above the 22m/s wind speed for both the FA and the SS bending moments.

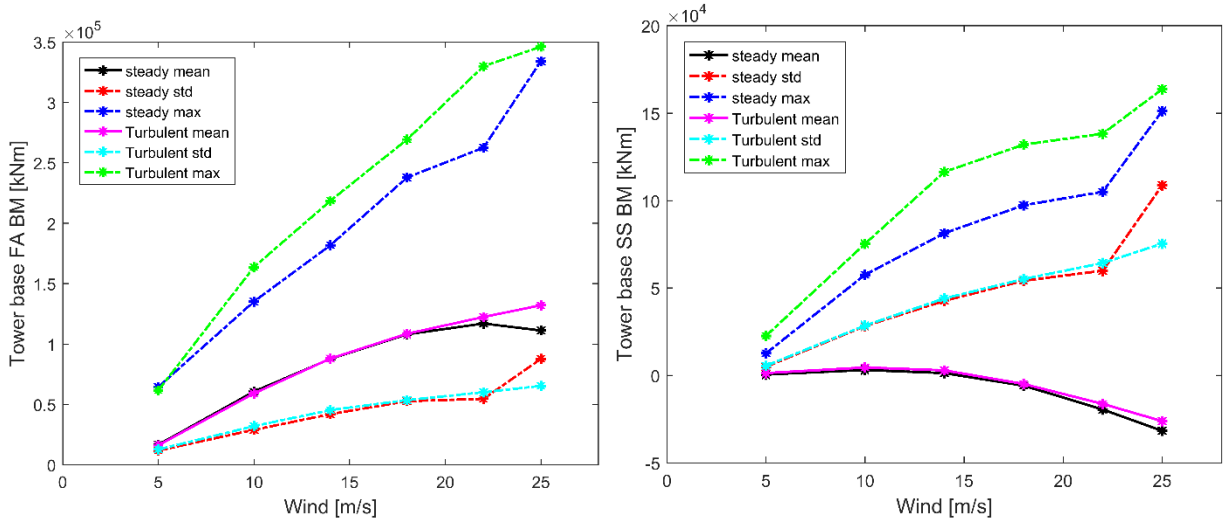

Figure 6.4: Tower Base FA and SS bending moments.

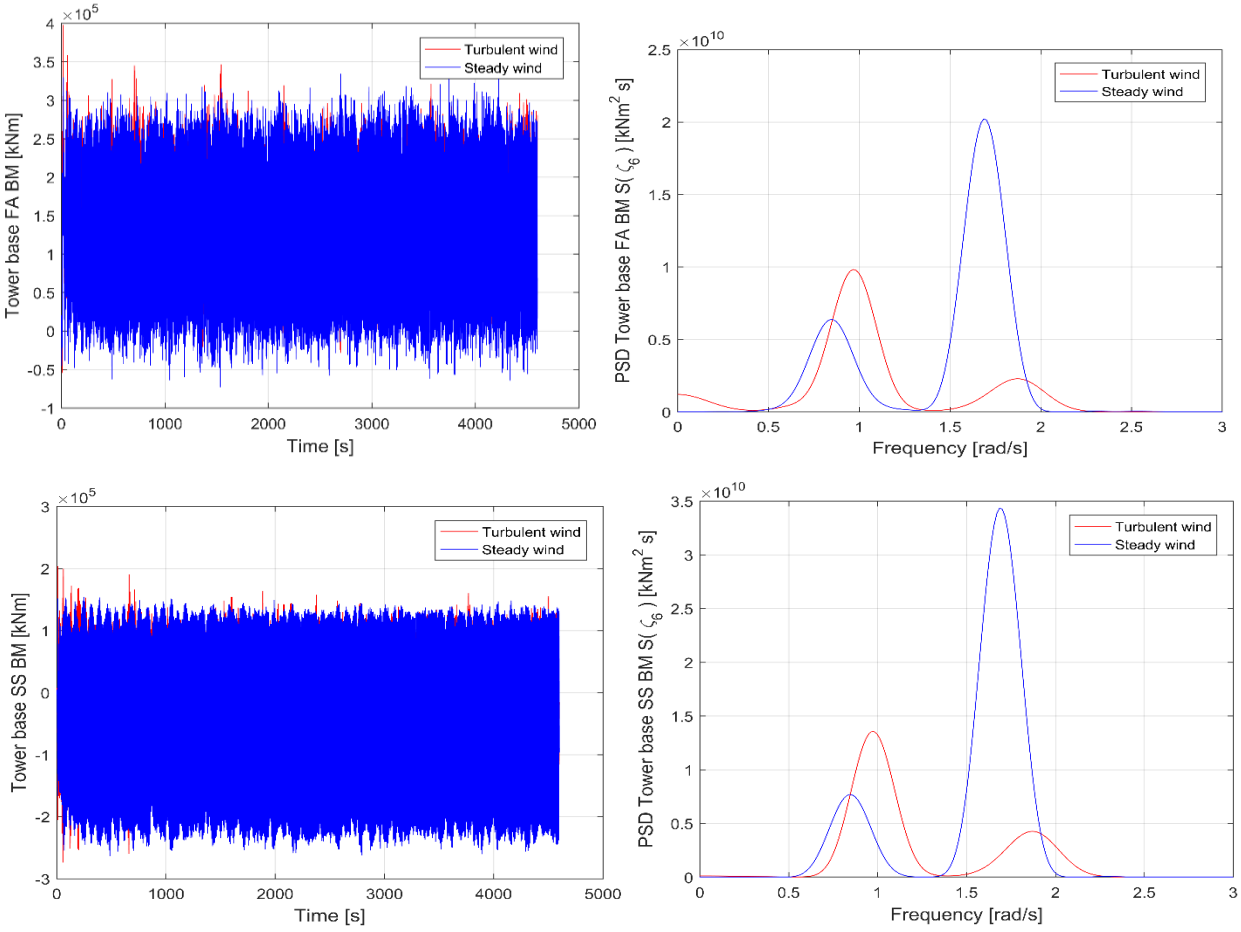

Figure 6.5: Tower Base FA and SS bending moment's time series and PSD for DLC6.

Another approach to investigate the effect of turbulence on the loads at the tower base is to study the Bending Moment (BM) time history and spectral plots. The environmental condition DLC 6 (V = 25 m/s, Hs = 6.02 m and Tp = 12.38 s) was chosen for this study because the statistical analysis of the BMs in **Figure 6.4** showed the turbulent effects was largest at 25m/s wind speed. The Bending Moment (BM) time history and the power spectra plots for DLC6 are shown in **Figure 6.5**. The effect of turbulence is depicted in the plots of the BM time history for both FA and SS by slightly higher spikes or BM amplitudes under turbulent wind condition. The spikes or BM amplitudes are indication of deviation from the mean values under the respective wind conditions.

This turbulent effect is further elaborated in the spectral plots for both FA and SS BMs. The wave frequency excitation dominates the response under turbulent wind condition while the 2P frequency excitation proved dominant under the steady wind condition as shown in the spectral plots.

The spectral plot for the FA BM revealed the wave excitation under turbulent wind condition indicated by the first peak (red) is about 80% higher than under steady wind condition (blue). Similarly, the spectral plot for SS BM showed similar response as that of the FA BM.

The lower second peak (red) due to turbulent wind condition at the 2P frequency (at high wind speeds, the turbine experiences a shift from the original 2P frequency of 1.1 rad/s) on the spectral plot indicated that the effect turbulence resulted in a lower excitation at the 2P frequency. This effect is more than 300% and 600% reduction in excitation when compared with the response under steady wind condition at the 2P frequency for the FA and the SS BMs respectively.

ii. Blade Root at Top and Bottom

Figure 6.6 and Figure 6.7 showed the bending moment at the last and first nodal point along the blade, called the blade root (top) and blade root (bottom) respectively with coordinates as described in **Table 6.1**.

In **Figure 6.6** and **Figure 6.7**, the mean BMs increases as the wind speed increases except for the FA BM at the blade root (top) which remained constant between the 10 – 18 m/s wind speed but decreases afterwards. Also, the variation in the mean BM values increases as wind speed increases for the FA and the SS BMs at the both blade extremes under both wind conditions.

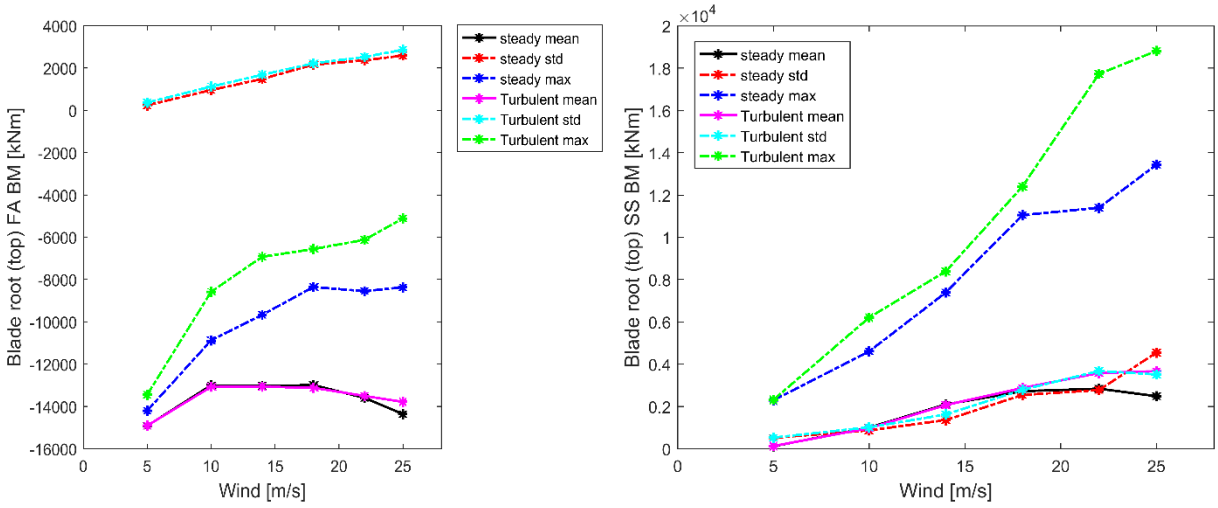

Figure 6.6: Blade root (top) FA and SS bending moments

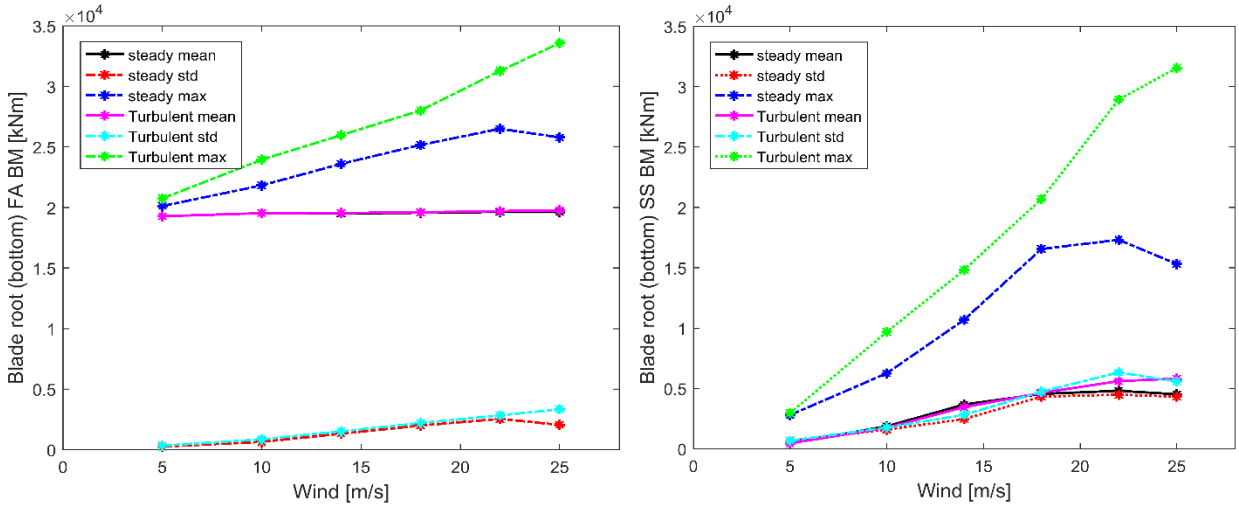

Figure 6.7: Blade root (bottom) FA and SS bending moments

The excitation due to turbulence on the FA and the SS BMs at the blade root (top) and the blade root (bottom) is remains negligible up to 22m/s wind speed. However, above 22 m/s wind speed, the turbulent effects become more noticeable with the mean SS bending moment increasing tremendously as seen in the maximum value under turbulent wind condition. The largest effect of turbulence on the mean values were experienced at 25 m/s wind speed fro both FA and SS BMs.

The difference between the standard deviation under turbulent wind condition and the standard deviation under steady wind condition increases at each higher wind speeds. This implied that the effect of turbelence on load variation increases as wind speed increases.

iii. Blade Center

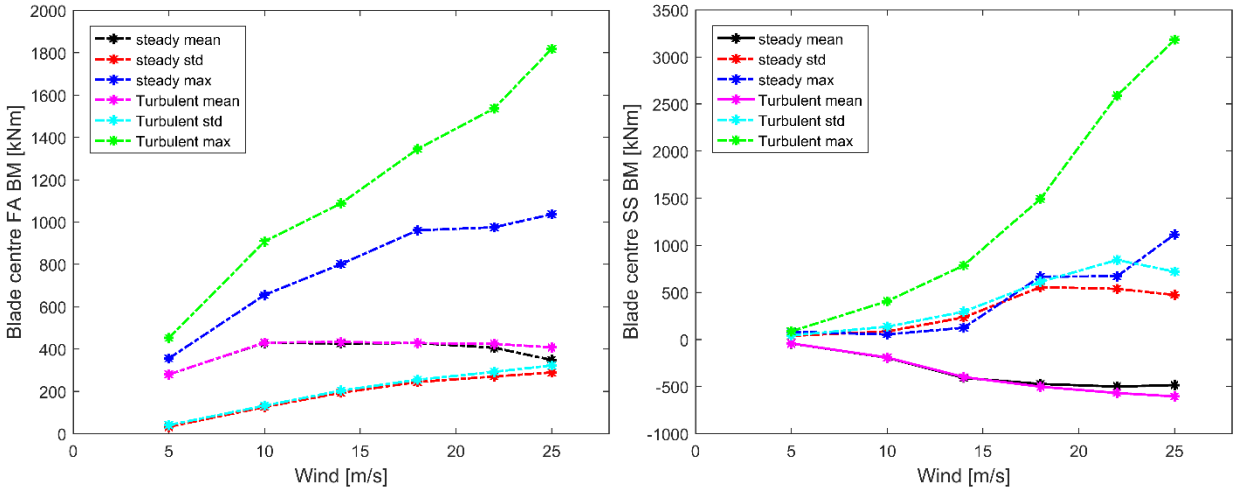

Figure 6.8: Blade center FA and SS bending moments

Figure 6.8 presents plots of the FA and the SS bending moments at the centre of the blade. The effect of turbulenece on the mean values is siginificant above 18m/s wind speed with higher values under turbulent wind condition for both the FA and the SS bending moments . Also, the turbulence effect resulted in increasing load variability as wind speed increases above 18m/s with a maximum effect at 25m/s wind speed.

III. Effect of turbulence on Mooring Lines Tension

The mooring lines tension is plotted against the mean wind speeds as shown in **Figure 6.9**.

Generally, the mean tension in mooring line 2 increases as the wind speed increases except at 25 m/s wind speed where it decreased under steady wind condition unlike in mooring line 1 and 3. This is because the mooring line 2 is positioned in the negative x-axis (see **Figure 4.1)** in alignment with the wave and wind, hence as the wind speed increases, the platform drift faster towards the positive x-axis. As the platform continues to drift, mooring line 2 will be continuously stretched while mooring line 1 & 3 are continuously relaxed simultaneously. This results in increasing tension of mooring line 2 and decreasing tension in mooring line 1 and 3. However, a moment is reached when mooring and loads are transferred to mooring line 3 because it is now stretched while mooring line 1 is continuously relaxed. This phenomenon is believed to have been initiated at 18 m/s wind speed under steady wind condition and it continued up to 25m/s wind speed as shown in **Figure 6.9**. The phenomenon could be attributed to the platform drift at

wind speeds above the 18 m/s to the positive y-axis as indicated by increased tension of mooring line 3 at wind speeds above the 18m/s wind speed.

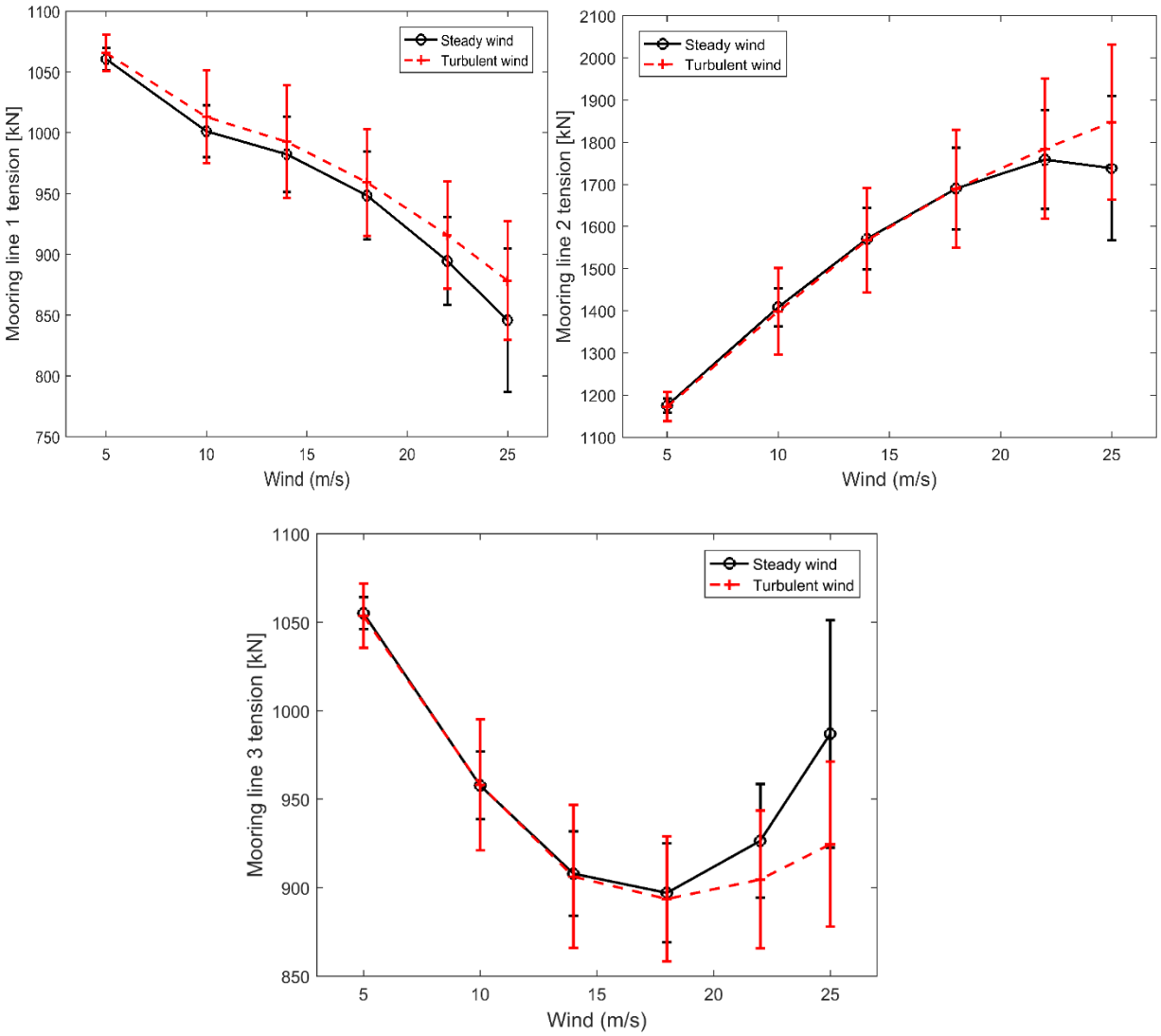

Figure 6.9: Mooring lines tension.

However, this effect is cushioned by unsteady platform drift within the identified wind speed region as observed in lower mean tension of mooring line 3 under turbulent wind condition.

The effect of turbulence is as well obvious in the increasing disparities between the load variability under turbulent wind condition and under steady wind condition as the wind speed increases for all mooring lines except for mooring line 3 whose response characteristic is unlike the others. The load varies higher from the mean values under turbulent wind condition than under steady wind condition at all wind speeds for mooring line 1 and 2.

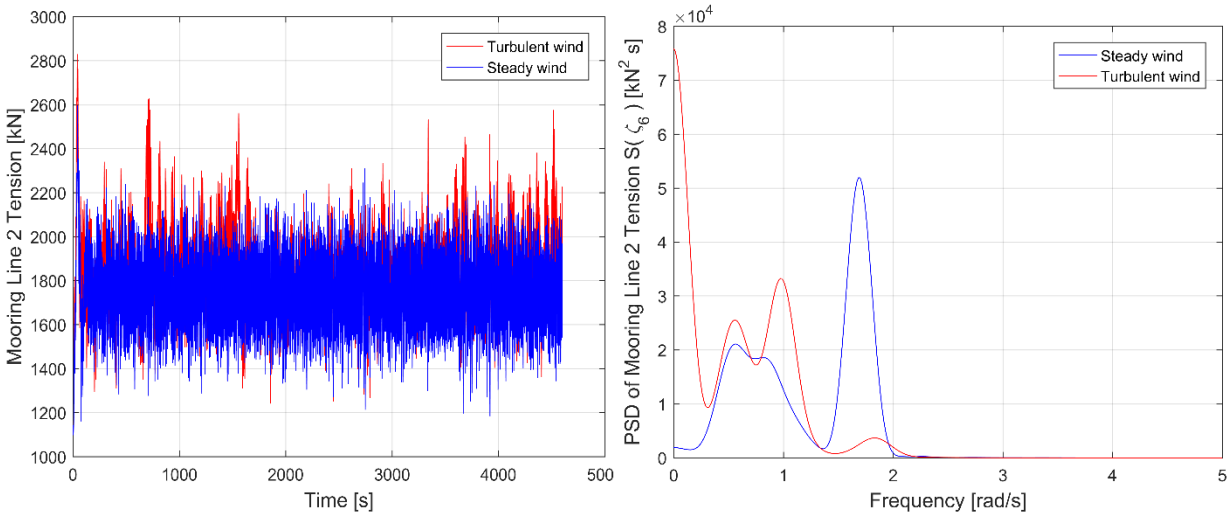

Figure 6.10: Mooring lines tension 2 time series and PSD for DLC6.

The time series plot of **Figure 6.10** showed the turbulent effects is high at DLC6 load condition for both mean values and varations from the mean. Furthermore, the spectral plot is observed to have higher peaks under turbulent wind condition at the wave excitation frequency than under steady wind condition.

The last peaks were observed at higher frequencies (about 1.7 rad/s), which should be induced by the eigen frequency of the blade showed about 500% reduction on the excitement under turbulent wind condition. This means the mooring lines 2 experienced reduced load excitation under turbulent wind at this frequency.

6.3. Dynamic response analysis of the 5 MW Optimized FVAWT

6.3.1. Model Validation

The model verification is demonstrated through comparing the performance of this model to that of the 5 MW Baseline FVAWT. The 5 MW Baseline FVAWT has already been verified by model-to-model comparison [43].Hence, it is sufficient to use the 5 MW Baseline FVAWT to validate the results of the 5 MW Optimised FVAWT by comparing the performance of both model. Furthermore, both models are similar in terms of power capacity, moorings configuration and support structure, hence a similar response exhibited by the 5 MW Baseline FVAWT is expected for the 5 MW Optimised FVAWT. Moreover, for a good model-to-model comparison, the same environmental condition as described in **Table 5.1** was adopted for the simulation of both FVAWTs model. The 5 MW Optimised FVAWT is verified by comparing the performance of

both FVAWTs model in terms of power generation. The wind turbine generator control is the same as used for the 5 MW Baseline FVAWT.

The power generated under turbulent wind condition from the coupled time-domain aero-hydro-servo-elastic simulation for both FVAWTs are compared as shown in **Figure 6.11**.

In **Figure 6.11**, the variability in power generated is indicated by error bars, representing the standard deviation from the mean power generated. The power generated from the 5 MW Optimised FVAWT is well in agreement with that of the 5 MW Baseline FVAWT up to the rated wind speed of 14 m/s. Furthermore, the mean power produced at the rated wind speed for both FVAWTs are almost the same value. Moreover, the mean power produced at the rated wind speed exceeds the rated power of 5 MW because of the application of the BL dynamic stall model in the 5 MW Optimised FVAWT. This consequently demonstrate the importance of the dynamic stall model in the design of the optimised rotor.

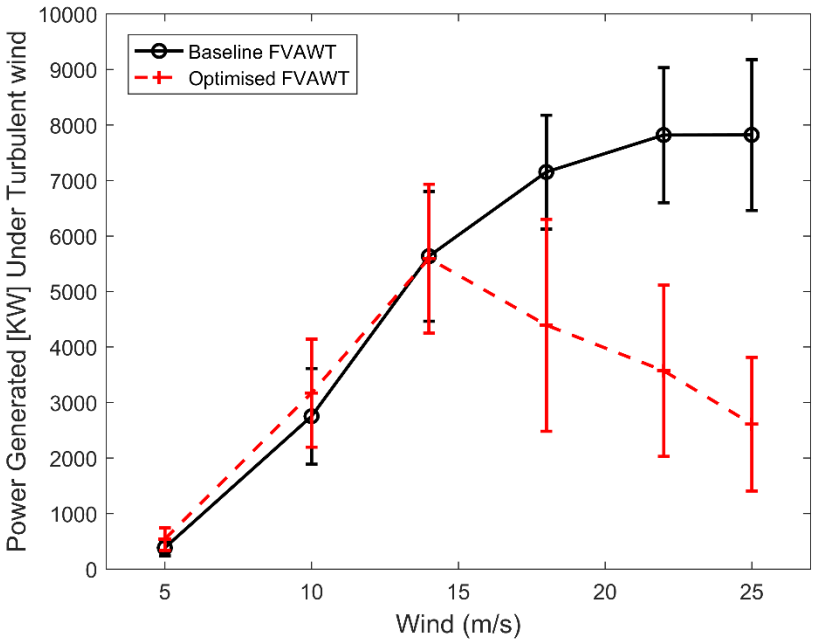

Figure 6.11: Comparing both FVAWT power generations.

The produced power from the 5 MW Optimised FVAWT is expected to be increasing with increasing wind speeds. However, the power produced by the 5 MW Optimised FVAWT deviated tremendously from the power produced by the 5 MW Baseline FVAWT at wind speeds exceeding the rated wind speed. This could be attributed to the adoption of the same generator control for the 5 MW Optimised FVAWT. The 5 MW Optimised FVAWT could produce the rated or above the rated 5 MW power at the rated rotational speed of 5.73 RPM which is higher than 5.26 RPM of the 5 MW Baseline FVAWT. Therefore, using the same control will produce the results shown in

Figure 6.11. It has been acknowledged that a unique control should be developed for the 5 MW Optimised FVAWT but this was considered out of scope in this work. Moreover, the agreement between both results up to the rated speed is sufficient to prove that the 5 MW Optimised FVAWT is capable of producing 5 MW at the 14 m/s rated wind speed and 5.73 RPM rated rotational speed.

6.3.2. Effect of Turbulence on FVAWT Dynamic Response

I. Effect of Turbulence on Power Generation

In **Figure 6.12,** the generator power produced by the FVAWT under steady wind is compared with that obtained under turbulent wind conditions.

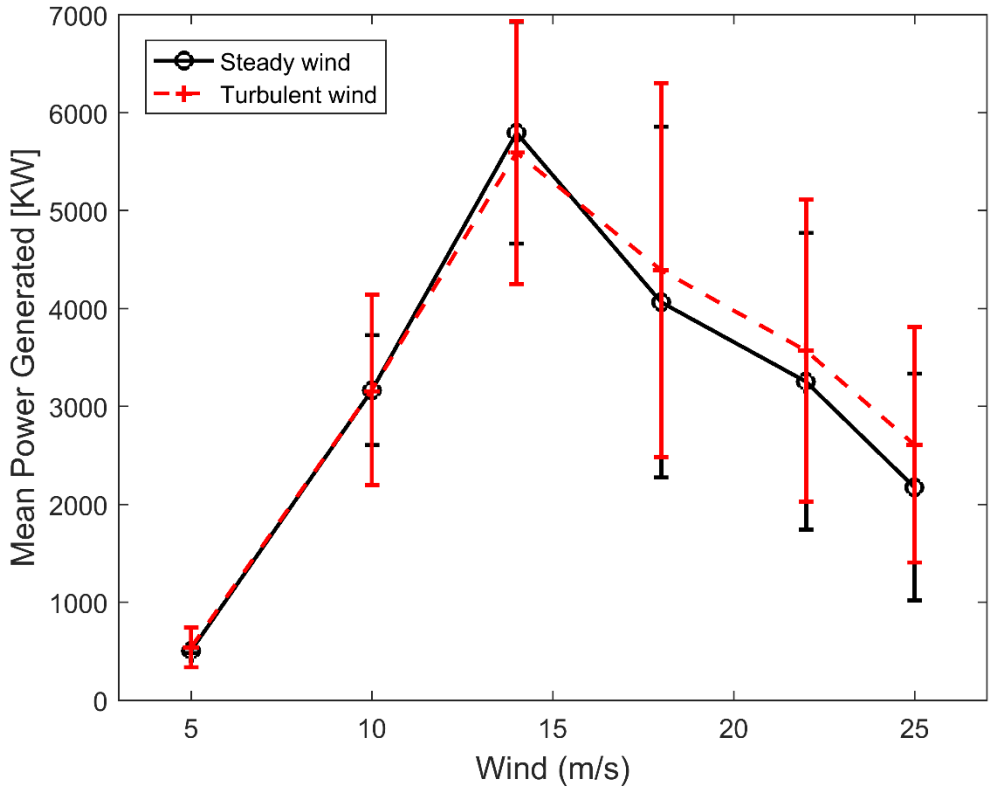

Figure 6.12: Power generated under steady and turbulent wind conditions.

The plot is based on the averaged value of the simulated power for each 3600s simulation after the start-up transient for five different seeds is removed. The error bars show the standard deviation from the averaged values. Although the same environmental condition is used for steady and turbulent wind conditions, the averaged power is found to differ above the rated wind speed of 14 m/s, and the disparity widens as the wind speed increases. The power produced under turbulent wind condition is higher than under steady wind condition for wind speeds above the rated speed. Furthermore, the error bars are longer under turbulent wind condition

as the wind speed increases. This indicates that the variation in the mean power produced under steady wind condition is lesser than the variation from the mean power produced under turbulent wind condition.

II. Effect of Turbulence on Global Motion

The effect of turbulence on the FVAWT global motion is investigated based on the statistical analysis and the spectral analysis of simulation results, including the inspection of the plots of time series of motions for the 6 degree of freedom motion. For the analysis of global motion in 6 degree of freedom motion, two environmental conditions were selected;

- Environmental condition at the rated wind speed of 14 m/s DLC 3 (V = 14 m/s, Hs = 3.62 m and Tp = 10.29 s).
- Environmental condition at the cut-out wind speed of 25 m/s DLC 6 (V = 25 m/s, Hs = 6.02 m and Tp = 12.38 s).

In statistical analysis, the averaged value and standard deviation from all 6 DLC are analysed. In the subsequent subsections, the time series and power spectrum for surge, sway, heave, roll, pitch and yaw motions are analysed under both steady and turbulent wind conditions for DLC 3 and DLC 6 as shown in their respective subsections. In the plot for time history of motions, it was observed that the amplitude of motions are clearly higher under turbulent wind condition than under steady wind condition for both design load cases (DLC) in all 6 degree of freedom motion.

The power spectrum of motions in the individual degree of freedom motion for the two wind conditions can be compared with further evaluate the effect of turbulence. From the power spectra plots, the natural responses for all degree of freedom motion experienced greater excitation under turbulent wind condition. Furthermore, peaks are observed at the 2P frequency (a characteristics of VAWTs with two blades) for both steady and turbulent wind conditions. In VAWTs, the axis of rotor rotation is not in line to the wind direction, and the angle of attack varies with the azimuthal position of the blades during operation. This creates variation in aerodynamic loads within a cycle of rotation. If the VAWT has two blades, each blade cuts in the wind direction once in every cycle. Therefore, a two bladed VAWT will cut-in twice in every cycle of the rotor, this causes a variation in the torque twice in every cycle. The 2P effect creates the 2P frequency. When the wind turbine rotates at the rated rotational speed of 0.62 rad/s, the 2P frequency is approximately 1.24 rad/s. The 2P effect is prominent in the roll and the pitch motions. The discussions on the statistical results and the 2P effects is under the section for the pitch motion.

i. Surge Motion

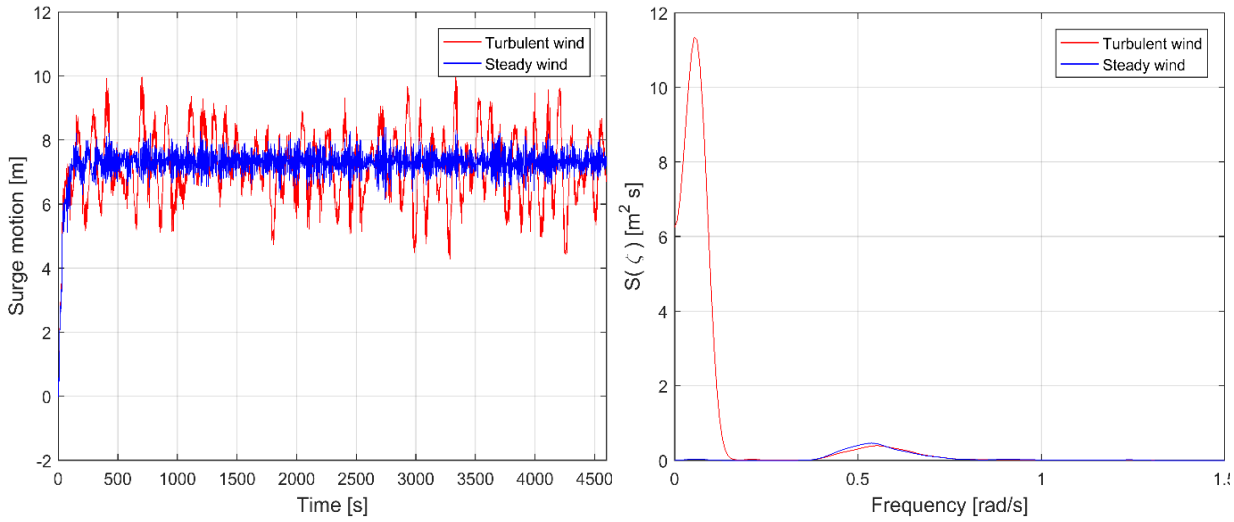

Figure 6.13: Time series and power spectrum of surge motion for DLC 3.

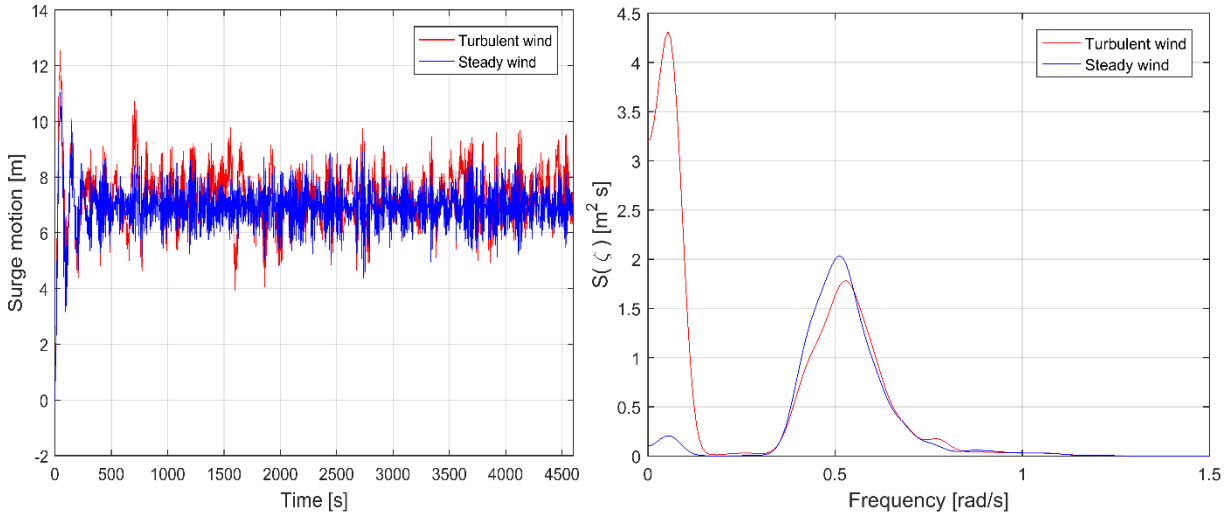

Figure 6.14: Time series and power spectrum of surge motion for DLC 6.

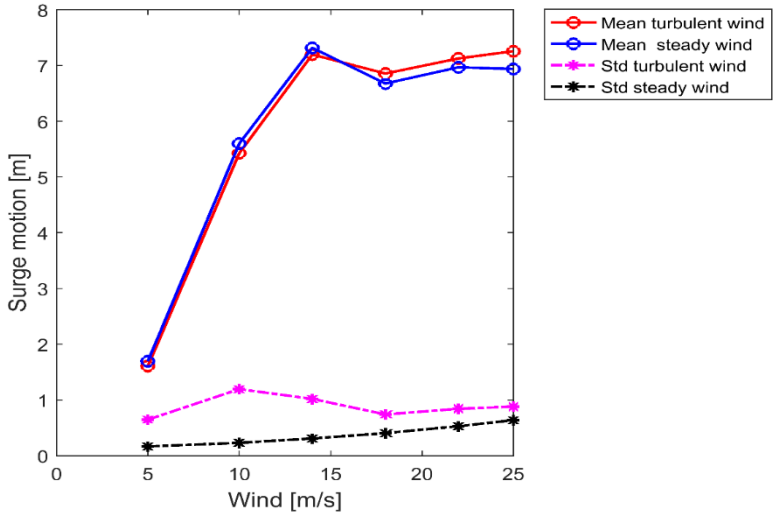

Figure 6.15: Surge motion for all DLC

ii. Sway Motion

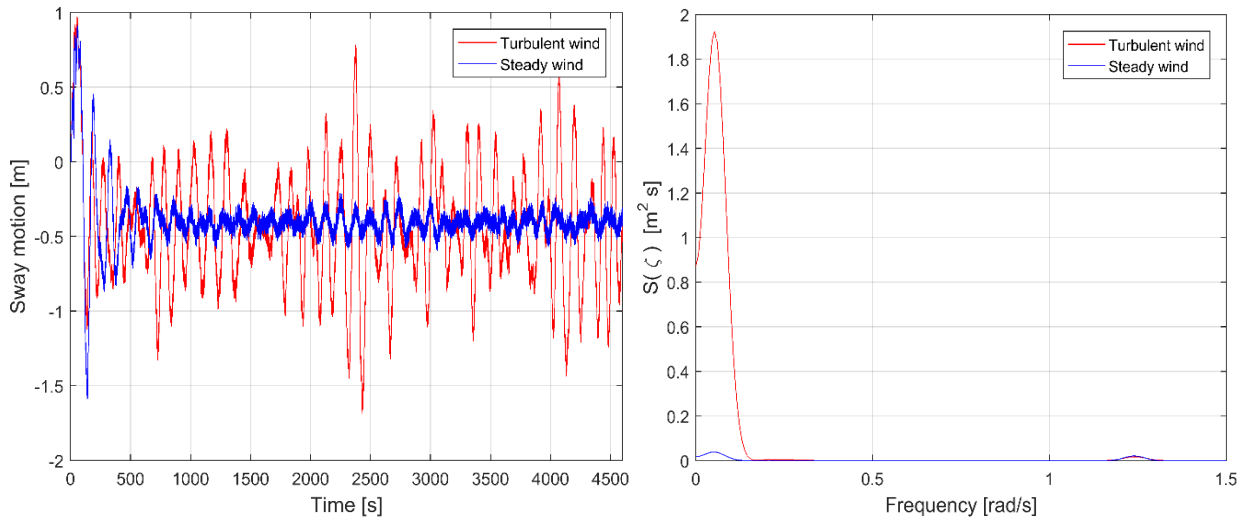

Figure 6.16: Time series and power spectrum of sway motion for DLC 3.

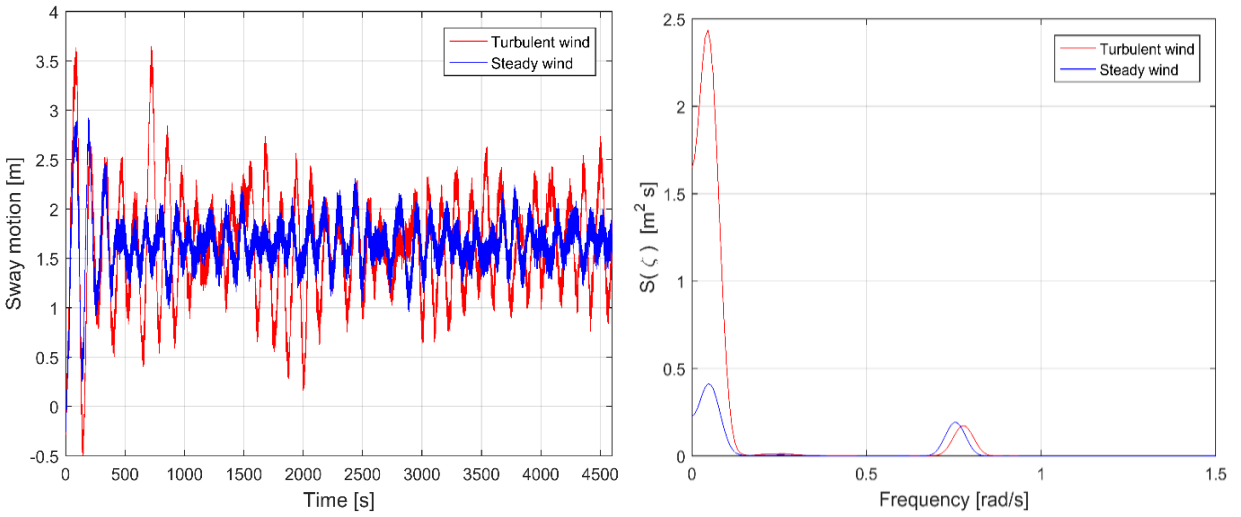

Figure 6.17: Time series and power spectrum of sway motion for DLC 6.

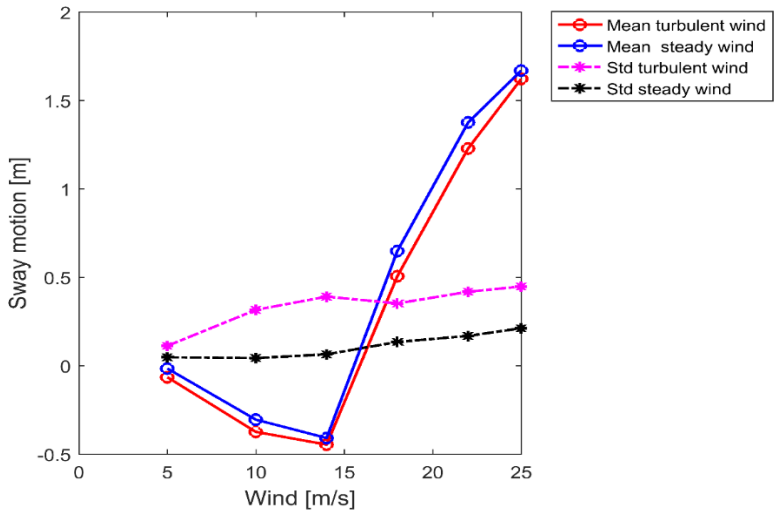

Figure 6.18: Sway motion for all DLC

iii. Heave Motion

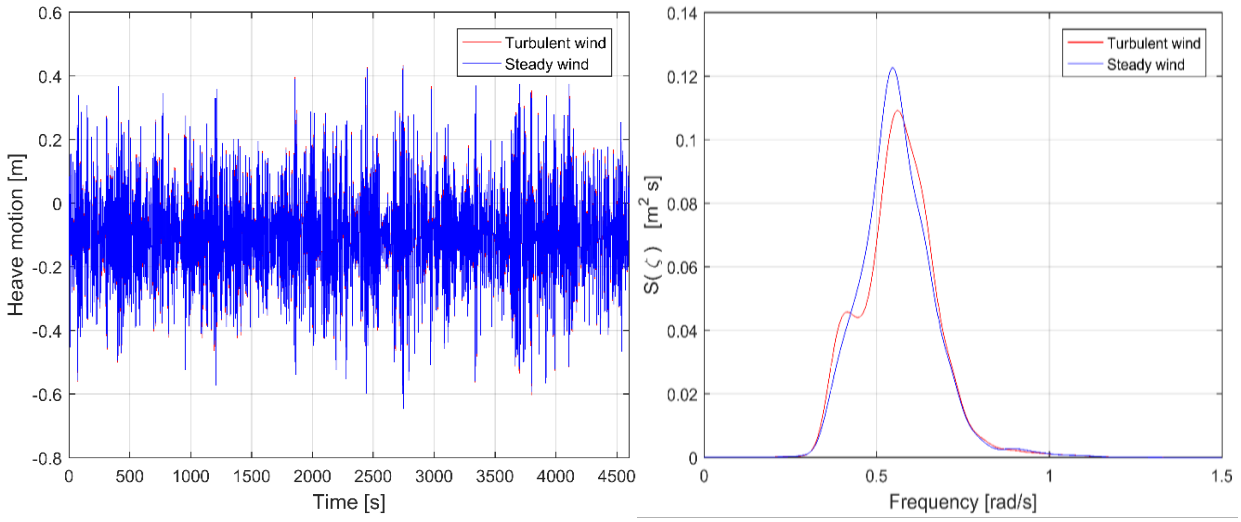

Figure 6.19: Time series and power spectrum of heave motion for DLC 3.

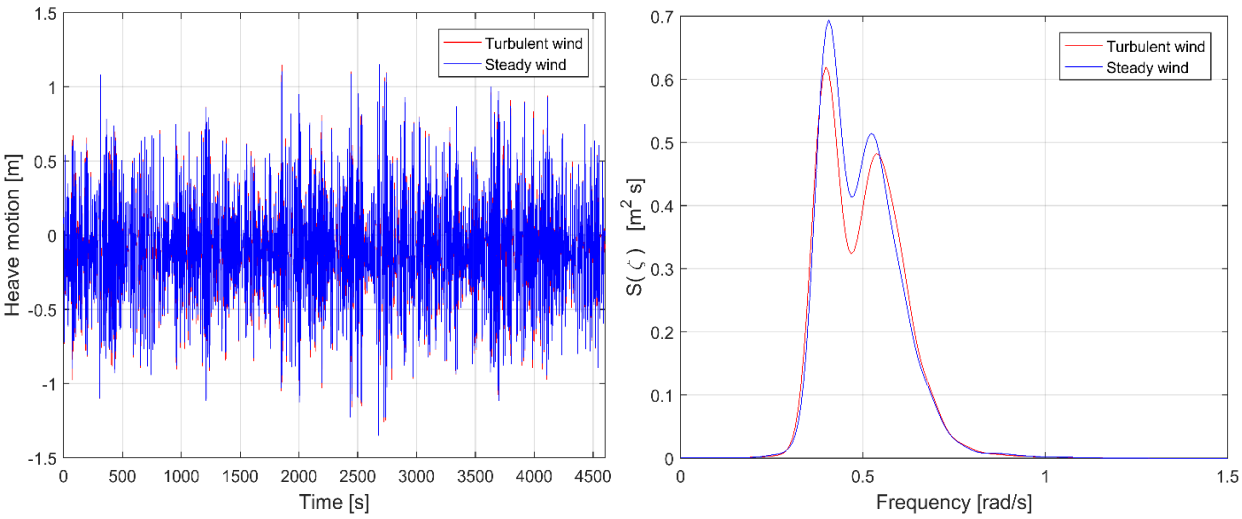

Figure 6.20: Time series and power spectrum of heave motion for DLC 6.

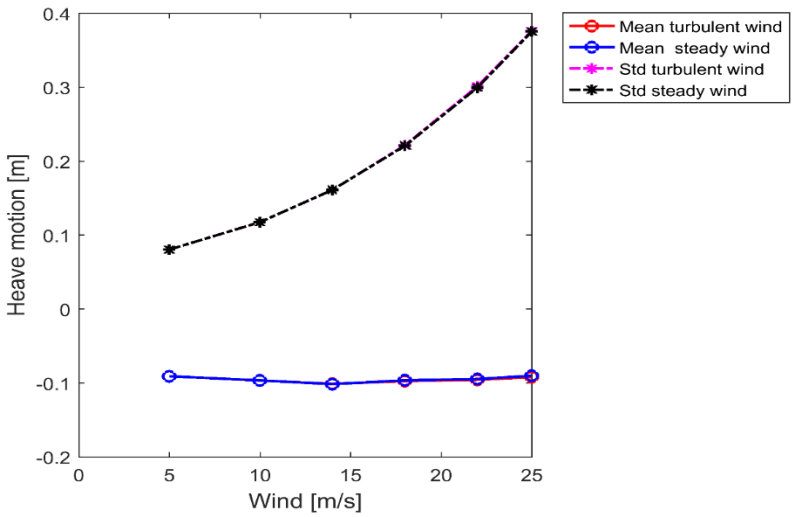

Figure 6.21: Heave motion for all DLC

iv. Roll Motion

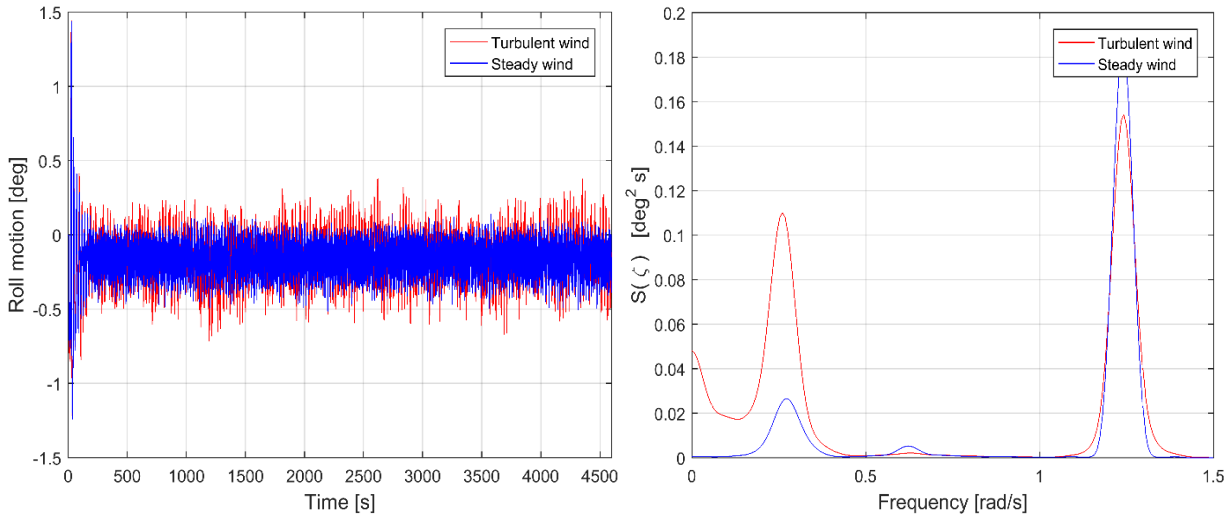

Figure 6.22: Time series and power spectrum of roll motion for DLC 3.

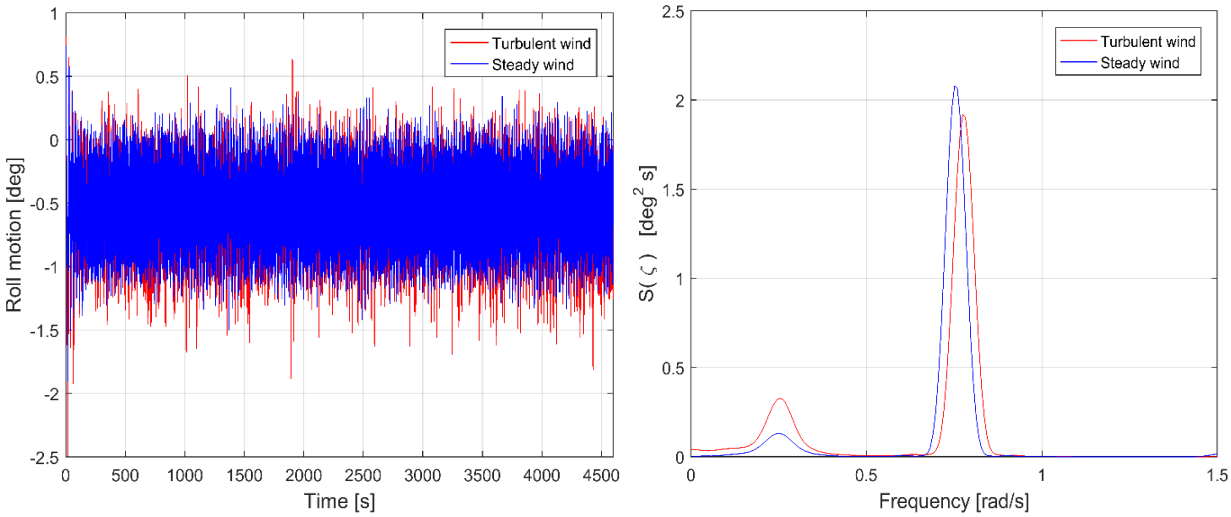

Figure 6.23: Time series and power spectrum of roll motion for DLC 6.

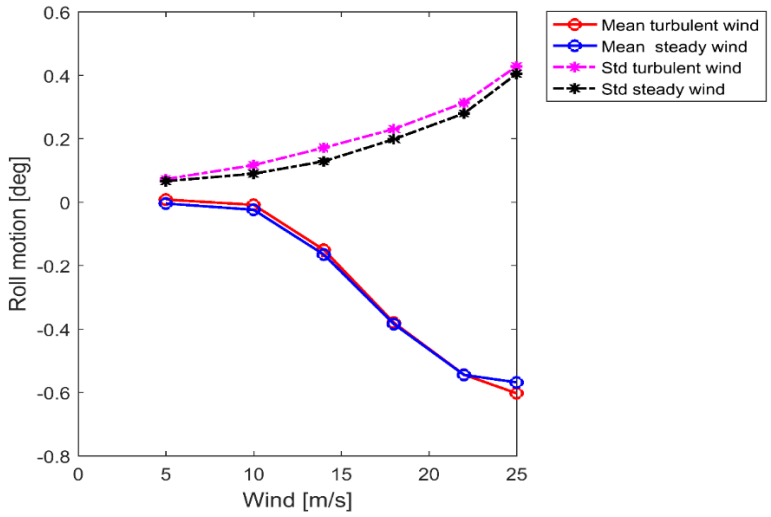

Figure 6.24: Roll motion for all DLC

v. Pitch Motion

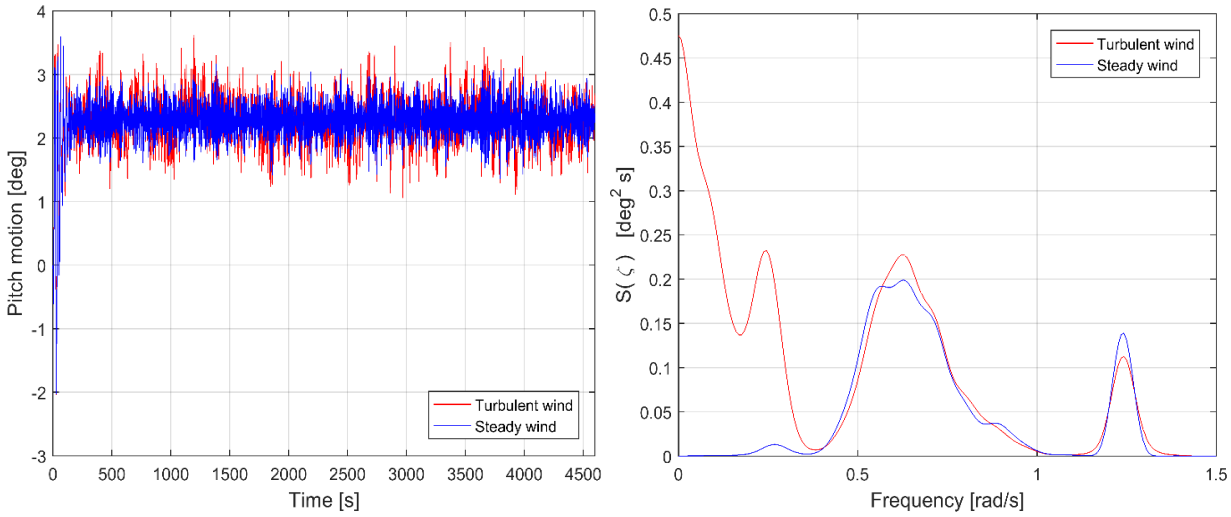

Figure 6.25: Time series and power spectrum of pitch motion for DLC 3.

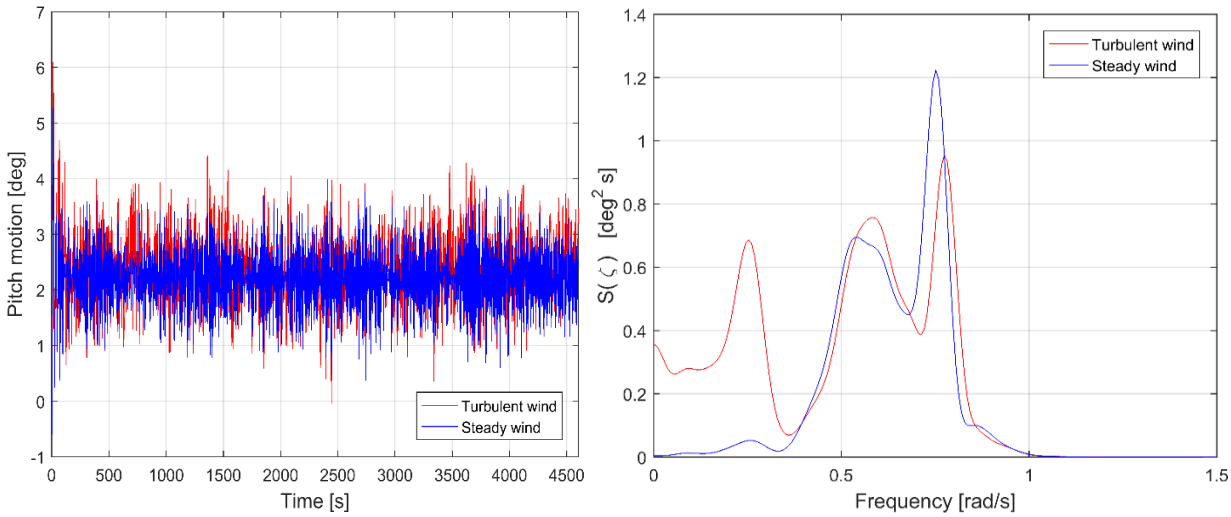

Figure 6.26: Time series and power spectrum of pitch motion for DLC 6.

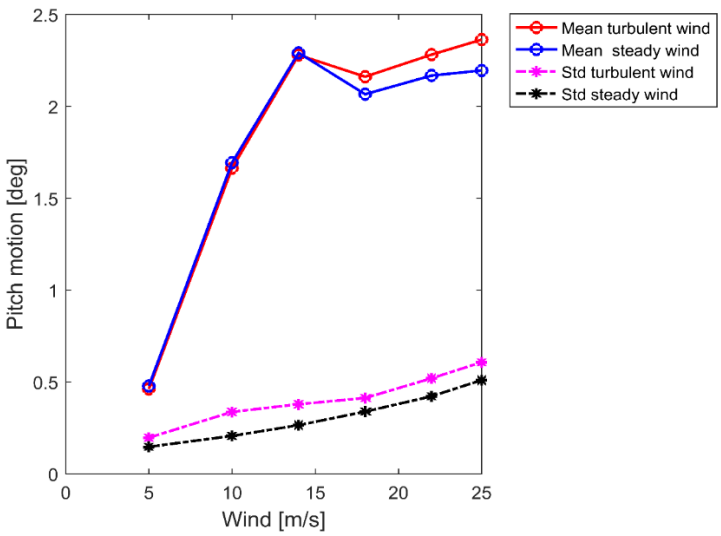

Figure 6.27: Pitch motion for all DLC

The power spectra in **Figure 6.22** and **Figure 6.25** for the roll and the pitch motions respectively revealed the turbulence effect on these motion reduces the 2P effect as seen in the lower peaks at the 2P frequency for turbulent wind condition. Furthermore, as the environmental condition becomes severe in DLC6, the difference in the height of the response peaks at the 2P frequency under steady and turbulent wind conditions become reduced in the roll motion but widens in the pitch motion. Additionally, the 2P frequency is observed to have changed to about 0.55 rad/s for steady wind condition and 0.56 rad/s for turbulent wind condition for DLC6 in both the roll and the pitch motions as shown in **Figure 6.23** and **Figure 6.26** respectively. This is due to the effect of turbulence on the controller as the rotational speeds under steady and turbulent wind conditions now differ.

The results of the statistical analysis of the global motion in terms of the mean value of 5 seeds realisation at each DLC and standard deviation from the mean values are as shown in **Figure 6.15, Figure 6.18, Figure 6.21, Figure 6.24, Figure 6.27, and Figure 6.30** for the surge, the sway, the heave, the roll, the pitch and the yaw motion respectively. The effect of turbulence only resulted in slight difference between the mean values under turbulent wind condition and steady wind conditions. Furthermore, as wind speed increases, this difference widens especially for rotational motions (roll, pitch and yaw), the surge and the sway motions. In general, it can be said that there was only negligible turbulent effect on the mean values especially at wind speeds below the rated wind speed.

The effect of turbulence is more obvious in the variation of motion amplitudes from the mean values as represented by the standard deviation from the mean values. The difference between the standard deviation under turbulent wind condition and steady wind condition narrows as the wind speed increases with the turbulent wind condition having a higher value for all degree of freedom motion except for the heave motion. The wind direction and waves are in alignment along the x-axis, hence, the turbulent wind effects will introduce little or no excitation on the translational motion along the z-axis. This is the reason for the indifference between the variation of motion from the mean values under turbulent and steady wind conditions for the heave motion.

As the wind speed increases, the variation in terms of standard deviation (std) from the mean values is observed to follow a fairly linear behaviour under steady wind condition. However, the standard deviation under turbulent wind condition increases up to the rated wind speed and

then decreases at speeds above the rated wind speed. This showed that under turbulent wind condition, the platform do not experience a steady drift on any direction but rather exhibit a secondary effect. This secondary effect could be a greater interaction among all degree of freedom motion due to the platform stiffness property with the exception of the heave motion.

vi. Yaw Motion

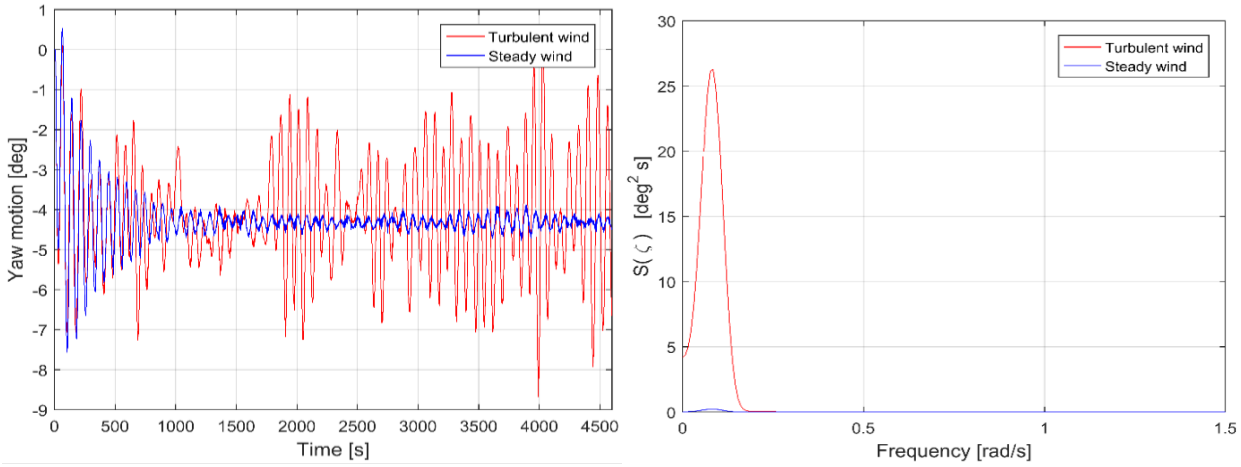

Figure 6.28: Time series and power spectrum of yaw motion for DLC 3.

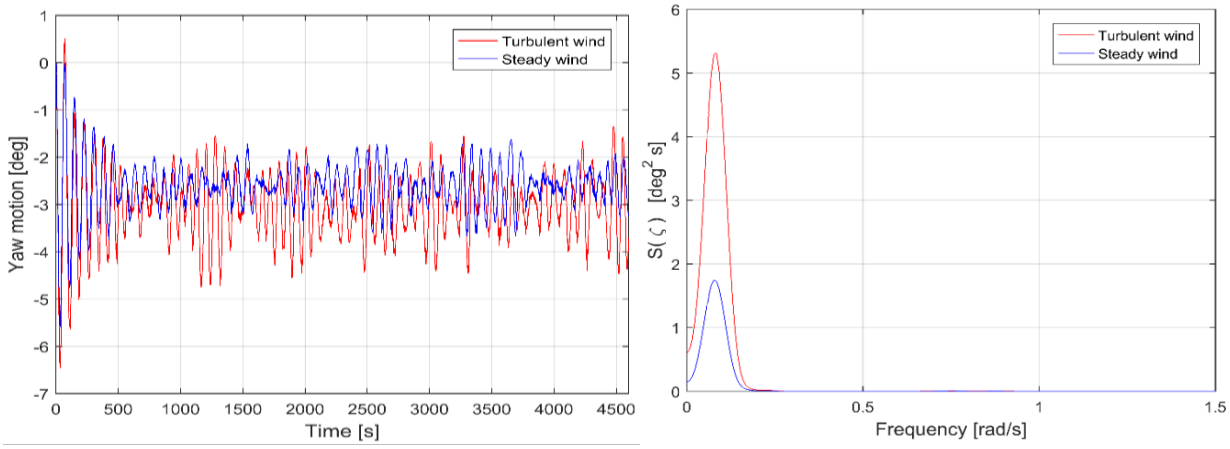

Figure 6.29: Time series and power spectrum of yaw motion for DLC 6.

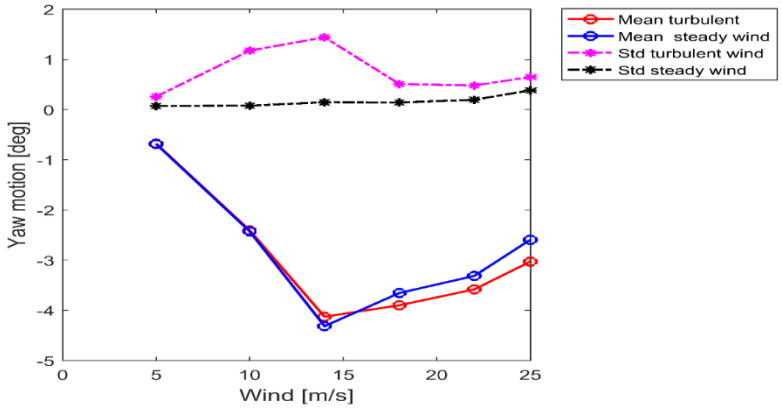

Figure 6.30: Yaw motion for all DLC

6.3.3. Effect of Turbulence on Structural Dynamic Response of the FVAWT

I. Effect of turbulence on the Turbine Blade Bending Moment

To analyze the effect of turbulence on the blade bending moments, 20 points were picked along the blade as described in **Table 6.2.** The distribution of bending moments along the blade are as shown in **Figure 6.31**.

Table 6.2: Description of nodal points selected for blade bending moment evaluation

Nodal points	Coordinates (Y,Z)	Length segment (m)	Description
1	(0.10,15.074)	0	Blade root (bottom)
2	(34.29, 26.44)	29.33	Along blade
3	(45.51, 32.16)	45.42	Along blade
4	(51.63, 39.79)	56.38	Along blade
5	(55.29, 47.41)	64.91	Along blade
6	(58.00, 55.04)	73.09	Along blade
7	(60.12, 62.67)	81.10	Along blade
8	(60.45, 70.30)	88.78	Along blade
9	(59.80, 77.92)	96.43	Along blade
10	(57.35, 87.45)	106.20	Along blade
11	(54.80, 93.17)	112.35	Blade center
12	(49.39, 102.71)	123.18	Along blade
13	(45.71, 108.43)	130.00	Along blade
14	(40.41, 116.05)	139.17	Along blade
15	(34.70, 123.68)	148.49	Along blade
16	(29.16, 131.31)	158.32	Along blade
17	(25.51, 135.12)	163.09	Along blade
18	(14.29, 146.56)	179.16	Along blade
19	(5.51, 154.19)	190.33	Along blade
20	(0.00, 158.00)	200.31	Blade root (top)

The plot of the distribution of FA bending moment along the blade in **Figure 6.31** revealed the turbulence effect caused extra bending moment excitation which increases as the wind speed increases as seen in higher load variability under turbulent wind condition. The mean FA bending moment attained higher values at the blade extremes (roots) and at the blade centre.

The plot of the mean SS bending moment in **Figure 6.31** showed negligible difference between both wind condition but it indicated a higher deviation from the mean value under turbulent wind condition. It was observed that the extreme values were larger than the mean value, hence the mean value appeared to be zero.

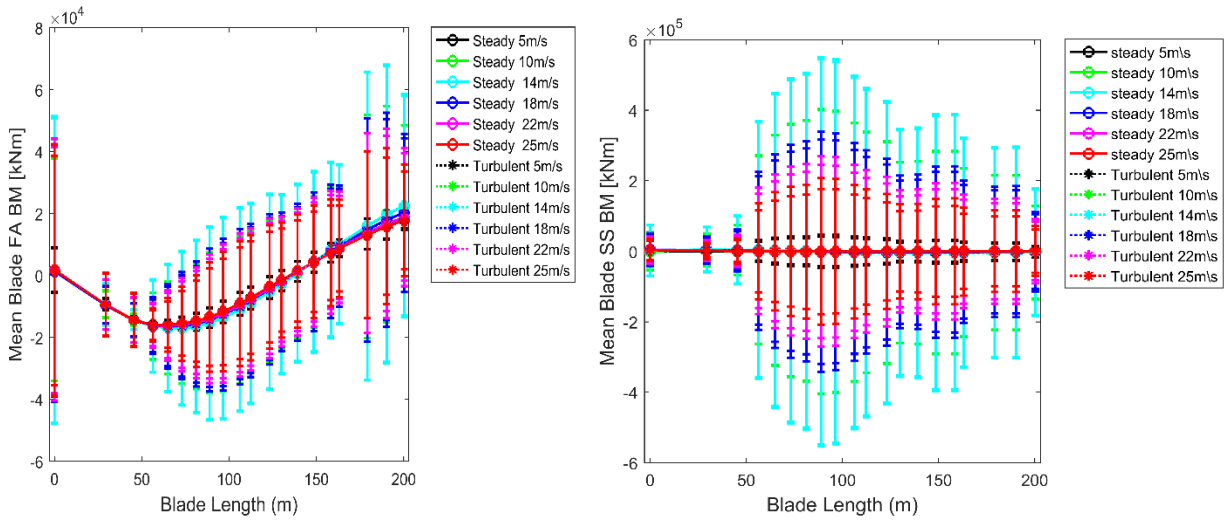

Figure 6.31: Blade FA and SS bending moment distribution for all DLC.

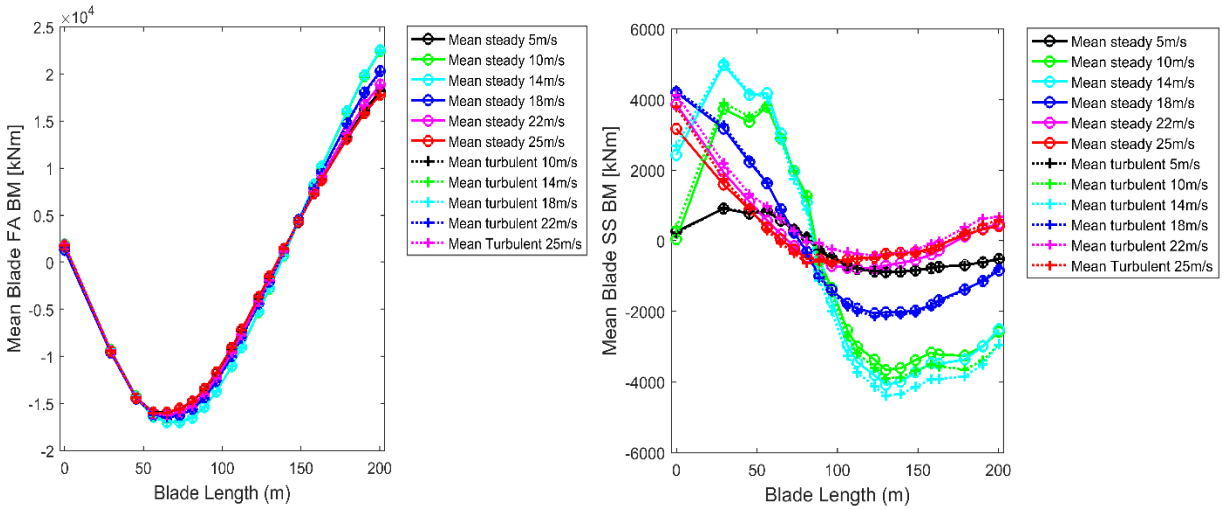

Figure 6.32: Blade mean FA and SS bending moment distribution at all DLC

To analyse this further, an alternative plot of the mean SS and FA bending moment in **Figure 6.32** clearly represents how the mean bending moments are distributed along the blade. It was observed that the mean FA bending moment attained higher values at the blade centre and blade root (top) positions. The plot of the mean SS bending moment in **Figure 6.32** showed higher values at some position slightly away from both blade extremes with highest value near the blade root (bottom) position for wind speeds above the rated wind speed of 14 m/s respectively.

In gerenral, it was clear in **Figure 6.32** that the effect of turbulence on the mean FA and the mean SS bending moments is negligible.

II. Effect of turbulence on Selected Critical Points on the Wind Turbine

The tower base, the blade extremes and the blade center were selected for further analysis because these are positons of high bending as explained in the last section.

i. Tower Base

The results of the statistical analysis of the FA and the SS BMs at the tower base are shown in **Figure 6.33**. The plots show the relationship between the mean values of the FA, the SS bending moments at the tower base with their respective variation from the mean values and the wind speed under both wind condition. The plot showed that as the wind speed increases, the effect of turbulence on the mean values remains insignificant at wind speeds below the rated wind speed for both the FA and the SS BMs.

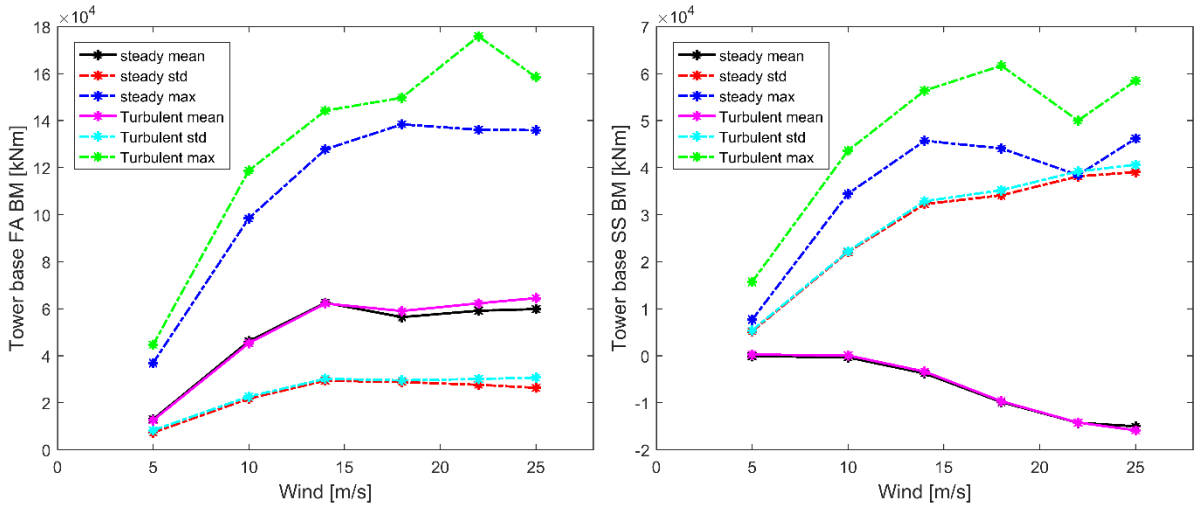

Figure 6.33: Tower base FA and SS bending moments

However, above the rated wind speed, the effect of turbulence the mean FA BM is obvious with larger value under turbulent wind condition than under steady wind condition. This effect continues to increase as wind speed increases above the rated wind speed with a maximum effect at 25m/s wind speed.

The variations from the mean values for the FA BM increases as wind speed increases under both steady and turbulent wind conditions. Furthermore, the effect of turbulence on the load variations from the mean values caused an increasing load variation at wind speeds above the rated wind speed for the FA BM. This effect is largest at 25m/s wind speed.

Consequently, the effect of turbulence on both the mean and load variation for the SS BM is negligible.

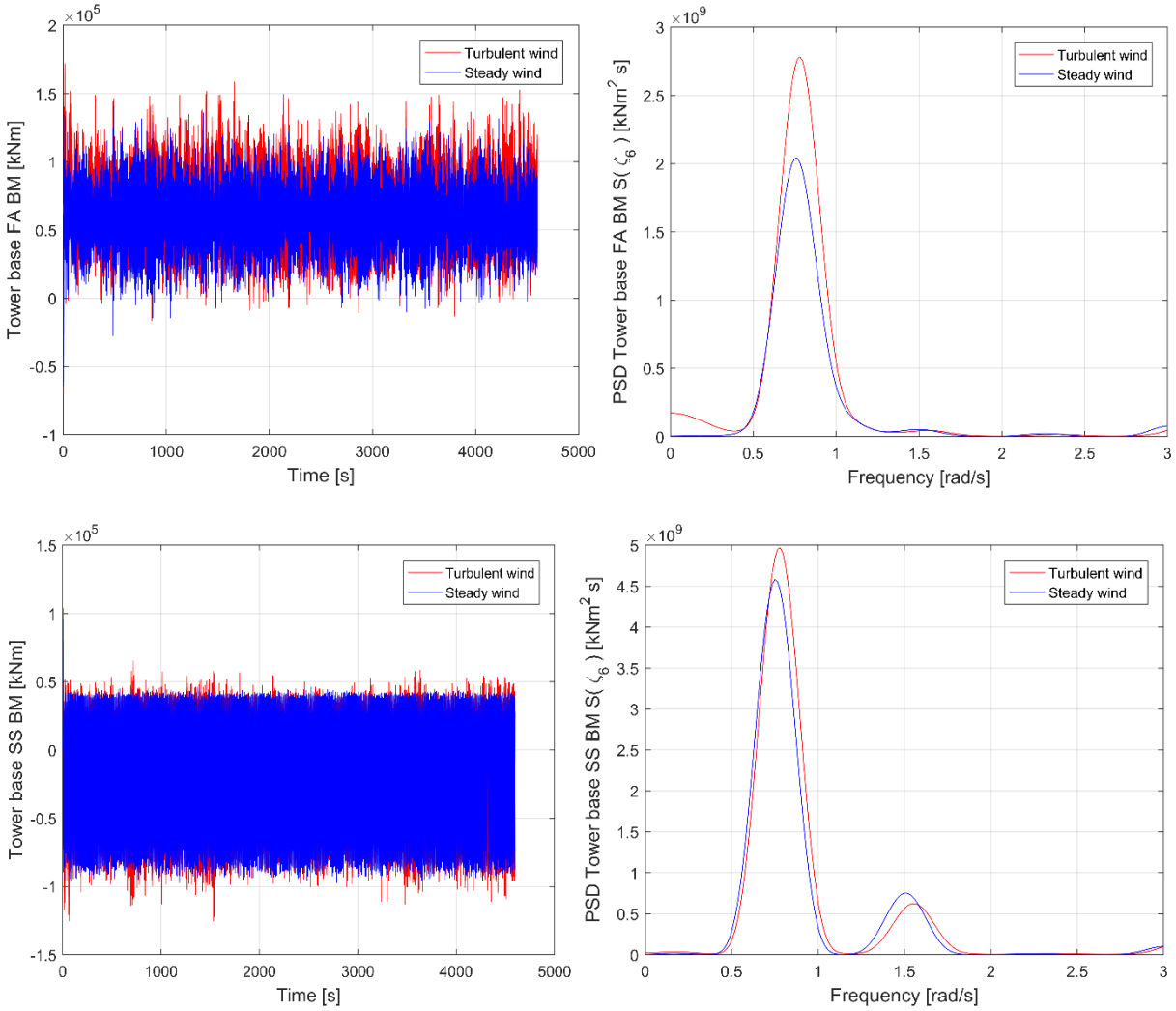

Figure 6.34: Tower Base FA and SS bending moment's time series and PSD for DLC6.

The Bending Moment (BM) time history and the spectral plots are alternative approaches to investigate the effect of turbulence on the tower base BMs. The environmental condition DLC 6 (V = 25 m/s, Hs = 6.02 m and Tp = 12.38 s) based on the discussions in section 6.2.3. (II., i.) and section 6.3.3. (II., i.); the turbulent effects is largest at 25m/s wind speed. The time series and the spectral plots of the FA and the SS BMs at the tower base are shown in **Figure 6.34**. The plots of the BM time history for both FA and SS showed higher amplitudes or spikes under turbulent wind condition than under steady wind condition. It further showed the turbulent effects on both BMs.

This spectral plots embellished the turbulent effects for both FA and SS BMs. The wave frequency

excitation dominates the response for both the FA BM and the SS BM as shown in the spectral plots of **Figure 6.34**.

The spectral plot for the FA BM revealed the wave excitation under turbulent wind condition (red) is higher than under steady wind condition (blue). Similarly, the spectral plot for SS BM showed higher peak at the wave excitation frequency under turbulent wind condition than under steady wind condition.

The second peak at the 2P frequency (observe the shift of the original 2P frequency of about 1.24 rad/s to 1.5 rad/s and 1.6 rad/s at high wind speed (25m/s) under steady wind condition and under turbulent wind condition respectively) on the spectral plots denote the reduced 2P effect under turbulent wind condition for the SS BM. The effect of turbulence on the 2P effect is negligible for the FA BM.

ii. Blade Roots (The Top and the Bottom)

The plots of bending moments at the blade root (top) and (bottom) with coordinates as described in **Table 6.2** are represented in **Figure 6.35** and **Figure 6.36** respectively.

Figure 6.35 showed an increasing and a decreasing mean FA bending moment at the blade root (top) under both wind conditions at wind speeds below and above the rated wind speed respectively. Furthermore, **Figure 6.35 and Figure 6.36** showed there were increasing and decreasing load varaition about the mean FA and the mean SS bending moments at both blade extremes under both wind conditions conditions at wind speeds below and above the rated wind speed respectively.

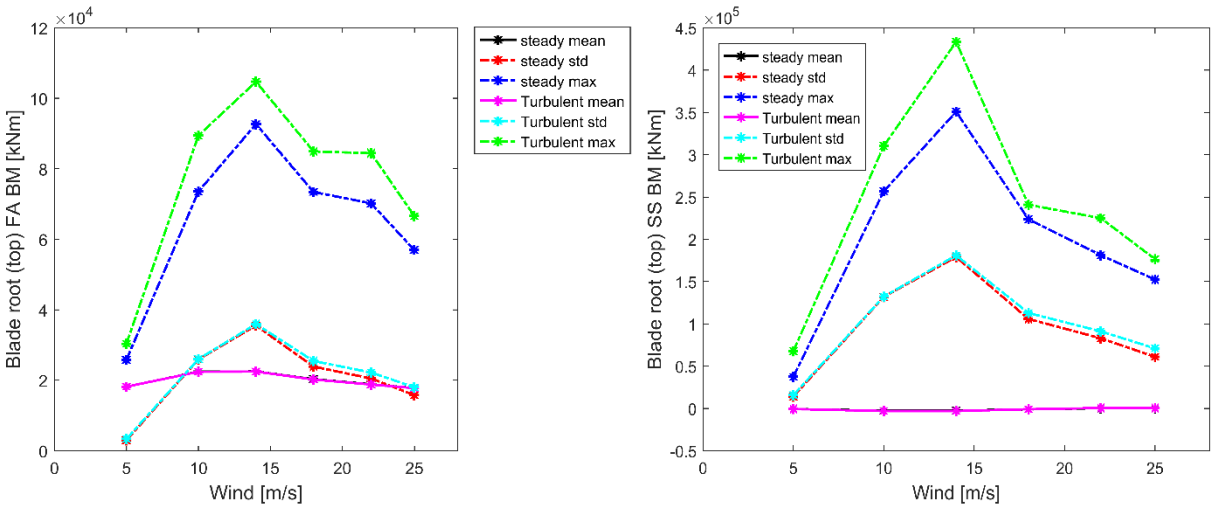

Figure 6.35: Blade root (top) FA and SS bending moments

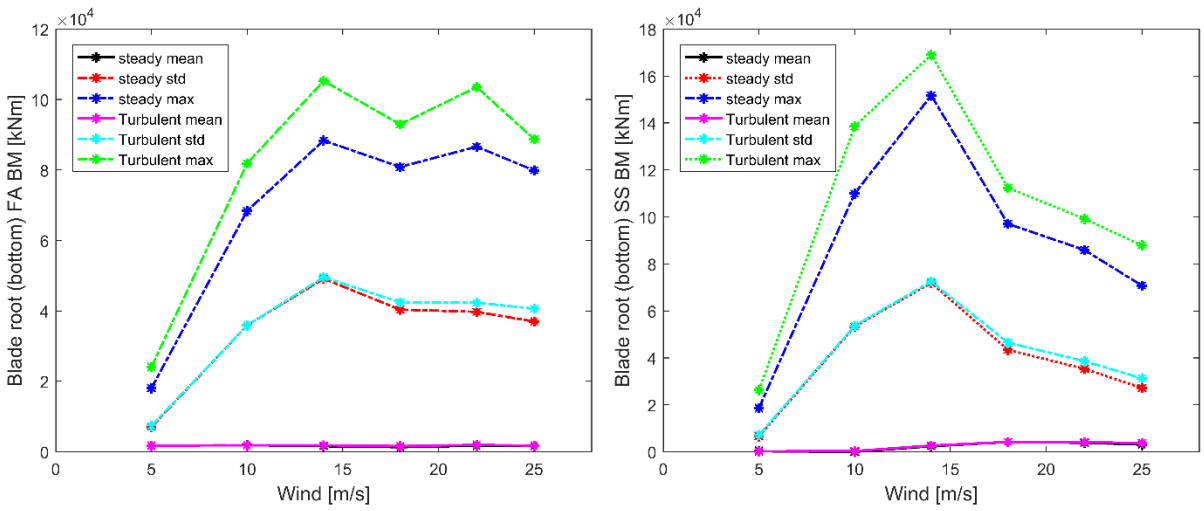

Figure 6.36: Blade root (bottom) FA and SS bending moments

The effect of turbulence on the mean FA and SS bending moments at both blade extremes is negligible as seen in **Figure 6.35 and Figure 6.36**.

The effect of turbulence is almost zero from cut-in wind speed up to 18m/s wind speed. However, above 18 m/s wind speed, the turbulent effects on the load variability is slightly observed within this region of wind speeds. However, This effect remained constant as wind speed increases for both the FA and the SS BMs.

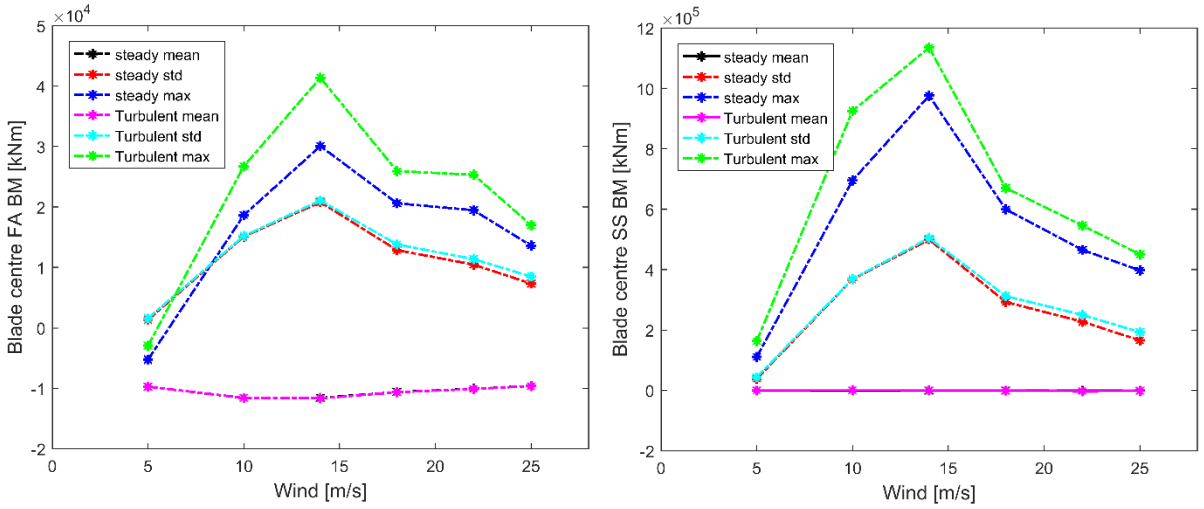

Figure 6.37: Blade center FA and SS bending moments

Figure 6.37 presents plots of the FA and the SS bending moments at the centre of the blade. The effect of turbulence on the mean values is insiginificant at all wind speeds. Also, the turbulence effect resulted in increased load variability at 18m/s wind speed. Above the 18m/s wind speed, the effect of turbulence remained fairly constant.

III. Effect of turbulence on Mooring Lines Tension

Figure 6.38 showed plots of the mooring lines tension against the mean wind speeds.

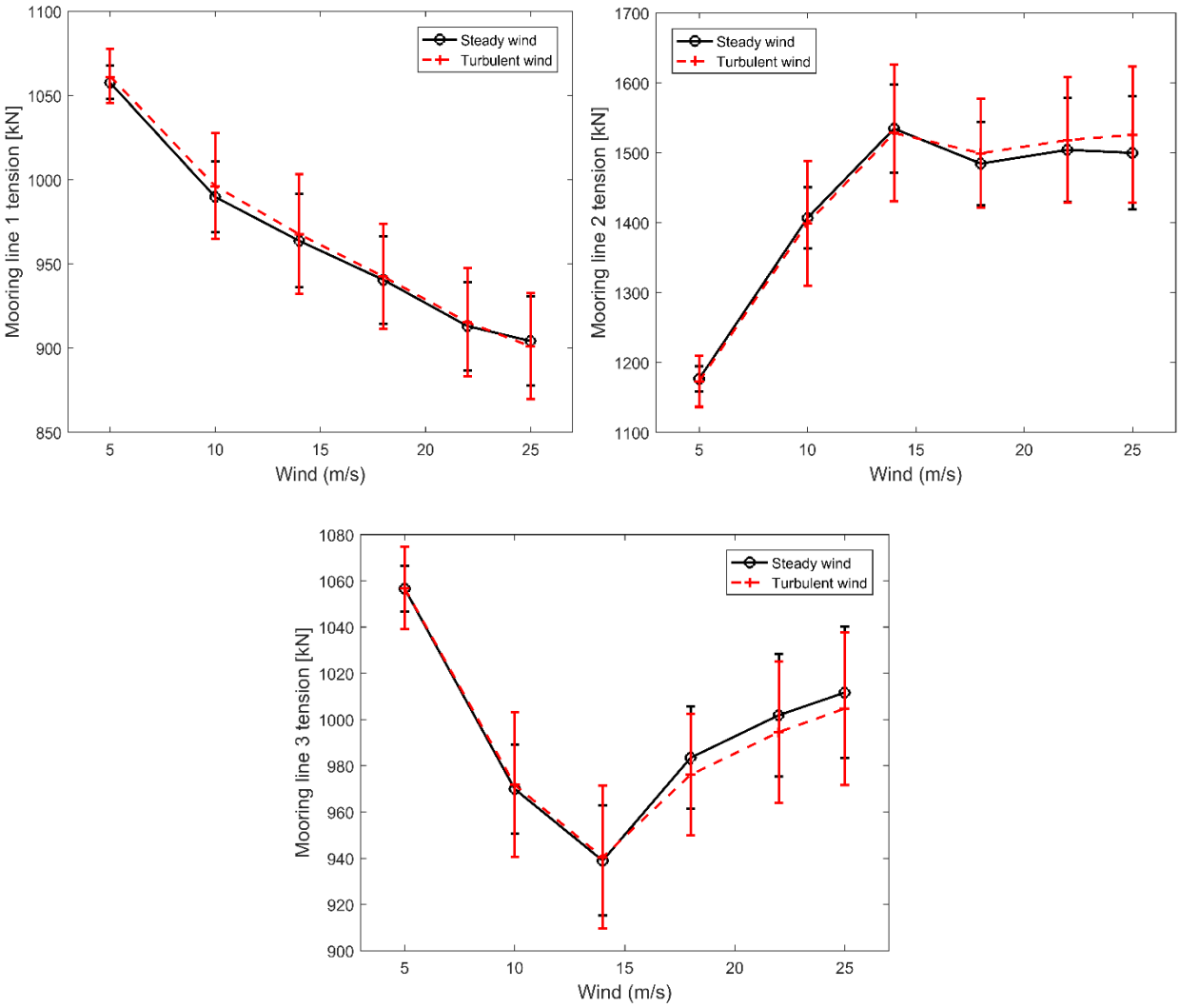

Figure 6.38: Mooring lines tension.

In **Figure 6.38**, the mean tension in mooring line 2 increases as the wind speed increases except at 25 m/s wind speed where it decreased under steady wind condition unlike in mooring line 1 and 3. This is due to the same explanation already discussed in section 6.2.3. (III). This results in increasing tension of mooring line 2 and decreasing tension in mooring line 1 and 3 at wind speeds below the rated wind speed.

The effect of turbulence is obvious in the disparities between the load variability under turbulent wind condition and that under steady wind condition at each mean wind speed for all mooring lines. The load varies higher from the mean values under turbulent wind condition than under

steady wind condition at all wind speeds for all mooring lines. However, the effect of turbulence on the load variation can be generally constant as wind speed increase for all mooring lines.

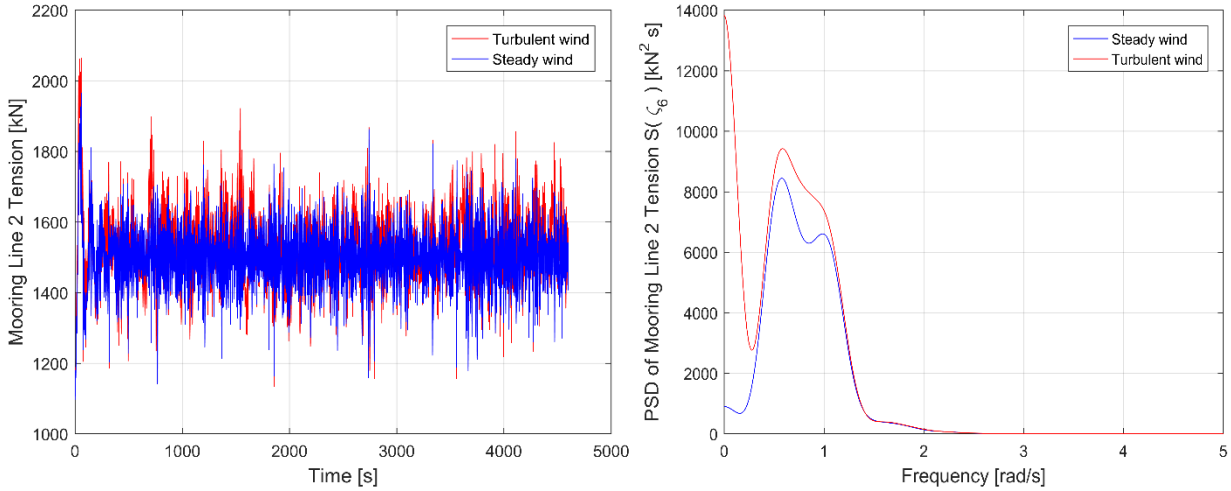

Figure 6.39: Mooring lines tension 2 time series and PSD for DLC6.

The time series plot for DLC6 in **Figure 6.39** showed amplitude of mooring line 2 tension is higher under turbulent wind condition than under steady wind condition effects.

The spectral plot is observed to have higher peaks at the wave excitation frequency under turbulent wind condition (red) than under steady wind condition (blue). This means the mooring lines experienced higher excitation due to wave loads under turbulent wind condition than under steady wnd condition. Furthermore, the reponses at the 2P frequency under both wind condition seems to have died out.

6.4. Comparing the Dynamic response of the 5 MW Baseline and 5 MW Optimized FVAWT

6.4.1. Comparing Generated Powers

The plot in **Figure 6.40** show a comparison between the powers generated by the 5 MW Baseline FVAWT and the 5 MW Optimized FVAWT. As discussed in section 5.3.1, the control model for the 5 MW Baseline FVAWT was adopted for the 5 MW Optimized FVAWT, hence, a significant disparity between the mean power generated by the 5 MW Baseline FVAWT and that by the 5 MW Optimized FVAWT is observed at wind speeds above the rated wind speed.

It was observed that the mean power increases as the wind speed increases for both FVAWT models, a value greater than the 5 MW rated power at the rated speed due to the application of

BL dynamic stall model was obtained. Below the rated wind speed, the 5 MW Optimized FVAWT produced higher power than the 5 MW Baseline FVAWT. A value of about 3 MW and 2.5 MW were reached for the 5 MW Optimized FVAWT and the 5 MW Baseline FVAWT respectively at 10 m/s wind speed.

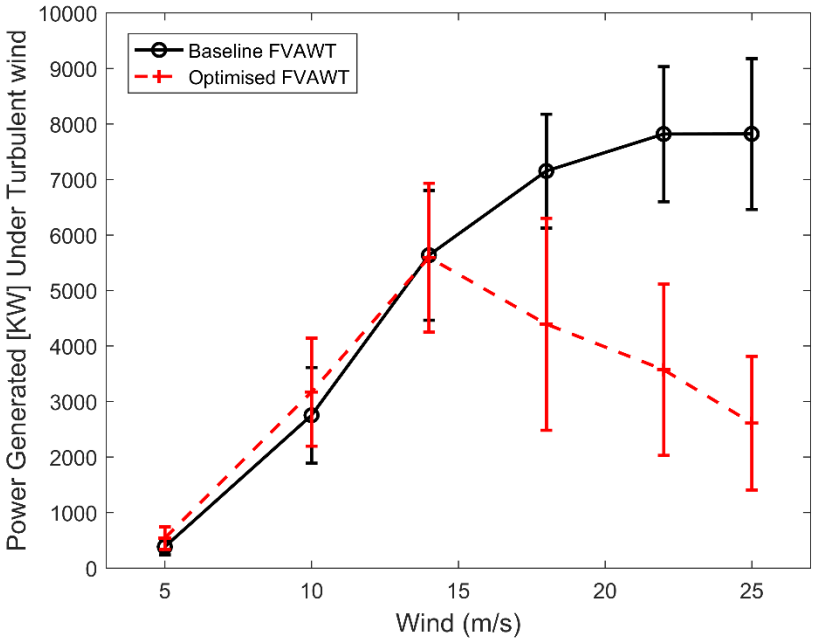

Figure 6.40: Comparing Power generation

In terms of variability in produced power, the plot showed that both FVAWT experienced increasing variability in the generated power as wind speed increases for region below the rated wind speed of 14 m/s. However, the variation in the power produced continued to increase for the 5 MW Baseline FVAWT but decreases for the 5 MW Optimized FVAWT as the wind speed increases above the rated wind speed. This could be attributed to the controller which responds differently at different rotational speed.

6.4.2. Comparing Structural Dynamic Response

In comparing structural responses of both models, the distribution FA and the SS bending moments along the blade and at the tower base were selected as yardsticks for comparison.

Figure 6.41 show the FA and the SS BM distributions along the blade for both FVAWTs under turbulent wind condition. The turbulent wind condition is selcted for this comparison because most of the cases dicussed in the previous sections experienced higher excitation or larger load variations under turbulent wind condition.

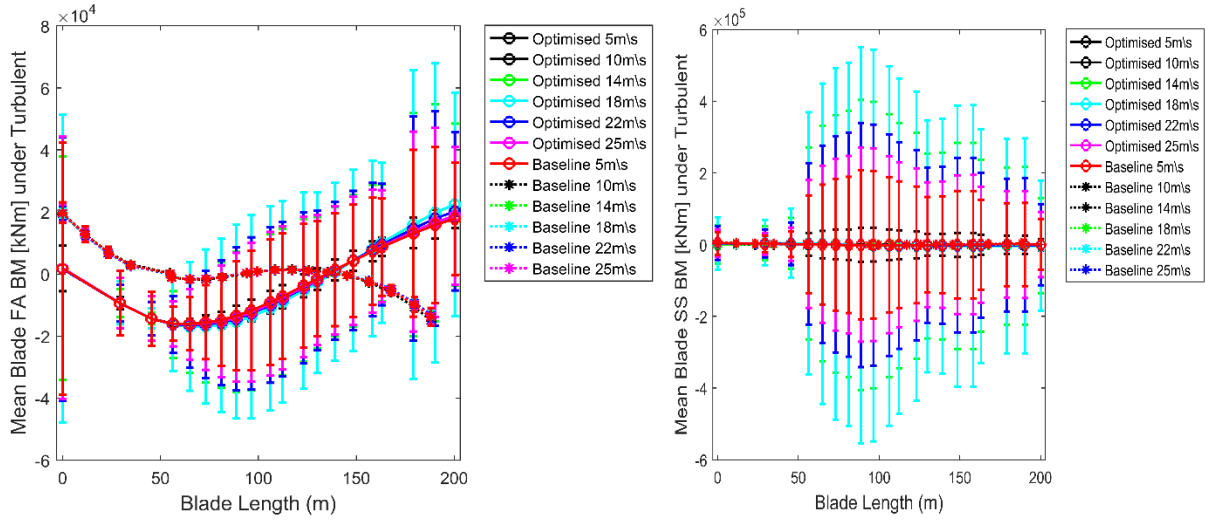

Figure 6.41: Comparing distribution of bending moment along the blade

The bending moment at the blade roots or extremes for the 5 MW Optimized FVAWT is expected to be larger than that of the 5 MW Baseline FVAWT since the rotor for the 5 MW Optimized FVAWT has longer blades and both FVAWT models were simulated under the same environmental conditions. However, at the blade root (bottom) (point zero in the plots along the blade axis), the 5 MW Optimized FVAWT reached its lowest mean value of approximately zero while the 5 MW Baseline FVAWT attained a value of about 2 KNm as shown in **Figure 6.41.**

At the center and blade root (top) (resective last point on the graph along the blade axis), the 5 MW Baseline FVAWT showed lower FA bending moment than the 5 MW Optimized FVAWT.

The mean SS bending moment for both models seemed to agree well, hence a negligible disparity was observed.

The 5 MW Optimized FVAWT showed higher load variation from mean value than the 5 MW Baseline FVAWT as indicated by error bars in **Figure 6.41** for both the FA and the SS bending moments. Furthermore, from the plot of the FA bending moment, the standard deviation for the 5 MW Baseline FVAWT is almost negligible as compared with the 5 MW Optimized FVAWT. This disparity widens as the wind speed increases.

I. Comparing Structural Dynamic Response of Selected Critical Points

i. Comparing Tower Base Bending Moments

The plots in **Figure 6.42** show the value of the mean of the FA, the SS bending moments at the tower base with their respective variation from the mean values in terms of maximum values and standard deviation (std) for both FVAWT models under turbulent wind condition.

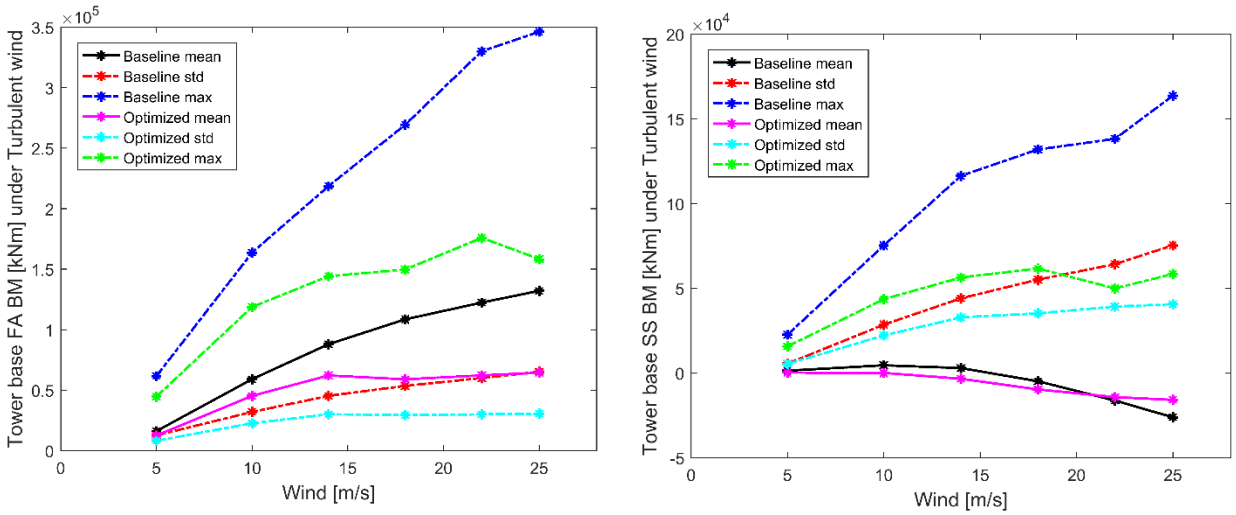

Figure 6.42: Tower base FA and SS bending moments

The plot of the FA BM showed that as the wind speed increases, the mean value for both FVAWTs models increases. Furthermore, the difference between the mean values both FVAWTs increase as wind speed increases. The 5 MW Baseline FVAWT experienced higher FA bending moment than the 5 MW Optimized FVAWT at all wind speeds. In terms of load variation, the load variability (std and max in the plot) for the 5 MW Baseline FVAWT is higher than for the 5 MW Optimized FVAWT. The largest disparity in the FA BM for both FVAWT models occurred at the cut-out wind speed (25m/s) where the 5 MW Baseline FVAWT experienced more than 100% higher mean and maximum FA BM than for the 5 MW Optimized FVAWT.

The SS BM showed similar trend just as the FA BM. The variations from the mean values follow the same trend as discussed for the FA BM. Moreover, the largest disparity in the statistical parameters between both models occurred at 25m/s wind speed as well. However, the mean values for both FVAWT models are very close.

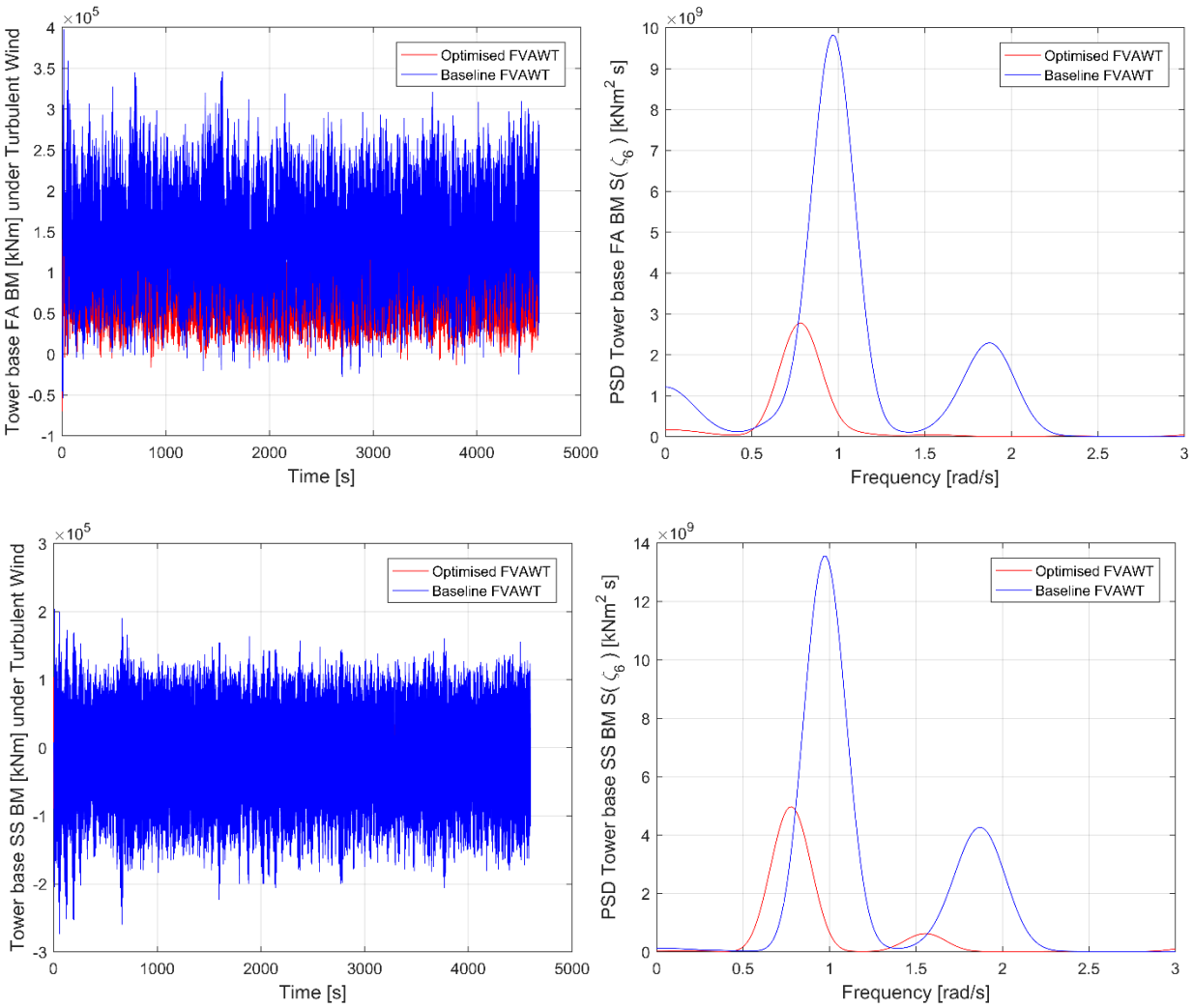

Figure 6.43: Tower Base FA and SS bending moment's time series and PSD for DLC6.

Alternatively, the Bending Moment (BM) time history and the spectral plots can be used to compare the tower base BMs for both FVAWT models. The environmental condition DLC 6 (V = 25 m/s, Hs = 6.02 m and Tp = 12.38 s) based on the discussions in section 6.2.3. (II., i.) and section 6.3.3. (II., i.); the turbulent effects is largest at 25m/s wind speed. The time series and the spectral plots of the FA and the SS BMs at the tower base are shown in **Figure 6.43**. The plots of the BM time history for both FA and SS showed higher amplitude for the 5 MW Baseline FVAWT than for the 5 MW Optimized FVAWT.

This spectral plots further explained the excitations at the wave excitation frequency and the 2P frequency experienced by the 5 MW Baseline FVAWT is higher than that experienced by the 5 MW Optimized FVAWT. This implies the 2P effect at the tower base is reduced by the 5 MW Optimized FVAWT.

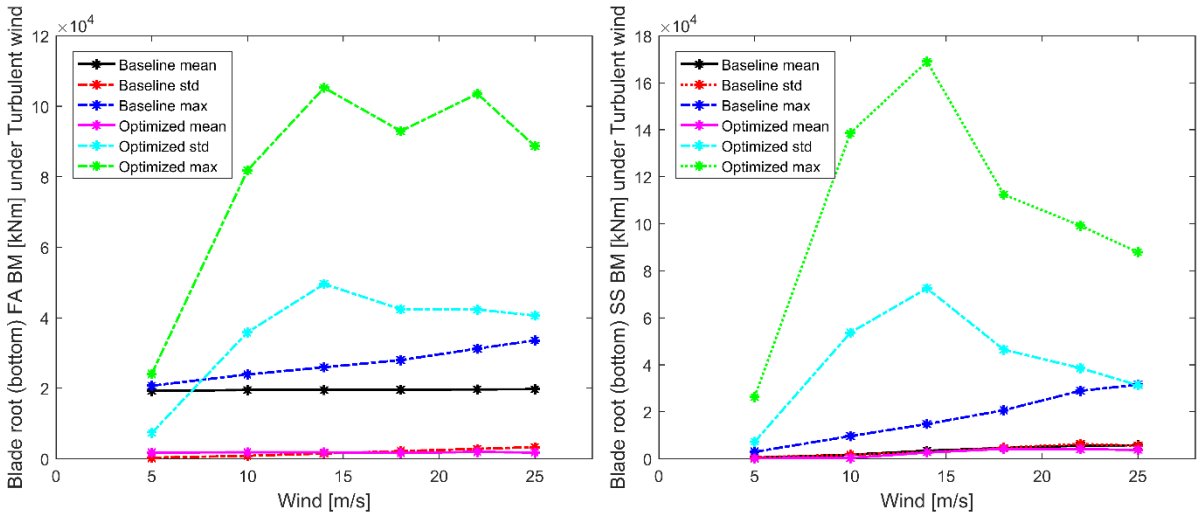

Figure 6.44: Blade root (bottom) FA and SS bending moments

The plots of bending moments at the blade root (bottom) with coordinates as described in **Table 6.2** and **Table 6.3** for the 5 MW Baseline FVAWT and the 5 MW Optimized FVAWT respectively are represented in **Figure 6.44**.

Figure 6.44 showed the mea FA and the mean SS BMs at the blade root (bottom) under both FVAWTs model remained fairly constant as the wind speed increases. Furthermore, the mean FA BM for the 5 MW Baseline FVAWT is twice as large as that for the 5 MW Optimized FVAWT at all wind speeds. However, the 5 MW Optimized FVAWT experienced higher load variation in terms of the load maximum values and the standard deviation than the 5 MW Baseline FVAWT. However, the difference in load variability between the FVAWTs narrows at wind speeds above the rated wind speed.

ii. Comparing Mooring Lines Tension

Figure 6.45 compares the load variability and mean load on mooring lines between the 5 MW Baseline FVAWT and the 5 MW Optimized FVAWT.

The mean load on mooring line 1 and 2 indicate a higher load for the 5 MW Baseline FVAWT is than for the 5 MW Optimized FVAWT while this is opposite the case for mooring line 3. As discussed earlier, the three mooring lines interact among themselves to share the total tension due to environmental loads. Therefore, it is difficult to conclude on which of the FVAWTs performed better in terms of mooring line tension. However, if the difference in the magnitude of the mean loads of all mooring lines for the respective FVAWT are summed at each wind speed,

the 5 MW Optimized FVAWT could be said to have experienced a slightly lower tension than the 5 MW Baseline FVAWT.

In terms of load variability, the error bars for the 5 MW Baseline FVAWT seems to be longer, hence the tension in all mooring lines varies higher in the 5 MW Baseline FVAWT than in the 5 MW Optimized FVAWT.

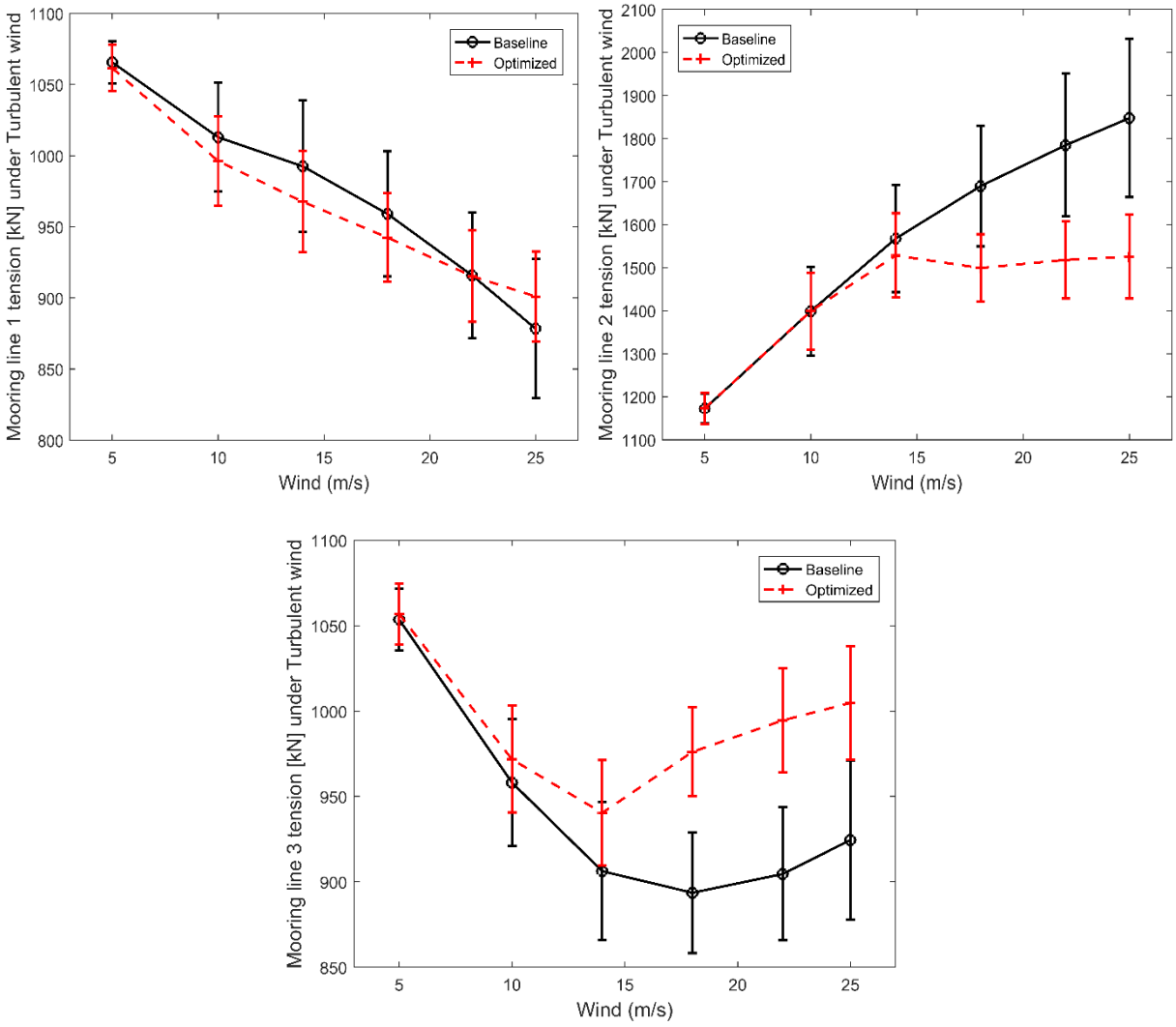

Figure 6.45: Mooring lines tension.

The time series plot for DLC6 in **Figure 6.46** showed that both the mean value and the amplitudes of mooring line 2 tension is higher for the 5 MW Baseline FVAWT than for the 5 MW Optimized FVAWT.

The spectral plot illustrated a higher excitation at the wave excitation frequency for the 5 MW Baseline FVAWT than for the 5 MW Optimized FVAWT. This means the mooring lines experienced

higher excitation due to wave loads for the 5 MW Baseline FVAWT than for the 5 MW Optimized FVAWT. Furthermore, the reponse at the 2P frequency for the 5 MW Optimized FVAWT died out. This further proved the 5 MW Optimized FVAWT experienced a reduced 2P effect than the 5 MW Baseline FVAWT.

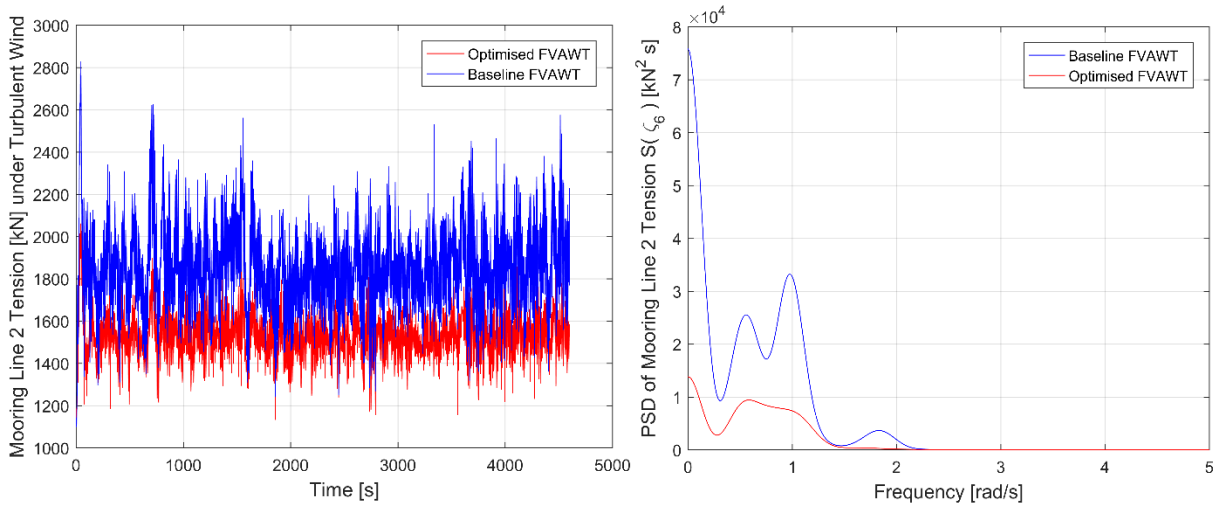

Figure 6.46: Mooring lines tension 2 time series and PSD for DLC6.

6.4.3. Comparing Global motion

The roll and pitch motion at DLC3 (V = 14 m/s, Hs = 3.62 m and Tp = 10.29 s) has been selected as parameters for comparing global motion of both models because it is interesting to investigate the performance of both FVAWT model under the rated wind speed. The roll and pitch motions were selected based on their importance in wind turbine safety.

I. Roll

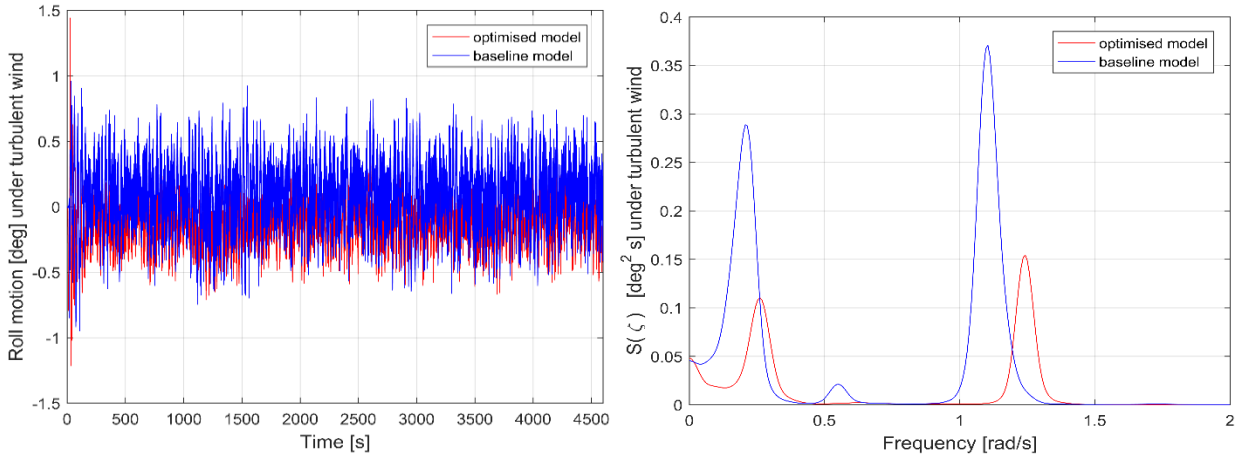

Figure 6.47: Comparing time series and power spectrum of roll motion

II. Pitch

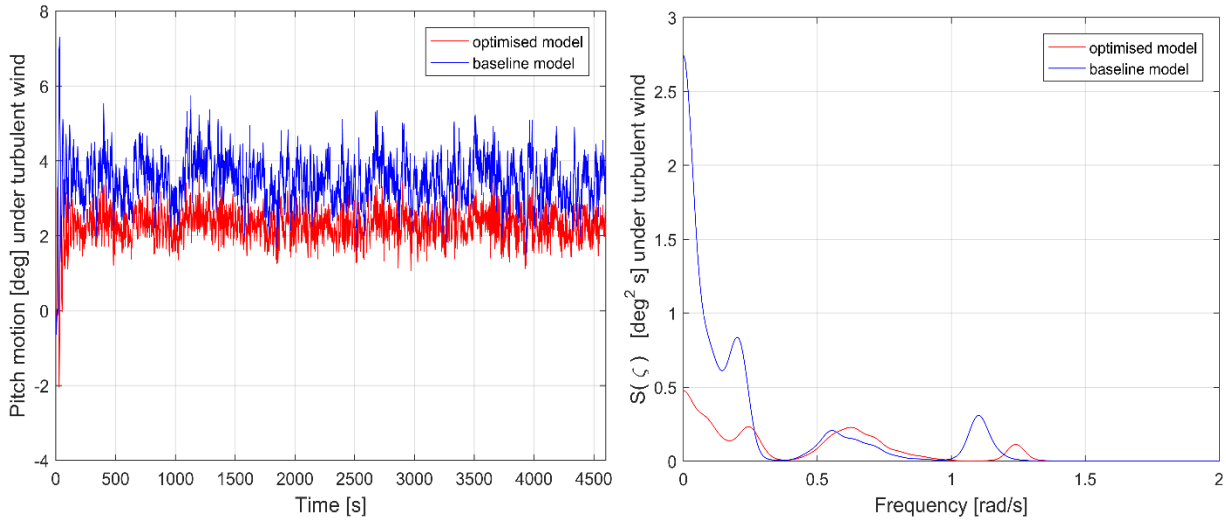

Figure 6.48: Comparing time series and power spectrum of pitch motion

The plots for the roll and the pitch motion time history in **Figure 6.47** and **Figure 6.48** respectively showed a lower motion amplitude for the 5 MW Optimized FVAWT than for the 5 MW Baseline FVAWT. Furthermore, the last two peaks on the spectral plots represents the intensity of the 2P effects for both FVAWT models.

In terms of wave excitation, the 5 MW Optimized FVAWT demonstrated a lower excitation with higher pitch and roll natural frequency when compared with the 5 MW Baseline FVAWT as indicated by the first two peaks in the respective spectral plots.

In the spectral plots, the peaks at the 2P frequency for both roll and pitch motion for the 5 MW Optimized FVAWT (2P frequency = 1.24 rad/s) is observed to be lower than the peaks for the 5 MW Baseline FVAWT (2P frequency = 1.1 rad/s). This demonstrates that the 5 MW Optimized FVAWT experienced a lower excitation at the 2P frequency than the 5 MW Baseline FVAWT.

6.5. Fatigue Analysis of Flexible Element

A short term fatigue analysis for loads at the tower, wind turbine blade and mooring lines were evaluated from results of the fully coupled time domain simulations in Simo-Riflex-DMS. The fatigue analysis in this work is aimed to investigate the Short-Term Damage Equivalent Load (STDEL) due by the tower Bending moments, Blade bending moments and mooring line tension, using the short-term fatigue damage equivalent loads estimation from NREL Mlife toolbox.

The aerodynamic and hydrodynamic loadings are stochastic in nature, hence, it is of pertinent to evaluate fatigue damage based on the time history of simulated responses. The rainflow counting technique, as the best method for fatigue damage estimation, is applied for the cycle counting.

A total of 60 (5 seeds of 6 different environmental conditions with aligned wind and waves) time domain simulations were carried out. The environmental conditions were selected as discussed in section 3.1.5.

The short term fatigue equivalent loads were estimated using Rainflow counting of load histories at the tower base, the blade roots and the mooring lines. An averaged fatigue damage equivalent load over 5 seeds for each of the 6 different design load cases is presented as fatigue damage equivalent load in the subsequent subsection.

6.5.1. Fatigue Analysis of Flexible Element for the 5 MW Baseline FVAWT

The fatigue analysis of flexible elements is focused on the effect of turbulence on the short-term damage equivalent load as discussed in the subsequent subsection.

I. Effect of Turbulence on Short-Term Damage Equivalent (STDEL)

To investigate the effect of turbulence on the Short-Term Damage Equivalent Load (STDEL) of flexible element for the 5 MW Baseline FVAWT, the following positions of high load concentration shown in **Table 6.3** were selected for the fatigue analysis. The estimated Short-Term Damage Equivalent Loads under steady and turbulent wind conditions are shown in **Figure 6.49 (a), (b), (c), (d)** and **(e)** for the tower base, the blade root (bottom), the blade centre, the blade root (top) and the mooring line1 respectively.

Table 6.3: Description of selected positions for fatigue analysis

Nodal points	Coordinates (Y,Z)	Length segment (m)	Description
1	(0.00,0.00)	-	Tower base
2	(0.10,15.074)	0	Blade root (bottom)
3	(62.80, 87.35)	99.50	Blade center
4	(0.00, 144.56)	188.17	Blade root (top)
5	Mooring line 1		

The legends used in the plots for fatigue STDELs are described in **Table 6.4** to fully understand the plots.

Table 6.4: Description of legends as used in the plots

S/N	Legend	Description
1	FA BM steady	STDEL due to FA bending moment under steady wind condition
2	FA BM turbulent	STDEL due to FA bending moment under turbulence wind condition
3	SS BM steady	STDEL due to SS bending moment under steady wind condition
4	SS BM turbulent	STDEL due to SS bending moment under turbulence wind condition
5	steady	STDEL due to axial force or tension under steady wind condition
6	turbulent	STDEL due to axial force or tension under turbulent wind condition

In general, the FA and SS short-term damage equivalent load is observed to be increasing with increasing wind speeds for both wind conditions until a wind speed of 22 m/s is reached when a decrease is experienced for the blade SS STDELs.

The effect of turbulence was observed for all the selected points for fatigue analysis. Furthermore, the effect of turbulence is seen as higher values of STDEL under turbulent wind condition than the steady wind condition. The difference between the STDEL under turbulent wind and steady wind conditions widens as wind speed increases for both SS and FA bending moments but experience a decrease at 25m/s for the SS bending moment. This showed that the SS bending moment at the blade under turbulent wind condition could have a similar damaging effect as the bending moment under steady wind condition at wind speeds above the 25m/s wind speed.

The mooring line STDELs continue to increase with increasing wind speed.

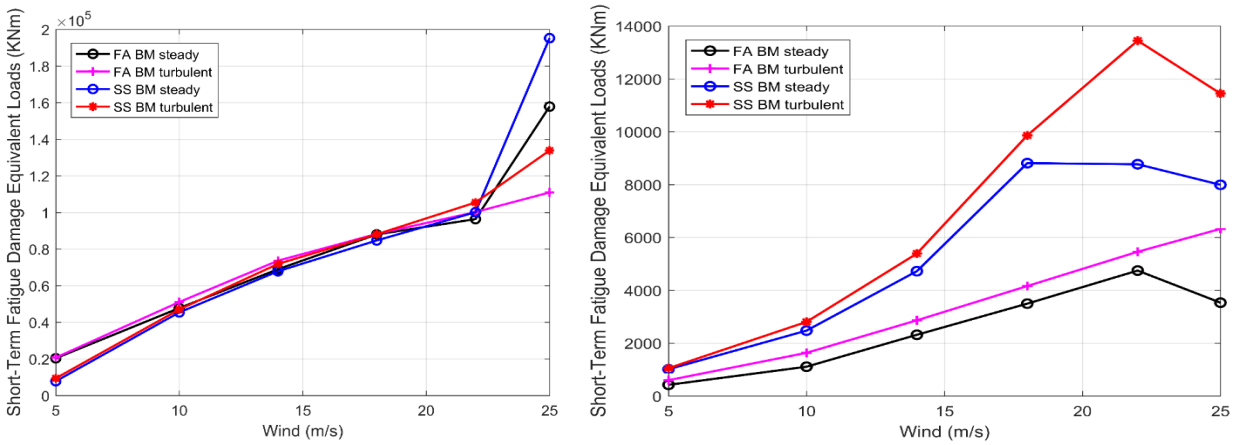

(a) Tower base fatigue equivalent load

(b) Blade root (bottom) fatigue equivalent load

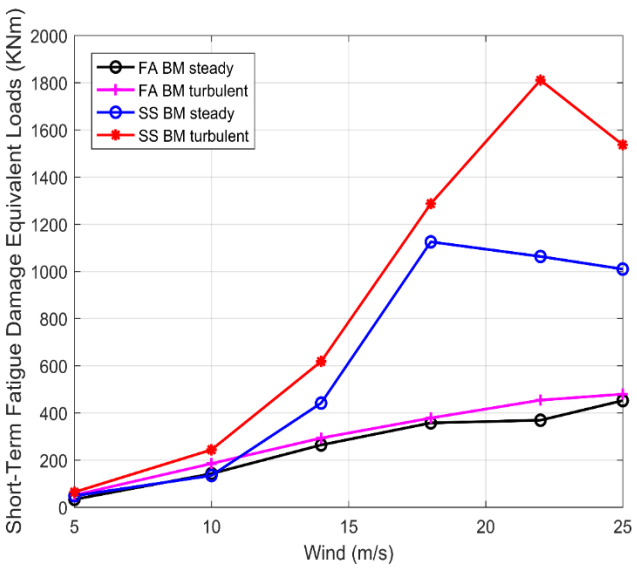

(c) Blade root center fatigue equivalent load

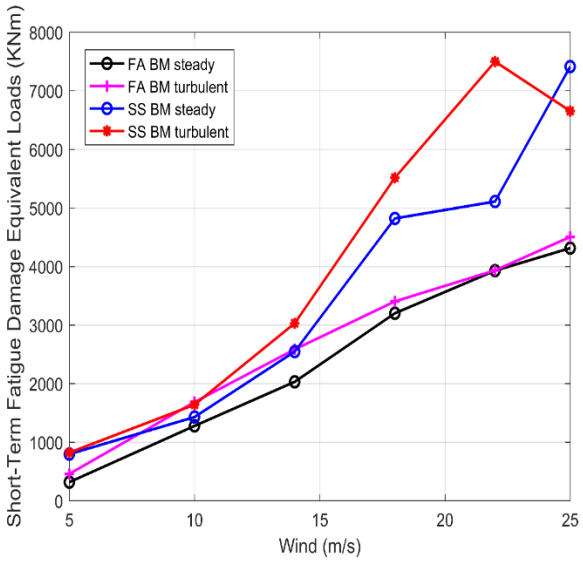

(d) Blade root (top) fatigue equivalent load

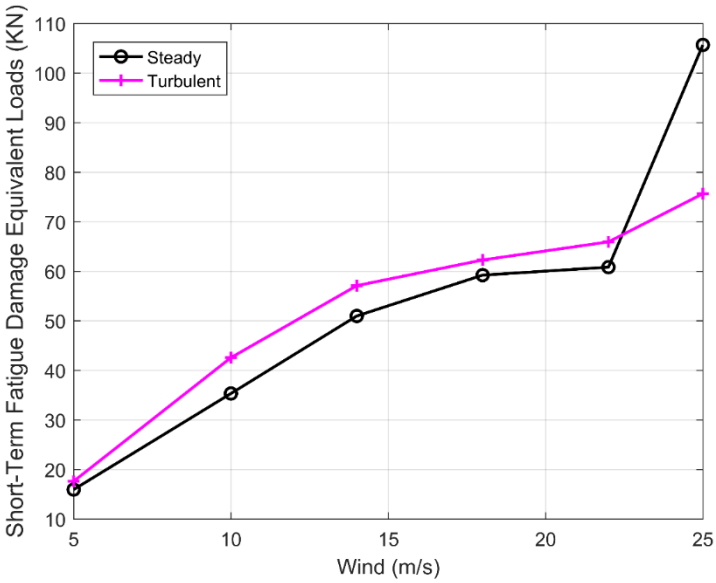

(e) Mooring Line 1 fatigue equivalent load

Figure 6.49: Fatigue STDEL of selected areas

6.5.2. Fatigue Analysis of Flexible Element for the 5 MW Optimized FVAWT

I. Effect of Turbulence on Short-Term Damage Equivalent

Similar to the discussion in section 6.5.1, the following areas were selected for fatigue analysis for the 5 MW Optimized FVAWT in order to ease comparison of results with the 5 MW Baseline FVAWT. The selected points are detailed in **Table 6.5.**

Table 6.5: Description of selected positions for fatigue analysis

Nodal points	Coordinates (Y,Z)	Length segment (m)	Description
1	(0.00,0.00)	-	Tower base
2	(0.10,15.074)	0	Blade root (bottom)
3	(54.80, 93.17)	112.35	Blade center
4	(0.00, 158.00)	200.31	Blade root (top)
5	Mooring line one		

The estimated the short term fatigue damage equivalent load under steady and turbulent wind condition are shown in **Figure 6.50 (a), (b), (c), (d)** and **(e)** for the tower base, the blade root (bottom), the blade centre, the blade root (top) and the mooring line1 respectively.

The plots revealed increasing and decreasing STDEL values for wind speeds below and above the rated wind speeds respectively, with the STDEL value for the turbulent wind condition attaining the higher values than for the steady wind condition for all wind speeds. The plots furthermore demonstrate that wind speeds farther from the rated wind speed (14 m/s) could have lower damaging effect than wind speeds closer to the rated wind speed for this FVAWT model.

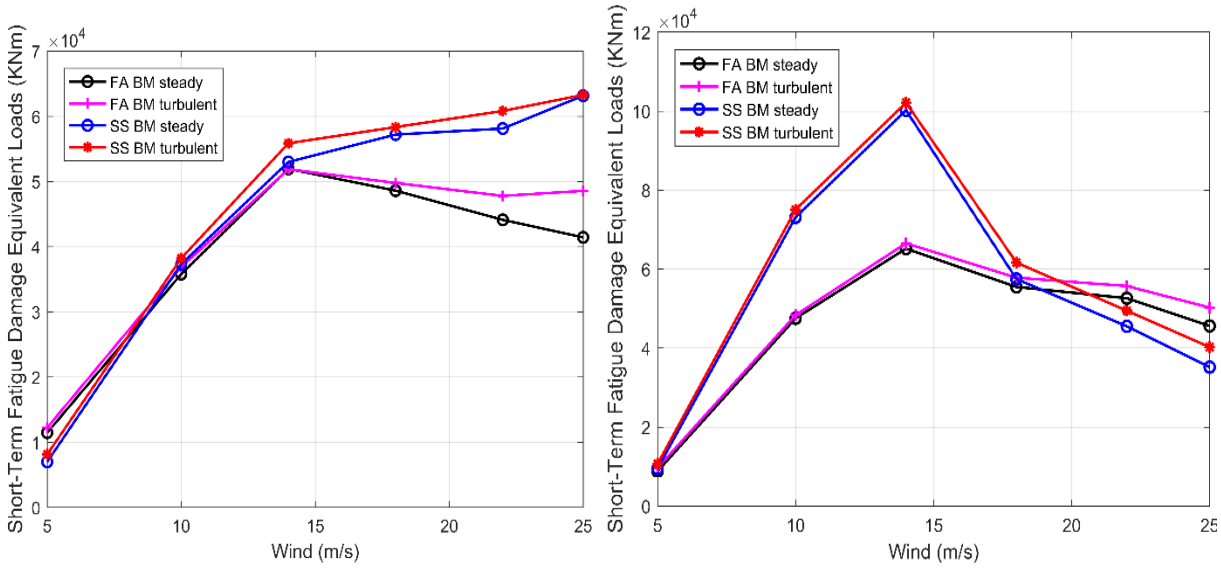

(a) Tower base fatigue equivalent load

(b) Blade root (bottom) fatigue equivalent load

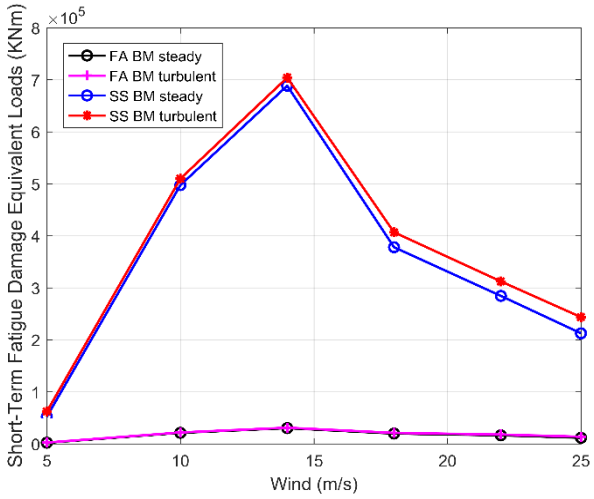

(c) Blade root center fatigue equivalent load

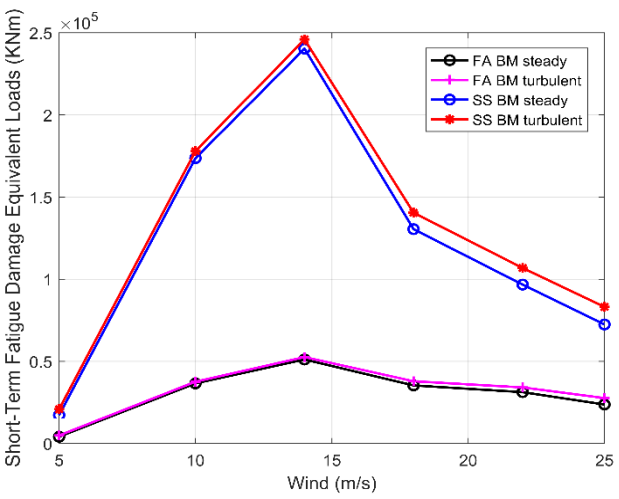

(d) Blade root (top) fatigue equivalent load

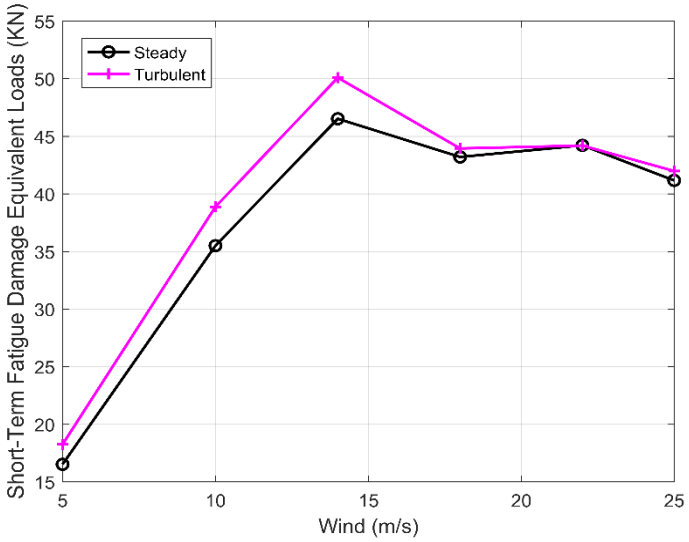

(e) Mooring Line fatigue equivalent load

Figure 6.50: Fatigue STDEL of selected areas

6.5.3. Comparing Fatigue Damage

In this subsection, the STDELs at some selected positions were compared between the 5 MW Optimized FVAWT and the 5 MW Baseline FVAWT. The tower base and the blade root (bottom) positions proved to have higher STDELs values than other points selected for fatigue analysis in the previous sections. Therefore, the two points were selected for STDEL comparison between both models under turbulent wind condition. Furthermore, the fatigue damage due to tension in mooring line 1 was selected for comparison as well.

The description of legends as used in the plots are shown in **Table 6.6.**

Table 6.6: Description of legends as used in the plots

S/N	Legend	Description
1	Optimized FA BM	STDEL due to FA bending moment for the 5 MW Optimized FVAWT
2	Baseline FA BM	STDEL due to FA bending moment for the 5 MW Baseline FVAWT
3	Optimized SS BM	STDEL due to SS bending moment for the 5 MW Optimized FVAWT
4	Baseline SS BM	STDEL due to SS bending moment for the 5 MW Baseline FVAWT
5	Optimized	STDEL due to axial force for the 5 MW Optimized FVAWT
6	Baseline	STDEL due to axial force for the 5 MW Baseline FVAWT

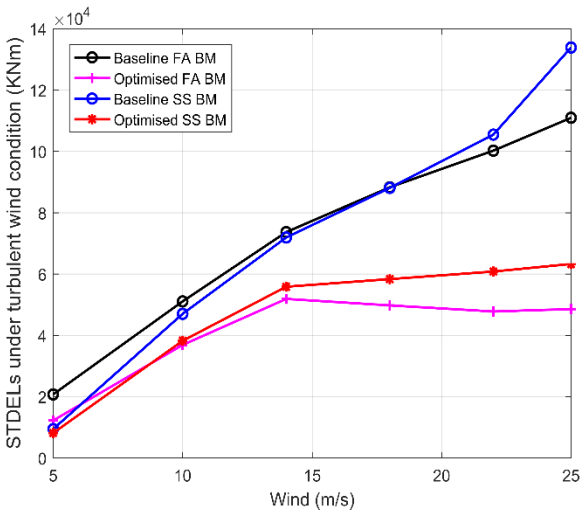

(a) Tower base fatigue equivalent load

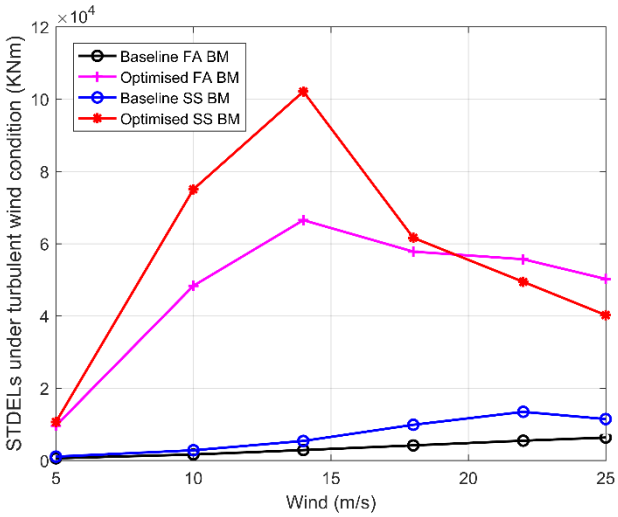

(b) Blade root (bottom) fatigue equivalent load

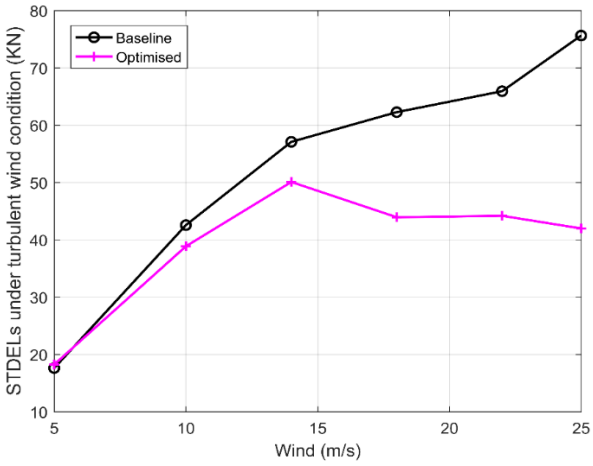

(e) Mooring Line fatigue equivalent load

Figure 6.51: Fatigue STDEL of selected areas

The plots in **Figure 6.40 (a)**, **(b) and (c)** compare the STDELs as described in **Table 6.6** for the tower base, the blade root (bottom) and the mooring line 1 respectively.

In terms of STDELs due to FA bending moment in **Figure 6.51 (a)**, the 5 MW Baseline FVAWT experienced higher STDELs at all wind speeds than the 5 MW Optimized FVAWT at the tower base. However, it experienced a lower value than the 5 MW Optimized FVAWT at the blade root (bottom) as shown in **Figure 6.51 (b)** up to 18 m/s wind speed and then the scenario was reversed. This showed, the 5 MW Optimized FVAWT could experience lower damaging load due to the SS bending moment at higher wind speeds than the 5 MW Baseline FVAWT.

In terms of STDELs due to mooring line tension in **Figure 6.51 (c),** an increasing disparity is observed between the STDELs for the 5 MW Baseline FVAWT and the 5 MW Optimized FVAWT as the wind speed increases. Furthermore, the 5 MW Baseline FVAWT doubled the STDELs for the 5 MW Optimized FVAWT at the cut-out wind speed of 25 m/s for the tower base SS bending moment.

7 Conclusion and recommendations for future work

This work aimed to apply the coupled model for dynamic analysis of FVAWTs. The dynamic responses of two FVAWTs were analyzed based on time domain simulations for a coupled model under normal operating conditions of the FVAWTs. In addition, the 5 MW Baseline FVAWT is compared with the 5 MW Optimized FVAWT to better evaluate the level of optimisation that was achieved from the baseline concept.

This chapter contains the important conclusions and recommendations for future work.

7.1. Conclusions

The main conclusions of this thesis are:

- The effect of turbulence on power production of the two FVAWTs resulted in an increased power generation and higher power variation.
- The statistical analysis of the dynamic responses of both FVAWTs under turbulent and steady wind condition exhibited similar trends. The comparisons between the statistical parameters (the mean values, standard deviations and maximum values) of selected response parameters (BM and tension, global motions in six DOFs,) under steady wind and turbulent wind conditions revealed the effect of turbulence on the global motions and the structural responses. For the 5 MW Optimized FVAWT global motions, it was observed that the amplitude of motions are clearly higher under turbulent wind condition than under steady wind condition under both design load cases (DLC3 and DLC6) for all 6 degree of freedom motion.
- For the tower base bending moments, the statistical results revealed that as the wind speed increases, the effect of turbulence on the mean values remained relatively low but became significant at wind speeds above 18m/s with a larger bending moment under turbulent wind condition. The turbulent effect resulted is prominent in the load variation

than in the mean values. The effect of turbulence had its largest effects at 25m/s wind speed.

- For the blade bending moments, the blade bending moment distribution for both FVAWT rotors revealed the positions of high bending were at the blade extremes. Furthermore, the 5 MW Optimized FVAWT experienced high bending at the blade center, while this is considered negligible when compared with the bending moment at the blade extremes for the 5 MW Baseline FVAWT. The effect of turbulence is insignificant for the mean values especially for the 5 MW Baseline FVAWT. This effect for the 5 MW Optimized FVAWT was almost zero from cut-in wind speed up to 18m/s wind speed. However, above 18 m/s wind speed, the turbulent effects on the load variability is obvious within this region of wind speeds. However, the turbulent effects had its greatest effect on variation of the blade bending moment from the mean values rather than mean values.

- Through the spectral analysis of the global motions, the tower base and the blade BMs, and the mooring lines tension under two wind conditions (steady wind and turbulent wind), the effect of 2P frequency on the structural responses and global motions were identified. The 2P effect resulting from the VAWT rotation leads to large fluctuations of the aerodynamic loads on the rotor, the internal loads in the rotor, the internal loads in the mooring line tension and the tower base, and the motion amplitude even in steady wind conditions. Furthermore, the 2P frequency experienced a shift from the natural 2P frequency (for 2-bladed VAWTs, 2P frequency is twice the rated rotational speed) at higher wind speeds. Furthermore, the spectral analysis of both FVAWTs under two load cases (DLC3 and DLC6), demonstrated that the 2P effect increases as the wind speed increases, this demonstrate the importance of the 2P effect at high wind speeds in the operational conditions.

- The power spectra of the tower base and the blade BMs, the mooring lines tension, and the global motions in six DOFs under turbulent condition and under steady wind condition were compared with further evaluate the effect of turbulence on these parameters. From the power spectra plots, the contributions to the differences in the load variation under the respective wind conditions were identified at different frequencies. This further revealed that low-frequency responses were tremendously excited by the turbulent wind except for the heave motion which exhibited the opposite response. Furthermore,

responses at the 2P frequency is prominent in the roll and the pitch motions. However, the 2P effect is reduced by the turbulent wind.

- The structural integrity and fatigue damage in the VAWTs is significant. The comparison of the Short-Term fatigue Damage Equivalent Loads (STDEL) due to the tower base bending moments, the blade root (bottom) bending moment and the mooring line 1 tension under steady wind and under turbulent wind conditions for the 5MW Baseline FVAWT revealed the effect of turbulence leads to higher STDELs. The effect of turbulence was observed for all the selected points for fatigue analysis. The difference between the STDEL under turbulent wind and steady wind conditions widens as wind speed increases for both SS and FA bending moments but experience a decrease at 25m/s for the SS bending moment. This showed that the SS bending moment at the blade under turbulent wind condition could have a similar damaging effect as the bending moment under steady wind condition at wind speeds above the 25m/s wind speed. The statistical analysis of STDELs for the 5MW Optimized FVAWT showed rapid drop in STDEL values at wind speeds above the FVAWT rated wind speed, this further indicates that the induced loads on the FVAWT under turbulent wind condition could have a similar damaging as under steady wind condition effect at wind speeds above the rated wind speed. Also, the statistical results demonstrated that at wind speeds farther from the rated wind speed (14 m/s), the internal loads could have lower damaging effect than at wind speeds closer to the rated wind speed for this FVAWT model. In terms of STDELs, the 5 MW Baseline FVAWT experienced larger short-term fatigue damage than the 5 MW Optimized FVAWT as the wind speed increases with twice as large as the STDELs for the 5 MW Optimized FVAWT at the cut-out wind speed of 25 m/s for the tower base SS bending moment.
- A comparison between the 5MW Optimized FVAWT and the 5MW Baseline FVAWT in terms of power production, structural responses, global motion and STDELs. Below the rated wind speed, the 5 MW Optimized FVAWT produced higher power than the 5 MW Baseline FVAWT. A value of about 3 MW and 2.5 MW were reached for the 5 MW Optimized FVAWT and the 5 MW Baseline FVAWT respectively at 10 m/s wind speed. However, the variation in the power produced continued to increase for the 5 MW Baseline FVAWT but decreases for the 5 MW Optimized FVAWT as the wind speed increases above the rated wind speed. This implies if an improved controller for the 5 MW

optimized FVAWT is applied, the generated power will more than that generated by the 5 MW base line FVAWT, especially below the rated wind speed. That means cost of energy (COE) will be reduced for the 5 MW optimized FVAWT.

- Comparisons between the results of spectral analysis of the global motions showed the 5 MW Optimized FVAWT experienced a lower excitation at the wave excitation frequency than the 5 MW Baseline FVAWT. Furthermore, the 5 MW Optimized FVAWT experienced a lower excitation at the 2P frequency than the 5 MW Baseline FVAWT. This implies a reduced 2P effects for the 5 MW Optimized FVAWT.

7.2. Recommendations for Future Work

The following recommendation should be considered for further work on FVAWTs;

7.2.1. General comments

The recommendations proposed by Wang in his PhD thesis [71] should be considered for further work with the exception of the fatigue analysis which has been well discussed in this thesis.

7.2.2. Specific recommendations

Control model for the 5MW Optimised FVAWT

The control for the 5MW Baseline FVAWT was adopted for the 5MW Optimised FVAWT in this thesis. However, due to the unigueness of the 5MW Optimised FVAWT in terms of rated rotational speed and rotor geometry, it is recommended to develop a unique control model for the 5MW Optimised FVAWT to fully investigate its performance and responses.

Wave-wind misaligned condition for the 5MW Optimised FVAWT

The environmental condition used in this work is an aligned wave-wind condition. In reality, this is not always the case as wind and wave often changes direction of propagation. Therefore, the author recommeds an analysis to be performed to evaluate the effect of the wave-wind misaligned condition on the dynamic response of the 5MW Optimised FVAWT.

Effect of current on the mooring line dynamics and platform global motions for the 5MW Optimised FVAWT

Although, the effect of current on the FVAWT global motion and mooring lines tension has been considered negligible in this thesis, however, this could be further investigated to justify the assumption.

References

[1] Corbetta G., Mbistrova A., and Ho A., "Wind in power " European Wind Energy Association (EWEA)February 2016 2016.

[2] Zervos A. and Kjaer C., "Pure Power - Wind Energy scenarios up to 2030," *European Wind Energy Association (EWEA),* 2008.

[3] Obdam T. and Zee T. V. d., "ECN O&M Tool Case Study for a Far Offshore Wind Farm. ," 2011.

[4] Rademakers L. W. M. M., Braam H., Obdam T. S., Frohböse P., and Kruse N., "Tools For Estimating Operation and Maintenance Costs of Offshore Wind Farms: State of the Art," presented at the EWEC 2008, Brussels, Belgium, 2008.

[5] "Part 1 — Early History Through 1875," ed: TelosNet Web Development and Darrell Dodge, Retrieved 2016-03-15.

[6] Drachmann A. G., "Heron's Windmill," vol. 7, pp. 145–151, 1961.

[7] Price and Trevor J. Blyth, James (1839–1906) [Online].

[8] Breton S.-P. and Moe G., "Status, plans and technologies for offshore wind turbines in Europe and North America,," *Renewable Energy* vol. 34, pp. 646-645, July 2008 2009.

[9] Paul S. D. Floating Wind Turbines [Online]. Available: http://web.mit.edu/windenergy/windweek/Presentations/P6%20-%20Sclavounos.pdf

[10] Heidi V. World's first floating wind farm: the key to broadening wind power's reach? [Online]. Available: http://www.power-technology.com/features/featureworlds-first-floating-wind-farm-the-key-to-broadening-wind-powers-reach-4809545/

[11] Tande J. O. G. (2014, March 07, 2016). *Fixed Offshore Wind Turbine Concepts*. Available: https://www.sintef.no/en/projects/nowitech-norwegian-research-centre-for-offshore-wi/

[12] Estate T. C., "The Crown Estate – UK Market Potential and Technology Assessment for floating offshore wind power," The Crown Estate, UK2012.

[13] Maples B., Saur G., Hand M., Pietermen R. v. d., and Obdam T., "Installation, Operation, and Maintenance Strategies to Reduce the Cost of Offshore Wind Energy," National Renewable Energy Laboratory, Energy Research Centre of the NetherlandsJuly 2013 2013.

[14] Darrieus G. J. M., "Turbine having its rotating shaft transverse to the flow of the current " 1835018, 1926.

[15] Coiro D., Nicolosi F., Marco A. D., Melone S., and Montella F., "Dynamic behaviour of patented Kobold tidal current turbine: numerical and experimental aspects," in *Proceeding of the 4th International Conference on Advanced Engineering Design*, Glasgow, UK, 2004.

[16] Ashwill T. D. and Leonard T. M., "Developments in blade shape design for a Darrieus vertical axis wind turbine," Sandia National Laboratories, Albuquerque, New Mexico (US)1986.

[17] Sheldal R. E., "Comparison of field and wind tunnel Darrieus wind turbine data," Sandia National Laboratory, Albuquerque, New Mexico (US)1981.

[18] Blackwell B. F., Sheldahl R. E., and Feltz L. V., "Wind tunnel performance data for the Darrieus wind turbine with NACA 0012 blades," Sandia National Laboratory, Albuquerque, New Mexico (US)1977.

[19] Sheldal R. E., Klimas P. C., and Feltz L. V., "Aerodynamic performance of a 5-metre-diameter turbine with extruded alluminum NACA 0015 blades," Sandia National Laboratories, Albuquerque, New Mexico (US)1980.

[20] Ashwill T. D., "Measured data fore the Sandia 34-meter vertical axis wind turbine," Sandia National Laboratories, Albuquerque, New Mexico (US)1992.

[21] Ashwill T. D., "Initial structure response measurements and model validation for the Sandia 34-Meter VAWT test bed," Sandia National Laboratories, Albuquerque, New Mexico (US)1990.

[22] Carne T. G. and Nord A. R., "Modal testing of rotating wind turbine," Sandia National Laboratories, Albunquerque, New Mexico (US)1983.

[23] Berg D. E., "Structural design of the Sandia 34-meter vertical axis wind turbine," Sandia National Laboratories, Albequerque, New Mexico (US)1985.

[24] Ralph M. E., "Design and Control of the variable speed generator on the Sandia 34-meter vertical axis wind turbine," in *Proceedings of the Windpower Conference*, San Francisco, California (US), 1989, pp. 55-59.
[25] Corporation F., "Final project report: high energy rotor development, test and evaluation," Flowind Corporation, Sandia Contract AB-7292, San Rafael, California (US1996.
[26] Carlin P. W., Laxson A. S., and Muljadi E. B., "The hystory and state of the art of variable speed wind turbine technology," *Wind Energy,* vol. 6, pp. 129-159, 2003.
[27] Paravischivoiu I., "Wind Turbine Design: With Emphasis on Darrieus Concept," in *Polytechnic International Press*, ed. Montreal, 2002.
[28] Beller C., "Urban wind energy - state of the art 2009," Risø DTU Roskilde, Denmark2009.
[29] Unit R. E. t. T. B. D., "The world offshore renewable energy report 2004-2008," London (UK2008.
[30] Henderson A. R. and Witch D., "Floating offshore wind energy - A review of the current status and an assesment of the prospects," *Wind Engineering,* vol. 34, pp. 1-16, 2010.
[31] Musial W. and Ram B., "Large-scale offshore wind power in the United States - Assesment of opportunities and barriers," National Renewable Energy Laboratory, Golden, Colorafo (US)2010.
[32] Musial W. and Butterfield C., "Future for offshore wind energy in the United States," in *Proceedings of the Energy Ocean Conference*, Palm Beach, FL, 2004.
[33] Stoddard W., "The life and work of Bill Heronemus, wind energy pioneer," *Wind Engineering,* vol. 26, pp. 335-341, 2002.
[34] Karimirad M. and Moan T., "Wave- and Wind-Induced Dynamic Response of a Spar-Type Offshore Wind Turbine," *JOURNAL OF WATERWAY PORT COASTAL AND OCEAN ENGINEERING,* vol. 138, pp. 9-20, 2012.
[35] Kvittem M. I., Bachynski E. E., and Moan T., "Effects of Hydrodynamic Modelling in Fully Coupled Simulations of a Semi-submersible Wind Turbine," *EGYPRO Energy Procedia,* vol. 24, pp. 351-362, 2012.
[36] Luan C., Gao Z., and Moan T., "Modelling and analysis of a semi-submersible wind turbine with a central tower with emphasis on the brace system," in *Proceedings of the 32nd International Conference on Ocean, Offshore and Arctic Engineering*, Nantes, France, 2013.
[37] Bachynski E. E. and Moan T., "Design considerations for tension leg platform wind turbines," *Marine Structures,* vol. 29, pp. 89-114, 2012.
[38] DNV-GL. Electrifying the future: Third generation wind power [Online]. Available: https://www.dnvgl.com/technology-innovation/broader-view/electrifying-the-future/third-generation-wind-power.html
[39] Jiang Z., Karimirad M., and Moan T., "Dynamic response analysis of wind turbines under blade pitch system fault, grid loss, and shutdown events," *Wind Energy,* vol. 17, pp. 1385-1409, 2014.
[40] Karimirad M. and Moan T., "Stochastic dynamic response analysis of a tension leg spar-type offshore wind turbine," *Wind Energy,* vol. 16, pp. 953-973, 2013.
[41] Kvittem M. I. and Moan T., "Effect of Mooring Line Modelling on Motions and Structural Fatigue Damage for a Semi-submersible Wind Turbine," in *Proceedings of the Twenty-second International Offshore and Polar Engineering Conference.*, Rhodes, Greece, 2012.
[42] Kvittem M. I. and Moan T., "Frequency versus time domain fatigue analysis of a semi-submersible wind turbine tower," in *ASME 2014 33rd International Conference on Ocean, Offshore and Arctic Engineering*, 2014, p. V09AT09A021; 12 pages.
[43] Wang K., Moan T., and Hansen M. O. L., "Stochastic dynamic response analysis of a floating vertical-axis wind turbine with a semi-submersible floater," *Wind Energy,* 2016.
[44] Cheng Z., Wang K., Gao Z., and Moan T., "Dynamic Modelling and Analysis of Three Floating Wind Turbine Concepts with Vertical Axis Rotor," *International Society of Offshore and Polar Engineers (ISOPE),* vol. 25, p. 9, June 21-26, 2015 2015.
[45] UWE. (May 06,2016). *Turbine Options: Vertical Axis vs. Horizontal Axis*. Available: https://sites.google.com/a/temple.edu/urbanwind/services/turbine-options-and-specifications
[46] Paquette J. and Barone M., "Innovative offshore vertical-axis wind turbine rotor project " EWEA 2012 Annual Event (2012).

[47] Wang K., Luan C., Moan T., and Hansen M. O. L., "Comparative Study of a FVAWT and a FHAWT with a Semi-submersible Floater," in *Proceedings of the Twenty-fourth (2014) International Offshore and Polar Engineering Conference*, Busan, Korea,, 2014, pp. 302 -

[48] Anagnostopoulou C., Kagemoto H., Sao K., and Mizuno A., "Concept design and dynamic analyses of a floating vertical-axis wind turbine: case study of power supply to offshore Greek islands," *Ocean Engineering and Marine Energy,* 25 July 2015 2015.

[49] OffshoreWIND. Floating Offshore Wind Project INFLOW Kicks-Off in France [Online].

[50] Paulsen U. S., Pedersen T. F., Madsen H. A., Enevoldsen K., Nielsen P. H., Hattel J.*, et al.*, "Deepwind - An innovative wind turbine concept for offshore," in *European Wind Energy Association (EWEA) Annual Event*, Brussels, 2011.

[51] Vita L., Paulsen U. S., and Pedersen T. F., "A novel floating offshore wind turbine concept: new developments," in *European Wind Energy Conference and Exhibition*, Poland, 2010.

[52] Vita L., Paulsen U. S., Pedersen T. F., Madsen H. A., and Rasmussen F., "A novel floating offshore wind turbine concept," in *European Wind Energy Conference and Exhibition*, Marseille, France, 2009.

[53] Cahay M., Luquiau E., Smadja C., and SILVERT F. C. C., "Use of a Vertical Wind Turbine in an Offshore Floating Wind Farm," in *Offshore Technology Conference* Houston, Texas, USA, 2011.

[54] *10MW Aerogenerator X © Wind Power Limited & Grimshaw at http://vimeo.com/13654447*.

[55] Paulsen U. S., Vita L., Madsen H. A., Hattel J., Ritchie E., Leban K. M.*, et al.*, "1st DeepWind 5 MW Baseline design," *Energy Procedia,* vol. 24, pp. 27-35, 2012.

[56] Robertson A., Jonkman J., Masciola M., Song H., Goupee A., Coulling A.*, et al.*, "Definition of the Semi-submersible Floating System for Phase II of OC4," 2012.

[57] Vita L., Pedersen T. F., and Madsen H. A., "Offshore Vertical Axis Wind Turbine with Floating and Rotating Foundation," *Lyngby, Denmark: Technical University of Denmark (DTU),* August 2011 2011.

[58] Strickland J. H., "The Darrieus turbine: a performance prediction model using multiple streamtubes," Sandia Laboratories, operated for the United States Department of Energy by Sandia Corporation., Albuquerque, New Mexico (US) SAND75-0431, 1975.

[59] Madsen H. A., *On the ideal and real energy conversion in a straight bladed vertical axis wind turbine*. Aalborg, Denmark,: Aalborg University Centre, 1983.

[60] al B. S. e., "Integrated dynamic analysis of floating offshore wind turbines," in *Euorpean Wind Energy Conference (EWEC)*, Milan, Italy, 2007.

[61] Larsen T. J. and Hansen A. M., "How 2 Hawc2, the user's manual," *Wind Energy,* 2014.

[62] Larsen T. J. and Hanson T. D., "A method to avoid negative damped low frequent tower vibrations for a floating, pitch controlled wind turbine," in *The Conference The science of making torque from the wind*, Copenhagen, Denmark, 2007.

[63] Ormberg H. and Bachynski E. E., "Global analysis of floating wind turbines: Code development, model sensitivity and benchmark study," in *Proceedings of the 22nd International Ocean and Polar Engineering Conference*, Rhodes, Greece, 2012.

[64] Moriarty P. J. and Hansen A. C., "AeroDyn theory manual," (NREL) N. R. E. L., Ed., ed. Denver West Parkway. Golden, US, 2005.

[65] Borg M., Wang K., Collu M., and Moan T., "A comparison of two coupled model of dynamics for offshore floating vertical axis wind turbines " in *Proceeding of the ASME 2014 33rd International Conference on Ocean, Offshore and Arctic Engineering*, San Francisco, California, USA, 2014.

[66] Collu M., Borg M., Shires A., and Brennan F. P., "FloVAWT: Progress on the development o a coupled model of dynamics for floating offhsore wind turbines," in *Proceeding of the ASME 2014 33rd International Conference on Ocean, Offshore and Arctic Engineering*, San Francisco, California, USA, 2014.

[67] Paraschivoiu I. and Delclaux F., "Double multiple streamtube model with recent improvements (for predicting aerodynamic loads and performance of Darrieus vertical axis wind turbines)," *Energy,* vol. 7, pp. 250-255, 1983.

[68] Mertens S., Kuik G. v., and Bussel G. v., "Performance of an H-Darrieus in the skewed flow on a roof.," *Journal of Solar Energy Engineering,* vol. 125, pp. 433-440, 2003.

[69] Wang K., Moan T., and Hansen M. O. L., "A method for modeling of floating vertical axis wind turbine," in *Proceedings of the 32nd International Conference on Ocean, Offshore and Arctic Engineering*, Nantes, France, 2013.

[70] Wang K., Hansen M. O. L., and Moan T., "Model improvements for evaluating the effect of towertilting on the aerodynamics of a vertical axis wind turbine," *Wind Energy,* vol. 18, pp. 91–110, 2015.

[71] Wang K., "Modelling and dynamic analysis of a semi-submersible floating vertical axis wind turbine," PhD, Faculty of Engineering Science and Technology: Department of Marine Technology, Norwegian University of Science and Technology, Norway, 2015.

[72] Hayman G. J. and Buhl M. J., "MLife User's Guide for Version 1.00.00," NREL, Ed., ed. Oak Ridge, TN 37831-0062, 2012.

[73] Verelst D. R., Aagaard M. H., Kragh K. A., and Belloni F., "Detailed Load Analysis of the baseline 5MW DeepWind Concept," DTU Wind Energy., Denmark2014.

[74] Wang K., Hansen M. O. L., and Moan T., "Dynamic Analysis of a Floating Vertical Axis Wind Turbine Under Emergency Shutdown Using Hydrodynamic Brake," in *EERA DeepWind' 2014, 11th Deep Sea Offshore Wind R&D Conference*, 2014, pp. 56-69.

[75] Paulsen U. S., Madsen H. A., Hattel J. H., Baran I., and Nielsen P. H., "Design optimization of a 5MW floating offshore vertical axis wind turbine.," in *DeepWind'2013-10th Deep Sea Offshore Wind R&D Conference* Trondheim, Norway, 2013, pp. 22–32.

[76] WMO, "Guide to Meteorological Instruments and Methods of Observation," WMO-World Meteorological Organisation, Geneva, Switzerland1983.

[77] DNV-OS-C205, "Environmental conditions and environmental loads," in *Offshore standard*, ed. Norway: Det Norske Veritas- Germanischer Lloyd, 2010.

[78] IEC, "Wind turbines- Part 3: Design requirement for offshore wind turbines.," vol. IEC61400-3 ed: International Electrotechnical Commission, 2009.

[79] IEC-61400-3, "Wind turbines – Part 3," in *Design requirements for offshore wind turbines*, ed, 2009, p. 61.

[80] IEC-61400-1, "Wind turbines – Part 1," in *Design requirements for offshore wind turbines*, ed, 2005, p. 22.

[81] Jonkman B. J. and Kilcher L., "TurbSim User's Guide: Version 1.06.00," (NREL) N. R. E. L., Ed., ed, 2012.

[82] Manwell J. F., McGowan J. G., and Rogers A. L., *Wind Energy Explained: Theory Design and Application*. Hoboken: John Wiley & Sons, 2002.

[83] Beri H. and Yao Y., "Double Multiple Stream Tube Model and Numerical Analysis of Vertical Axis Wind Turbine " *Energy and Power Engineering,* vol. 3, pp. 262-270, 2011.

[84] Klimas P. C., "Darrieus rotor aerodynamics. Transactions of the ASME," *Journal of Solar Energy Engineering,* pp. 102-105, 1982.

[85] Templin R. J., "Aerodynamic performance theory for the NRC vertical-axis wind turbine," National Aeronautical Establishment, Ottawa, Ontario (Canada)1974.

[86] Strickland J. H., "The Darrieus Turbine: A Performance Prediction Model Using Multiple Streamtubes," Sandia National Laboratories, Albuquerque, N.M.1975.

[87] Paraschivoiu I., "Double-multiple streamtube model for Darrieus Wind Turbines," presented at the Second DOE/NASA Wind Turbines Dynamics Workshop, NASA CP-2185, Cleveland, Ohio, 1981.

[88] Madsen H., "The Actuator Cylinder – a flow model for vertical axis wind turbines," PhD PhD Aalborg University Centre, 1982.

[89] Scheurich F., Fletcher T. M., and Brown R. E., "Simulating the aerodynamic performance and wake dynamics of a vertical-axis wind turbine.," *Wind Energy,* vol. 14, pp. 159-177, 2011.

[90] Zanon A., Giannattasio P., and Simão-Ferreira C. J., " A vortex panel model for the simulation of the wake flow past a vertical axis wind turbine in dynamic stall," *Wind Energy,* vol. 16, pp. 661-680, 2013.

[91] Strickland J. H., Webster B. T., and Nguyen T., "A vortex model of the Darrieus turbine: An analytical and experimental study," *Fluid Engineering,* vol. 101, pp. 500-505, 1979.

[92] Hirsch H. and MA C., " A cascade theory for the aerodynamic performance of Darrieus wind turbines," *wind Engineering,* vol. 11, pp. 164-175, 1987.

[93] Dixon K. and . "The near wake structure of a vertical axis wind turbine," TU Delft, The Netherlands2009.

[94] Dixon K., Ferreira C. S., Hofemann C., and Bussel G. V., "A 3d unsteady panel method for vertical axis wind turbines," in *The proceedings of the European Wind Energy Conference & Exhibiti on EWEC*, Brussels, 2008.

[95] Simão, Ferreira C., and Scheurich F., "Demonstrating that power and instantaneous loads are decoupled in a vertical-axis wind turbine," *Wind Energy,* vol. 17, pp. 385-396, 2014.

[96] Vishal P. B. K., "Performance prediction of a straight bladed darrieus wind turbine by single streamtube model," *International Journal of Advanced Engineering Technology,* vol. IV, pp. 86–89, April-June 2013.

[97] Paraschivoiu I., "Double-multiple stream tube model for studying vertical-axis wind turbines," *Journal of Propulsion and Power,* vol. 4, 1988.

[98] Simão C. F., "The near wake of the VAWT: 2D and 3D views of the VAWT aerodynamics. PhD thesis," PhD, Faculty of Aerospace Engineering, Delft University of Technology, The Netherlands, 2009.

[99] Roscher B., "Structural Optimization Of A Vertical Axis Wind Turbine With Aeroelastic Analysis," M.Sc, Wind Energy and Aerospace Engineering, Technical University of Denmark and Delft University of Technology., Denmark, 2014.

[100] Madsen H. A., "Application of actuator surface theory on wind turbines," in *Proceedings of IEA meeting on Joint Actions on Aerodynamics of Wind Turbines*, 2. Symposium held in Lyngby, 1988.

[101] Madsen H. A., Paulsen U. S., and Vita L., "Analysis of VAWT aerodynamics and design using the Actuator Cylinder flow model," 2012.

[102] Helge M., Torben L., Luca V., and Uwe P., "Implementation of the Actuator Cylinder flow model in the HAWC2 code for aeroelastic simulations on Vertical Axis Wind Turbines," presented at the 51st AIAA Aerospace Sciences Meeting including the New Horizons Forum and Aerospace Exposition, 2013.

[103] Larsen H. C., "Summary of a vortex theory for the cyclogiro,," in *Proceedings of the second US national conferences on wind engineering research*, US, 1975, pp. V8-1-3.

[104] Fanucci J. B. and Walter R. E., "Innovative wind machines: the theoretical performace of a vertical-axis wind turbine," in *Proceedings of the vertical-axis wind turbine technology workshop*, USA, 1976.

[105] Holme O. A., "Contribution to the aerodynamic theory of the vertical axis wind turbine," presented at the International symposium on wind energy system, Cambridge, England, 1976.

[106] Wilson R. E., "Wind-turbine aerodynamics," *Journal of Wind Engineering and Industrial Aerodynamics,* vol. 5, pp. 357-372, May 1980 1980.

[107] Strickland J. H., Webster B., and Nguyen T., "Vortex model of the Darrieus turbine: An analytical and experimental study," Sandia National Laboratory, USA1981.

[108] Cardona J. L., "Flow curvature and dynamic stall stimulated with an aerodynamic free-vortex model for vawt," *wind Engineering,* vol. 8, pp. 135-143, 1984.

[109] Vandenberghe D. and Dick E., "A free vortex simulation method for the straight bladed vertical axis wind turbine," *Journal of Wind Engineering and Industrial Aerodynamics,* vol. 26, pp. 307-324, 1987.

[110] Ponta F. L. and Jacovkis P. M., "A vortex model for Darrieus turbine using finite element techniques," *Renewable Energy,* vol. 24, pp. 1-18, 2001.

[111] Brown R. E., "Rotor wake modeling for flight dynamic simulation of helicopters," *AIAA journal,* vol. 38, pp. 57-63, 2000.

[112] Scheurich F. and Brown R. E., "Modelling the aerodynamics of vertical-axis wind turbines in unsteady wind conditions," *Wind Energy,* vol. 16, pp. 91-107, 2013.

[113] Penna P. J., "Wind tunnel tests of the Quiet Revolution Ltd. QR5 vertical axis wind turbine," Institute for Aerospace Research, National Research Council, Canada2008.
[114] Schuerich F. and Brown R. E., "Effect of dynamic stall on the aerodynamics of vertical-axis wind turbines," *AIAA journal,* vol. 49, pp. 2511-2521.
[115] Scholz N., "Aerodynamics of cascades. Translated and revised by A. Kline," AGARD-AG-2201965.
[116] Islam M., Ting D.-K., and Fartaj A., "Aerodynamic models for Darrieus-type straight-bladed vertical axis wind turbines," *Renewable and Sustainable Energy Reviews,* vol. 12, pp. 1087-1109, 2008.
[117] Wang L., Zhang L., and Zeng N., " A potential flow 2-D vortex panel model: Applications to vertical axis straight blade tidal turbine," *Energy conversion and managemen,* vol. 48, pp. 454-461, 2007.
[118] Katz J. and Plotkin A., *Low Speed Aerodynamics*, 2nd ed. Cambridge, UK: Cambridge University Press, 2001.
[119] Erickson L. L., "Panel Methods - An Introduction," NASA., California, NASA1990.
[120] Hansen M. O. L. and Sørensen D. N., "CFD model for vertical axis wind turbine.," in *Wind Energy for the New Millennium - Proceedings of the European Wind Energy Conference*, Copenhagen, 2001, pp. 485-488.
[121] Horiuchi K., I U., and K S., "Straight wind vertical axis wind turbines: a flow analysis," *wind Engineering,* vol. 29, pp. 243-252, 2005.
[122] Ferreira C. J. S., Zuijlen A. v., Bijl H., and Bussel G. v., "Simulating dynamic stall in a two-dimensional vertical-axis wind turbine: verification and validation with particle image velocimetry data," *Wind Energy,* vol. 13, pp. 1-17, 2009.
[123] Leishman J. G., *Principles of helicopter aerodynamics. 2nd ed.* Cambridge: Cambridge University Press, 2006.
[124] Gormont R. E., "A mathematical model of unsteady aerodynamics and radial flow for application to helicopter rotors," Boeing Co, Vertol Div., Philadelphia, PA1973.
[125] Paraschivoiu I., *Wind turbine design: with emphasis on Darrieus concept*. Montreal: Polytechnic International Press, 2002.
[126] Berg D. E., "An Improved Double-Multiple Streamtube Model for the Darrieus Type Vertical-Axis Wind Turbine," in *Preceedings of the Sixth Biennial Wind Energy Conference and Workshop*, Minneapolis,MN, 1983, pp. 231-238.
[127] Leishman J. and Beddoes T., "A semi-empirical model for dynamic stall," *Journal of the American Helicopter Society,* vol. 34, pp. 3-17, 1989.
[128] Gupta S. and Leishman J., "Dynamic stall modelling of the S809 aerofoil and comparison with experiments.," *Wind Energy,* vol. 9, pp. 521-547, 2006.
[129] Gudmestad O. T., *Marine Technology and Operations: Theory and Practice*. Ashurs: Southampton UK: WIT Press, 2015.
[130] DNV-OS-E301, "Position mooring," in *Offshore standard*, ed. Norway: Det Norske Veritas-Germanischer Lloyd, 2010.
[131] WMO, "GUIDE TO WAVE ANALYSIS AND FORECASTING," vol. WMO-No. 702, ed. Secretariat of the World Meteorological Organization – Geneva – Switzerland: World Meteorological Organization, 1998.
[132] *Modelling a precision loadcell using neural networks for vision-based force measurement in cell micromanipulation*. Available: http://researchbank.rmit.edu.au/view/rmit:31057 Item Resolution URL
[133] Chakrabarti S. K., *Hydrodynamics of Offshore Structures*. UK: WIT Press, 1987.
[134] Moskowitz L., "Estimates of the power spectrums for fully developed seas for wind speeds of 20 to 40 knots," *Journal of Geophysical Research,* vol. 69, pp. 5161–5179, 1964.
[135] Hasselman K., Barnett T. P., Bouws E., Carlson H., Cartwright D. E., Enke K*., et al.*, "Measurements of Wind-Wave Growth and Swell Decay During the Joint North sea Wave Project (JONSWAP)," DEUTSCHEN HYDROGRAPHISOHES INSTITUT . HAMBURG, Deutschen Hydro-graphischen Institut, No. 12, Hamburg, Germany.1973.
[136] Torsethaugen K., "Model for Double Peaked Wave Spectrum," SINTEF Civil and Envir. Engineering,Trondheim, Norway., Trondheim, Norway.1996.

[137] Migliore P. G. and Cheney M. C., "Feasibility study of pultruded blades for wind turbine rotors," in *Proceedings of the ASME/AIAA Wind Energy Symposium*, Reno, Nevada (US), 2000.

[138] Migliore P. G. and Cheney M. C., "Feasibility Study of Pultruded Blades for Wind Turbine Rotors," presented at the ASME/AIAA 2000 Wind Energy Symposium, Reno, Nevada, 2000.

[139] Ralph M. E., "Design and Control of the variable speed generator on the Sandia 34-meter vertical axis wind turbine " in *Proceedings of the Windpower Conference*, San Francisco, California (US), 1989, pp. 55-59.

[140] Sutherland H. J., Berg D. E., and Ashwill T. D., "A retrospective of VAWT technology," Sandia National Laboratories, Albuquerque, NM, USA 2012.

[141] Paulsen U. S., Borg M., Madsen H. A., Pedersen T. F., Hattel J., Ritchie E.*, et al.*, "Outcomes of the DeepWind conceptual design," *Energy Procedia. 12th Deep Sea Offshore Wind R&D Conference, EERA DeepWind,* vol. 80, pp. 329 – 341, 2015.

[142] Uwe S. P., Helge A. M., Abildgaard K. K., Nielsen P.-H., Baran I., Ritchie E.*, et al.*, "The 5 MW DeepWind floating offshore vertical wind turbine concept design - status and perspective," in *Proceedings - EWEA 2014*, European Wind Energy Association (EWEA), 2014.

[143] Paulsen U. S., Madsen H. A., Hattel J. H., Baran I., Nielsen P. H., Ritchie E.*, et al.*, "DeepWind-from idea to 5 MW concept " *Energy Procedia,* 2014.

[144] Marit K. I. and Chenyu L., "Use of Buoyancy Compensating Force in Coupled Simo-Riflex Models," Centre for Ships and Ocean Structures, NOWITECHJune 2013 2013.

[145] MARINTEK, "SIMO-User's Manual Appendix A ", MARINTEK, Ed., ed. Norway, 2013.

[146] WAMIT-Inc., "WAMIT USER MANUAL," Technology M. I. o., Ed., ed. Chestnut Hill, MA 02467-2504 USA, 1998.

[147] Naess A. and Moan T., *Stochastic dynamics of marine structures.*: Cambridge University Press, 2012.

[148] Marit K. I., "Modelling and response analysis for fatigue design of a semi-submersible wind turbine," PhD, Department of Marine Technology, Norwegian University of Science and Technology, Faculty of Engineering Science and Technology, 2014.

[149] MARINTEK, "RIFLEX Theory Manual," MARINTEK, Ed., ed, 2013.

[150] Sicklinger S., Lerch C., Wüchner R., and Bletzinger K.-U., "Fully coupled co-simulation of a wind turbine emergency brake maneuver," *Wind Engineering & Industrial Aerodynamics,* vol. 144, pp. 134–145, 2015.

[151] Cheng Z., Wang K., Gao Z., and Moan T., "Dynamic Response Analysis of Three Floating Wind Turbine Concepts with a Two-Bladed Darrieus Rotor," *Ocean and Wind Energy* vol. 2, pp. 213–222;, November 2015 2015.

[152] Johannessen K., Meling T. S., and Haver S., "Joint distribution for wind and waves in the northern north sea," *International Journal of Offshore and Polar Engineering,* vol. 12, 2002.

[153] Larsen P. K., *Design of steel structures (in Norwegian)*: Tapir, 1997.

[154] DNV-RP-C203, "Fatigue Design of Offshore Steel Structures," ed. Norway: Det Norske Veritas, 2010.

[155] Fredheim Ø., "Fatigue analysis of column-brace connection in a semi-submersible wind turbine.," Masters, Norwegian University of Science and Technology, Norway, 2012.

[156] Matsuishi M. and Endo T., "Fatigue of metals subjected to varying stress," *Society of Mechanical Engineers, Fukuoka, Japan,* pp. 37–40, 1968.

[157] Andreas B., Par J., Georg L., and Igor R., "Wafo– a Matlab Toolbox for Analysis of Random Waves and Loads," WAFO-group F. O. E., CENTRE FOR MATHEMATICAL SCIENCES, MATHEMATICAL STATISTICS, Ed., ed. LUND University, Sweden, 2011.

Appendix A

A.1- TurbSim Input file for the 5 MW Baseline FVAWT

TurbSim Input File. Valid for TurbSim v1.50, 25-Sep-2009; for Certification Test #1 (Kaimal Spectrum, formatted FF files).

---------Runtime Options----------

10000 RandSeed1 - First random seed (-2147483648 to 2147483647)

70000 RandSeed2 - Second random seed (-2147483648 to 2147483647) for intrinsic pRNG, or an alternative pRNG: "RanLux" or "RNSNLW"

False WrBHHTP - Output hub-height turbulence parameters in GenPro-binary form? (Generates RootName.bin)

False WrFHHTP - Output hub-height turbulence parameters in formatted form? (Generates RootName.dat)

False WrADHH - Output hub-height time-series data in AeroDyn form? (Generates RootName.hh)

False WrADFF - Output full-field time-series data in TurbSim/AeroDyn form? (Generates RootName.bts)

True WrBLFF - Output full-field time-series data in BLADED/AeroDyn form? (Generates RootName.wnd)

False WrADTWR - Output tower time-series data? (Generates RootName.twr)

False WrFMTFF - Output full-field time-series data in formatted (readable) form? (Generates RootName.u, RootName.v, RootName.w)

False WrACT - Output coherent turbulence time steps in AeroDyn form? (Generates RootName.cts)

True Clockwise - Clockwise rotation looking downwind? (used only for full-field binary files - not necessary for AeroDyn)

0 ScaleIEC - Scale IEC turbulence models to exact target standard deviation? [0=no additional scaling; 1=use hub scale uniformly; 2=use individual scales]

--------Turbine/Model Specifications----------

31 NumGrid_Z - Vertical grid-point matrix dimension

31 NumGrid_Y - Horizontal grid-point matrix dimension

0.05 TimeStep - Time step [seconds]

4600.0 AnalysisTime - Length of analysis time series [seconds] (program will add time if necessary: AnalysisTime = MAX(AnalysisTime, UsableTime+GridWidth/MeanHHWS))

4600.0 UsableTime - Usable length of output time series [seconds] (program will add GridWidth/MeanHHWS seconds)

79.78 HubHt - Hub height [m] (should be > 0.5*GridHeight)

158.00 GridHeight - Grid height [m]

180.00 GridWidth - Grid width [m] (should be >= 2*(RotorRadius+ShaftLength))

0 VFlowAng - Vertical mean flow (uptilt) angle [degrees]

0 HFlowAng - Horizontal mean flow (skew) angle [degrees]

--------Meteorological Boundary Conditions----------

"IECKAI" TurbModel - Turbulence model ("IECKAI"=Kaimal, "IECVKM"=von Karman, "GP_LLJ", "NWTCUP", "SMOOTH", "WF_UPW", "WF_07D", "WF_14D", or "NONE")

"1-Ed3" IECstandard - Number of IEC 61400-x standard (x=1,2, or 3 with optional 61400-1 edition number (i.e. "1-Ed2"))

"C" IECturbc - IEC turbulence characteristic ("A", "B", "C" or the turbulence intensity in percent) ("KHTEST" option with NWTCUP, not used for other models)

"NTM" IEC_WindType - IEC turbulence type ("NTM"=normal, "xETM"=extreme turbulence, "xEWM1"=extreme 1-year wind, "xEWM50"=extreme 50-year wind, where x=wind turbine class 1, 2, or 3)

default ETMc - IEC ETM "c" parameter [m/s] (or "default")

"PL" WindProfileType - Wind profile type ("JET"=Low-level jet,"LOG"=Logarithmic,"PL"=Power law, or "default")

79.78 RefHt - Height of the reference wind speed [m]

14.0 URef - Mean (total) wind speed at the reference height [m/s]

350 ZJetMax - Jet height [m] (used only for JET wind profile, valid 70-490 m)

default PLExp - Power law exponent (or "default")

default Z0 - Surface roughness length [m] (or "default")

--------Non-IEC Meteorological Boundary Conditions----------

default Latitude - Site latitude [degrees] (or "default")

0.05 RICH_NO - Gradient Richardson number

default UStar - Friction or shear velocity [m/s] (or "default")

default ZI - Mixing layer depth [m] (or "default")

default PC_UW - Mean hub u'w' Reynolds stress (or "default" or "none")

default PC_UV - Mean hub u'v' Reynolds stress (or "default" or "none")

default PC_VW - Mean hub v'w' Reynolds stress (or "default" or "none")

default IncDec1 - u-component coherence parameters (e.g. "10.0 0.3e-3" in quotes) (or "default")

default IncDec2 - v-component coherence parameters (e.g. "10.0 0.3e-3" in quotes) (or "default")

default IncDec3 - w-component coherence parameters (e.g. "10.0 0.3e-3" in quotes) (or "default")

default CohExp - Coherence exponent (or "default")

--------Coherent Turbulence Scaling Parameters----------

".\EventData" CTEventPath - Name of the path where event data files are located

random CTEventFile - Type of event files ("random", "les" or "dns")

true Randomize - Randomize disturbance scale and location? (true/false)

1.0 DistScl - Disturbance scale (ratio of dataset height to rotor disk).

0.5 CTLy - Fractional location of tower centerline from right (looking downwind) to left side of the dataset.

0.5 CTLz - Fractional location of hub height from the bottom of the dataset.

30.0 CTStartTime - Minimum start time for coherent structures in RootName.cts [seconds]

==========

NOTE: Do not add or remove any lines in this file!

==========

A.2 - TurbSim Input file for the 5 MW Optimised FVAWT

TurbSim Input File. Valid for TurbSim v1.50, 25-Sep-2009; for Certification Test #1 (Kaimal Spectrum, formatted FF files).

---------Runtime Options----------

10000 RandSeed1 - First random seed (-2147483648 to 2147483647)

70000 RandSeed2 - Second random seed (-2147483648 to 2147483647) for intrinsic pRNG, or an alternative pRNG: "RanLux" or "RNSNLW"

False WrBHHTP - Output hub-height turbulence parameters in GenPro-binary form? (Generates RootName.bin)

False WrFHHTP - Output hub-height turbulence parameters in formatted form? (Generates RootName.dat)

False WrADHH - Output hub-height time-series data in AeroDyn form? (Generates RootName.hh)

False WrADFF - Output full-field time-series data in TurbSim/AeroDyn form? (Generates RootName.bts)

True WrBLFF - Output full-field time-series data in BLADED/AeroDyn form? (Generates RootName.wnd)

False WrADTWR - Output tower time-series data? (Generates RootName.twr)

False WrFMTFF - Output full-field time-series data in formatted (readable) form? (Generates RootName.u, RootName.v, RootName.w)

False WrACT - Output coherent turbulence time steps in AeroDyn form? (Generates RootName.cts)

True Clockwise - Clockwise rotation looking downwind? (used only for full-field binary files - not necessary for AeroDyn)

0 ScaleIEC - Scale IEC turbulence models to exact target standard deviation? [0=no additional scaling; 1=use hub scale uniformly; 2=use individual scales]

--------Turbine/Model Specifications----------

31 NumGrid_Z - Vertical grid-point matrix dimension

31 NumGrid_Y - Horizontal grid-point matrix dimension

0.05 TimeStep - Time step [seconds]

4600.0 AnalysisTime - Length of analysis time series [seconds] (program will add time if necessary: AnalysisTime = MAX(AnalysisTime, UsableTime+GridWidth/MeanHHWS))

4600.0 UsableTime - Usable length of output time series [seconds] (program will add GridWidth/MeanHHWS seconds)

86.50 HubHt - Hub height [m] (should be > 0.5*GridHeight)

170.00 GridHeight - Grid height [m]

180.00 GridWidth - Grid width [m] (should be >= 2*(RotorRadius+ShaftLength))

0 VFlowAng - Vertical mean flow (uptilt) angle [degrees]

0 HFlowAng - Horizontal mean flow (skew) angle [degrees]

--------Meteorological Boundary Conditions----------

"IECKAI" TurbModel - Turbulence model ("IECKAI"=Kaimal, "IECVKM"=von Karman, "GP_LLJ", "NWTCUP", "SMOOTH", "WF_UPW", "WF_07D", "WF_14D", or "NONE")

"1-Ed3" IECstandard - Number of IEC 61400-x standard (x=1,2, or 3 with optional 61400-1 edition number (i.e. "1-Ed2"))

"C" IECturbc - IEC turbulence characteristic ("A", "B", "C" or the turbulence intensity in percent) ("KHTEST" option with NWTCUP, not used for other models)

"NTM" IEC_WindType - IEC turbulence type ("NTM"=normal, "xETM"=extreme turbulence, "xEWM1"=extreme 1-year wind, "xEWM50"=extreme 50-year wind, where x=wind turbine class 1, 2, or 3)

default ETMc - IEC ETM "c" parameter [m/s] (or "default")

"PL" WindProfileType - Wind profile type ("JET"=Low-level jet,"LOG"=Logarithmic,"PL"=Power law, or "default")

86.50 RefHt - Height of the reference wind speed [m]

14.00 URef - Mean (total) wind speed at the reference height [m/s]

350 ZJetMax - Jet height [m] (used only for JET wind profile, valid 70-490 m)

default PLExp - Power law exponent (or "default")

default Z0 - Surface roughness length [m] (or "default")

--------Non-IEC Meteorological Boundary Conditions----------

default Latitude - Site latitude [degrees] (or "default")

0.05 RICH_NO - Gradient Richardson number

default UStar - Friction or shear velocity [m/s] (or "default")

default ZI - Mixing layer depth [m] (or "default")

default PC_UW - Mean hub u'w' Reynolds stress (or "default" or "none")

default PC_UV - Mean hub u'v' Reynolds stress (or "default" or "none")

default PC_VW - Mean hub v'w' Reynolds stress (or "default" or "none")

default IncDec1 - u-component coherence parameters (e.g. "10.0 0.3e-3" in quotes) (or "default")

default IncDec2 - v-component coherence parameters (e.g. "10.0 0.3e-3" in quotes) (or "default")

default IncDec3 - w-component coherence parameters (e.g. "10.0 0.3e-3" in quotes) (or "default")

default CohExp - Coherence exponent (or "default")

--------Coherent Turbulence Scaling Parameters----------

".\EventData" CTEventPath - Name of the path where event data files are located

random CTEventFile - Type of event files ("random", "les" or "dns")

true Randomize - Randomize disturbance scale and location? (true/false)

1.0 DistScl - Disturbance scale (ratio of dataset height to rotor disk).

0.5 CTLy - Fractional location of tower centerline from right (looking downwind) to left side of the dataset.

0.5 CTLz - Fractional location of hub height from the bottom of the dataset.

30.0 CTStartTime - Minimum start time for coherent structures in RootName.cts [seconds]

==========

NOTE: Do not add or remove any lines in this file!

==========